POLITECNICO DI TORINO
Repository ISTITUZIONALE

Challenges and opportunities for SERS in the infrared: materials and methods

Original
Challenges and opportunities for SERS in the infrared: materials and methods / Deriu, C., Thakur, S., Tammaro, O., Fabris, L.. - In: NANOSCALE ADVANCES. - ISSN 2516-0230. - ELETTRONICO. - 5:8(2023), pp. 2132-2166. [10.1039/D2NA00930G]

Availability:
This version is available at: 11583/2977757 since: 2025-02-04T10:52:01Z

Publisher:
Royal Society of Chemistry

Published
DOI:10.1039/D2NA00930G

Terms of use:

This article is made available under terms and conditions as specified in the corresponding bibliographic description in the repository

Publisher copyright

(Article begins on next page)

10 October 2026

Nanoscale Advances

ROYAL SOCIETY OF CHEMISTRY

REVIEW

View Article Online
View Journal

Check for updates

Cite this: DOI: 10.1039/d2na00930g

Challenges and opportunities for SERS in the infrared: materials and methods

Chiara Deriu, *[a] Shaila Thakur, [a] Olimpia Tammaro [a] and Laura Fabris [ab]

In the wake of a global, heightened interest towards biomarker and disease detection prompted by the SARS-CoV-2 pandemic, surface enhanced Raman spectroscopy (SERS) positions itself again at the forefront of biosensing innovation. But is it ready to move from the laboratory to the clinic? This review presents the challenges associated with the application of SERS to the biomedical field, and thus, to the use of excitation sources in the near infrared, where *biological windows* allow for cell and through-tissue measurements. Two main tackling strategies will be discussed: (1) acting on the design of the enhancing substrate, which includes manipulation of nanoparticle shape, material, and supramolecular architecture, and (2) acting on the spectral collection set-up. A final perspective highlights the upcoming scientific and technological bets that need to be won in order for SERS to stably transition from benchtop to bedside.

Received 19th December 2022
Accepted 15th March 2023

DOI: 10.1039/d2na00930g

rsc.li/nanoscale-advances

Open Access Article. Published on 22 March 2023. Downloaded on 4/4/2023 3:23:28 PM.
This article is licensed under a Creative Commons Attribution-NonCommercial 3.0 Unported Licence.

1 Introduction

When setting up a new laboratory infrastructure for surface-enhanced Raman spectroscopy (SERS), scientists have nowadays the privilege to choose among the widest-to-date set of commercially available instrumentation: from tunable lasers to microscope-integrated spectrometers, from easily couplable instruments that allow for *operando* measurements, to portable and miniaturized technology enabling measurements in the field or *in vivo*. This was certainly not the case twenty years ago. Raman instruments were often built in-house, the knowledge on the manipulation of materials at the nanoscale, and with it, the whole world of plasmonics, was still very limited. Surely, applications of SERS to everyday analytical issues were pioneering, when not still out of reach.

Fueled by the nanotechnology revolution that characterized the 2000s, SERS has managed to rapidly advance from niche, obscure analytical technique, to a thriving field at the forefront of analytical innovation. The technological advancements in bottom-up fabrication with increasing control over size and shape,[1–5] the development of high precision top-down and soft

[a]*Department of Applied Science and Technology, Politecnico di Torino, 10129 Turin, Italy. E-mail: chiara.deriu@polito.it*
[b]*Department of Materials Science and Engineering, Rutgers University, Piscataway, NJ 08854, USA*

Chiara Deriu obtained her PhD in Chemistry from Florida International University (FIU), Miami, USA, in 2020, where she worked on tailoring the stabilization of nanomaterials for the detection of drugs by SERS. Following, she received a postdoctoral appointment at FIU to work on the computational modeling of adsorbates on bimetallic clusters. She then joined Politecnico di Torino (Italy) in September 2021, where she is an ERC-funded postdoctoral researcher. Her scientific interests lie at the intersection of physical chemistry and the analytical sciences, with particular attention to nanoscale surface chemistry and its effects on both nanofabrication and SERS analytical performance.

Shaila Thakur obtained her PhD in Chemical Engineering from Indian Institute of Technology (IIT) Kharagpur, India in 2017. She worked as a postdoctoral scholar at National Center for Biological Sciences (NCBS) Bangalore (India) from 2020–2021. She joined Politecnico di Torino (Italy) as a postdoctoral fellow in 2022. She currently works on an ERC-funded project based on the utilization of plasmonic nanostructures for probing prostate cancer biomarkers. Her research interests include nanomaterial synthesis, biosensing, and interaction of nanomaterials with cells, DNA/RNA and proteins.

© 2023 The Author(s). Published by the Royal Society of Chemistry

Open Access Article. Published on 22 March 2023. Downloaded on 4/4/2023 3:23:28 PM. This article is licensed under a Creative Commons Attribution-NonCommercial 3.0 Unported Licence.

patterning methods,[6–8] the increasing understanding of nanoscale assembly and its integration across larger length scales,[9] all greatly contributed to a transformative era for SERS.[10] In a synergistic tie, nanotechnology and SERS prompted new fundamental research over the last twenty years, opening the doors to plasmonics,[11,12] thus leading to a deeper understanding of the relationships between physical characteristics (material, size, shape, dielectric environment) of SERS-active nanomaterials and their optical properties.[13–16]

The 2000s are also to be remembered as the years that saw a sharp increase in the interest in the biological world: the sequencing of the whole human genome,[17] the cloning of mammals,[18–21] and the development of pharmacogenomics and molecular diagnostics that set the basis for what we now call personalized medicine.[22–27] The SERS community was certainly not an outsider in this global trend; aided by its single molecule sensitivity, it promised access to the study of otherwise inaccessible low concentration biological species.

SERS has an advantage over traditional Raman spectroscopy to allow for trace detection, but it still faces some challenges similar to Raman spectroscopy when dealing with biological analytes like cells and tissues. This is because such challenges—*self-absorption* and *autofluorescence*—are inherent to the molecular structure and complexity of biological systems.[28] With self-absorption we define the physical phenomenon by which sample-scattered photons are absorbed by the sample itself, before reaching the detector, while with autofluorescence we indicate the spontaneous fluorescence emission that a molecule, typically characterized by delocalized π electrons, undergoes upon laser irradiation. These affect the intensity and the signal to noise ratio (S/N) of the detected signal, respectively, and are especially prominent when excitation in the visible range is utilized.[28–30] This is because common tissue constituents, such as hemoglobin, are chromophores that have both the highest absorption coefficients and fluorescence-related electronic transitions in the visible spectrum.[28,29]

While it is true that the plasmonic nanoparticles also act as fluorescence quenchers,[31] a fluorescence background, also called *SERS continuum*,[31] is often present in SERS spectra of biological systems.[32,33] This may be due to the interplay between the analyte's distance from the SERS-active surface, the size and three-dimensional conformation of the analyte on the SERS-active surface, and the concomitant presence of other species (*e.g.*, nanoparticle synthesis by-products, capping agents, residual biological matrix components). The most common strategy that is utilized in traditional Raman spectroscopy to mitigate autofluorescence is to decrease the energy provided to the system, by utilizing lasers emitting at longer wavelengths, for example in the near infrared (NIR).

Incidentally, the use of NIR light can also solve self-absorption phenomena. For instance, the main constituents of tissue, namely whole blood and water, show the lowest absorption coefficients in the regions from 700 to 1000 nm (*first biological window*, NIR I) and from 1000 nm to 1400 nm (*second biological window*, NIR II) (Fig. 1). By reducing absorption, the penetration of the radiation also increases, making imaging of deeper (>500 μm to cm)[28] tissues possible. Furthermore, less energetic excitation sources make Raman spectroscopy amenable to *in vivo* measurements, as they are less likely to impart photochemical damage to samples. Since these principles of Raman spectroscopy also apply to SERS, the problem of autofluorescence and self-absorption phenomena in biological specimen can be solved or minimized by switching to NIR excitation wavelengths. This, however, does not come without its own set of challenges.

2 Overview of challenges

While moving to higher wavelengths can reduce or eliminate autofluorescence and self-absorption phenomena, it also causes

Olimpia Tammaro is a postdoctoral researcher at the Department of Applied Sciences and Technologies at the Politecnico di Torino (Italy). She received an MSc in Materials Engineering from University of Naples "Federico II" (Italy) in 2016. She obtained her PhD in the group of Prof. P. A. Netti at IIT – CABHC (Italy) in 2020. The topic of her doctoral thesis was the development through a microfluidic platform of multi-modal probes. She then carried out postdoctoral research at the Politecnico di Torino (Italy) in the field of chemistry for technologies, with a focus on the synthesis of functional materials.

Laura Fabris received her B.S./M.S. degree in Chemistry in 2001 from the University of Padova, where she was awarded a PhD in 2006. She was then a postdoc at the University of California Santa Barbara. In 2009 she moved to Rutgers University in the Department of Materials Science and Engineering where she remained first as Assistant then as Associate Professor. Upon receiving an ERC Consolidator Grant, she moved to Politecnico di Torino (Italy) in the Department of Applied Science and Technology where she is a Full Professor. Her research combines fundamental notions of nanomaterials chemistry and spectroscopy for the development of new technologies addressing important challenges in medicine, biology, and energy.

© 2023 The Author(s). Published by the Royal Society of Chemistry

Open Access Article. Published on 22 March 2023. Downloaded on 4/4/2023 3:23:28 PM.
This article is licensed under a Creative Commons Attribution-NonCommercial 3.0 Unported Licence.

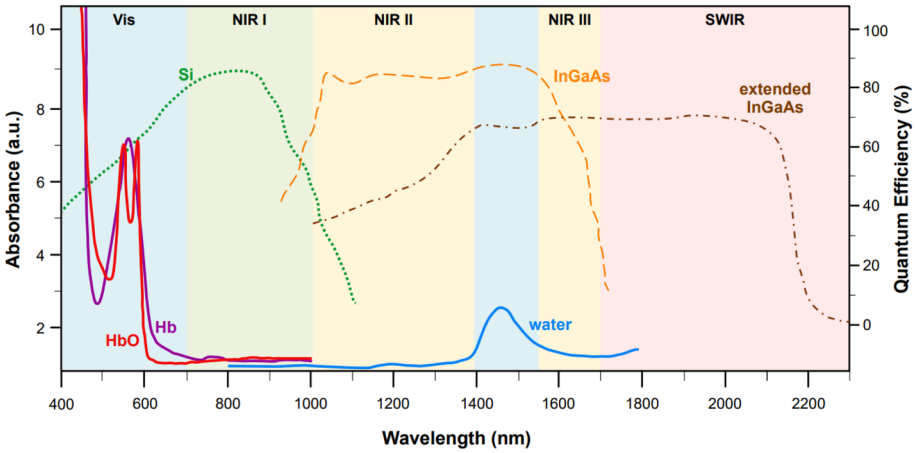

Fig. 1 Representative absorption spectra (*y* axis on the left, optical length of 1 mm) of oxygenated hemoglobin (HbO, red),[38] deoxygenated hemoglobin (Hb, purple),[38] and water (blue).[38] The quantum efficiencies (*y* axis on the right) for the main NIR and SWIR detectors are also reported: silicon-based back-thinned deep depletion EMCCD (green, dotted),[39] lattice-matched InGaAs (orange, dashed),[39] and extended InGaAs (brown, dot-and-dash).[40] The following spectral ranges are highlighted: NIR I (700–1000 nm, *first biological window*), NIR II (1000–1400 nm *second biological window*), NIR III (1550–1700 nm), and SWIR (>1700 nm). Figure inspired by Smith *et al.*, 2009 [39] and Hong *et al.*, 2017.[38]

a concurrent decrease in the intensity of the signal according to the fourth power relationship between the Raman cross section and the frequency of the excitation source ($\sigma \propto \omega^4$), thus causing a loss of sensitivity.[31] Unfortunately, sensitivity problems can also arise from limitations in the current technology for the fabrication of NIR detectors. Silicon-based electron multiplying charge-coupled devices (EMCCD) with back-thinned deep depletion design are characterized by a maximum quantum efficiency at 850 nm (Fig. 1, green dotted profile), which makes them the most popular and effective solution for systems fitted with multiple excitation lines, spanning from the visible (*i.e.*, 514, 532, 633 nm) to 785 nm or 830 nm in the NIR I. However, because of silicon's band gap, the sensitivity of these detectors rapidly approaches zero at wavelengths above 1000 nm. Therefore, different detectors, such as those based on InGaAs, must be utilized in order to access higher wavelengths in the NIR.

Standard InGaAs detectors (lattice-matched $In_{0.53}Ga_{0.47}As$ on InP) have sensitivity that ranges from 1000 nm to 1700 nm (Fig. 1, dashed orange profile),[34] allowing access to the second biological window. The sensitivity range can be further pushed to higher wavelengths *via* indium enrichment (*extended* $In_xGa_{1-x}As$ detectors, $0.53 < x < 1$),[35,36] enabling detection windows centered from 1637 to 1811 nm,[36] or even higher up in the short wavelength (SW) IR (~2200–3000 nm)[34,35] (Fig. 1, brown dot-and-dash profile). Certainly, the tunability of the InGaAs detection window *via* indium enrichment is an interesting property with important technological outcomes; regrettably, indium enrichment also translates to an increase in the lattice mismatch between the InGaAs alloy and the InP substrate, on which the former is typically epitaxially grown or vapor deposited.[34,36] This mismatch causes structural defects that ultimately reduce the optical performances of the material,[36] leading to dark current-induced sensitivity loss,[37] which can be only in part modulated *via* either thermoelectronic- or cryo-cooling. At present, research towards commercially mature, cost effective, low-noise NIR and SWIR detectors is still in progress.

The introduction of excitation wavelengths in the NIR also generates a need to intervene on the design of the enhancing substrate. To understand this necessity, we must recall that SERS is a *plasmonic* analytical technique, and thus, it relies on the excitation of the localized surface plasmon resonance (LSPR). The LSPR can only occur if the following equation is satisfied:[41]

$$\varepsilon_{np}(\lambda) = -\chi\varepsilon_{env} \quad (1)$$

where ε_{np} is the relative permittivity of the nanoparticle, ε_{env} is the relative permittivity of the surrounding environment, and χ is the shape factor for the nanostructure, which is equal to 2 for a sphere, and becomes larger with increasing anisotropic morphology.[14,41] For gold and silver nanospheres, which are the most common SERS substrates, resonance conditions are met when excitation occurs in the visible spectrum.[41] It follows that when silver or gold nanostructures are irradiated with such a light source, the above resonance expression is satisfied, and the LSPR is induced. Eqn (1) also indicates that the relative permittivity, ε, is a function of wavelength, implying that, as the wavelength is changed, the relative permittivity of a given metal, and thus its plasmonic response, also changes. Consequently, SERS substrates that had been proficiently utilized for SERS measurements under visible light excitation (*e.g.*, colloidal silver nanospheres) may not be as ideal or as effective anymore when moving from the visible to the infrared spectrum.

Salt-induced aggregation can shift the LSPR of a SERS-active substrate to higher wavelengths.[31,42] It is indeed very common to perform measurements with aggregated colloidal Au nanospheres when the excitation line is at 785 nm,[43–46] and it has been recently discussed how planar substrates based on large (*i.e.*, obtained by complete colloidal sol disruption) fractal aggregates of silver nanospheres can also be effectively utilized

Open Access Article. Published on 22 March 2023. Downloaded on 4/4/2023 3:23:28 PM.
This article is licensed under a Creative Commons Attribution-NonCommercial 3.0 Unported Licence.

with excitation sources in the NIR I (680–920 nm).[47] However, such planar substrates might not be the optimal analytical strategy for all SERS applications (*e.g.*, *ex vivo* or *in vivo* analysis of tissues), and standard colloidal aggregated nanospheres (Lee, Meisel's,[48] Turkevich's,[49] Frens'[50]) would still keep longer excitation wavelengths in the NIR II and SWIR inaccessible. The necessity to manipulate the LSPR by means other than salt-induced aggregation is therefore apparent.

To this end, it must be recalled that the extinction behavior of a plasmonic nanoparticle as a function of wavelength, $E(\lambda)$, can be described by:[14,41]

$$E(\lambda) = \frac{24\pi^2 N a^3 \varepsilon_{env}^{3/2}}{\lambda \ln(10)} \left[\frac{\varepsilon''_{np}(\lambda)}{\left(\varepsilon'_{np}(\lambda) + \chi\varepsilon_{env}\right)^2 + \varepsilon''_{np}(\lambda)^2} \right] \quad (2)$$

where N is the number of nanoparticles, a is the size term, corresponding to the radius if a spherical nanostructure is assumed, ε'_{np} and ε''_{np} are the real and imaginary part of the relative permittivity of the metal, ε_{np}, describing its absorption and scattering behavior, respectively, and χ is the shape factor, as seen in eqn (1). If resonance conditions are met (eqn (1)), and the metal's absorption ε''_{np} is small and positive, then $E(\lambda)$ reaches its maximum (λ_{LSPR}). In practical terms, this means that the extinction, and thus, its maximum λ_{LSPR}, can be tuned by acting on three fundamental parameters: size (a), shape (χ), and chemical identity of the nanomaterial ($\varepsilon_{np} = \varepsilon'_{np} + i\varepsilon''_{np}$). In particular, it can be observed that as the size and anisotropic character of nanoparticles is increased, their λ_{LSPR} is also increased (*i.e.*, red shifted), while doping, defect engineering, and hybridization can be exploited to fabricate novel nanomaterials with native NIR and SWIR activity (Fig. 2).

Although the relationships between the above listed parameters and the optical properties of nanoparticles have been extensively investigated in the past twenty years, and a lot of energy has been put into improving size and shape control at the nanofabrication level, there are still some criticalities that make substrate tuning a non-trivial task. For example, reaching morphological uniformity and high morphological yield of anisotropic substrates, especially in surfactant-free systems, still represents a challenge in current practice. Surfactant-free systems are particularly interesting for *direct detection* applications; while nanoparticle capping is unavoidable in any colloidal system,[51] the presence of strongly interacting shape-directing surfactants (*e.g.*, cetyltrimethylammonium bromide, CTAB) at the solid/liquid interface of an enhancing substrate can interfere with measurements by increasing the distance at which the analyte can interact with the SERS-active surface.[52,53]

SERS is indeed a distance-dependent phenomenon that relies on the adsorption of analytes on or in close proximity to plasmon-sustaining nanostructures (within 1 nm for maximum enhancement, within 3 nm for lower, longer-range enhancement)[54] to achieve their detection.[55,56] In thermodynamic terms, adsorption will happen if the association constant, K_{ad}, between the analyte and the nanostructured surface is larger than all of the other constants at play, namely, K_{ad} between substrate and stabilizers, substrate and nanofabrication by-products, and between individual analyte molecules.[53] When the system does not allow for adequate adsorption of an analyte for its direct detection, or when a very complex matrix has to be dealt with (*e.g.*, biological fluids, cells, tissues) and high selectivity and specificity are required, *indirect* detection strategies must be utilized instead.

Indirect detection by SERS is effected by means of functionalized nanoparticles, called SERS *nanotags*, that allow for the switching on and off of a signal given by a *reporter* molecule, upon folding, binding, or other recognition event. Differently engineered nanotags in the same colloidal sol or assay[57–59] can then be exploited for multiplexing, allowing for the concomitant indirect detection or imaging of different analytical targets during the same measurement. For this approach to be successful, the reporter molecule must be carefully selected,

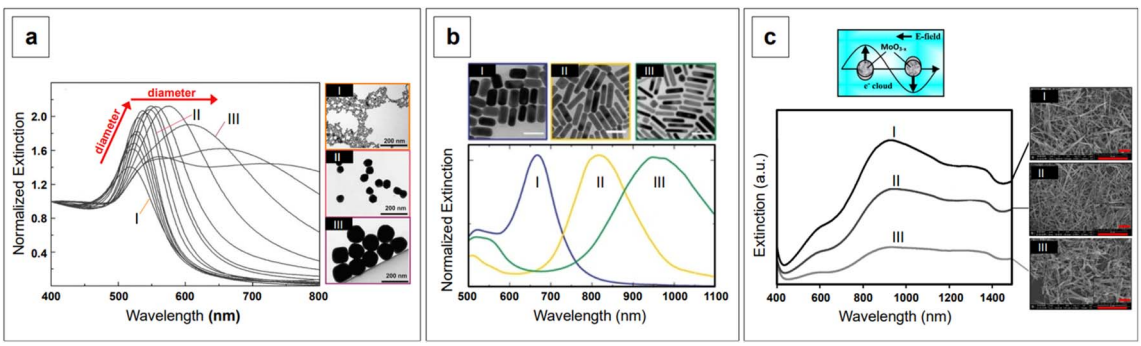

Fig. 2 Effect of size, shape, and dielectric function on the plasmon band of nanomaterials. (a) The λ_{LSPR} of citrate-reduced gold nanospheres widens and shifts to the red and NIR as the size increases from 8.4 ± 1.0 nm (I), to 64.8 ± 3.4 nm (II), and 123.6 ± 10.6 nm (III). Adapted with permission from Bastús *et al.*, *Langmuir*, 2011, **27**, 11098–11105. Copyright 2011 American Chemical Society. (b) Nanorods show two plasmon bands, corresponding to the transverse (~500 nm) and longitudinal components. The wavelength of the latter increases with increasing aspect ratio (AR): gold nanorods having AR of 2 ± 1 show a longitudinal λ_{LSPR} at about 660 nm (I, blue), those with AR of 4.2 ± 1 show a longitudinal λ_{LSPR} at about 810 nm (II, yellow), and those with AR of 6 ± 2 show a longitudinal λ_{LSPR} at about 960 nm (III, green). Scale bars in the TEM micrographs are 50 nm. Adapted with permission from Springer Nature: Zijlstra *et al.*, *Nature*, 2009, **459**, 410–413. Copyright 2009. (c) Extinction spectra of three NIR-active MoO_{3-x} nanomaterials with different oxygen vacancies and corresponding Field Emission SEM (FE-SEM) micrographs. Adapted with permission from Patil *et al.*, *J. Phys. Chem. C*, 2020, **124**, 21082–21093. Copyright 2020 American Chemical Society.

© 2023 The Author(s). Published by the Royal Society of Chemistry

Open Access Article. Published on 22 March 2023. Downloaded on 4/4/2023 3:23:28 PM. This article is licensed under a Creative Commons Attribution-NonCommercial 3.0 Unported Licence.

such that it can be easily conjugated to the metal core of the nanotag, and it can give off a bright signal, even at trace concentrations. This implies that a good reporter for SERS nanotags must have a large SERS cross section. While in the visible and NIR I range a wide array of large cross section reporter molecules is available (crystal violet, rhodamine 6G, and 4-mercaptobenzoic acid among others), bright NIR II and SWIR reporters for SERS are scarce and research on their design and synthesis is still ongoing and niche.

Lastly, we recall that by avoiding self-absorbance, NIR light can penetrate tissues, reaching about 1 cm of depth when 785 nm lasers are utilized.[60] Increasing wavelengths into the NIR II and SWIR further improves transparency at such depths by concomitantly reducing scattering.[61,62] However, such an extent of penetration depth might not be sufficient for applications that require non-destructive access to deeper targets within the human body, such as abdominal organs or intracranial regions. This issue clearly limits the range of application of NIR-SERS to the medical and intraoperative fields. Traditional Raman spectroscopy can benefit of alternative spectral collection arrangements, such that the radiation can reach deeper targets. This variation of the technique is called Spatially Offset Raman Spectroscopy (SORS), and its Surface Enhanced (SE) counterpart, SESORS, can be similarly implemented, affording depths of penetration from 4 to 5 cm.[63] As a consequence, this spectral collection configuration brings about new and complex challenges in that, for a SERS signal to be generated by a deep target, a suitable enhancing substrate must be delivered *in its vicinity*. Therefore, nanoparticle dose, delivery method, biocompatibility, toxicity, and clearance are all aspects that must be carefully evaluated when implementing a realistic SESORS analytical protocol.

In the following sections, we will explore how the challenges herein outlined have been tackled by the SERS community, providing examples of relevant literature from the past six years (2017–2022). While there is a broad range of recent reviews on SERS,[64,65] especially on substrates[66–70] and biomedical applications,[71–78] we intend to offer a different take on the matter and focus on aspects that are seldom discussed, although within popular topics such as anisotropic growth. An example of these are surface chemistry and its relationship with crystal growth, monodispersity, and final SERS performance, as well as the insights coming from computational chemistry, which aid in the elucidation of mechanisms that are still experimentally elusive. We hope to guide the reader in a journey that illustrates the reasons behind certain practical choices presented by NIR-focused literature cases, and stimulate the debate around the criticalities that still need to be addressed to finally push (NIR-)SERS into the real world.

2.1 Excitation wavelength and nanomaterial design

As previously discussed, the use of NIR and SWIR excitation wavelengths necessarily implies some degree of intervention on the nanomaterial design, with respect to the most commonly utilized substrates for SERS in the visible range. Three main intervention strategies can be identified:

(1) acting on the anisotropy of the nanoparticle morphology to shift the LSPR to the NIR and SWIR regions;

(2) acting on the chemical composition (ε_{np}) and architecture of the nanomaterials (*e.g.*, core–shell, multimaterial hybridization, doping, *etc.*) to obtain novel SERS-active substrates in the NIR and SWIR;

(3) using NIR and SWIR reporters to obtain NIR and SWIR nanotags for indirect SERS detection.

2.1.1 Anisotropic plasmonic nanomaterials. The LSPR of a nanomaterial can be manipulated by increasing its *aspect ratio*, defined as the ratio between the in-plane width and the out-of-plane height of the nanostructure ($AR_{sphere} = 1$).[14] This increases the anisotropic character of the system and red-shifts the λ_{LSPR}. The simplest and most notable case of anisotropic nanoparticle is probably represented by gold nanorods, while in the last ten years branched nanoparticles, often referred to as nanostars, have taken the lead as the state-of-the-art morphology for bright SERS substrate fabrication. Besides the evident effects of anisotropy on the position of the plasmon resonance (Fig. 2b), these nanostructures also exhibit an inherent advantage that makes them brighter than traditional spheroidal nanoparticles—the *lightning rod effect*.

This effect entails the accumulation of dipolar fields at the tips of prolate structures, such as the tips of nanorods or nanostar branches, resulting in electric fields that are much more intense than those at flattened regions.[31] Since plasmonic nanostructures behave like nano-antennas, in that the radiative process from the nanostructure (*i.e.*, near-field) to the far-field is what ultimately enables SERS (*electromagnetic mechanism*),[56] it follows that a radiative process that is generated by stronger electric fields will generate inherently larger surface-enhanced Raman signals. In other words, the tips of rods or branches are intrinsic hotspots.[31,79–82] Additionally, the more a prolate geometry is needle-like, the higher the concentration of dipolar fields, and thus, the larger the resulting signal enhancement.[80] This can be easily observed in Fig. 3a, which shows the NIR-SERS spectra (λ_{exc} 785 nm) of standard probe crystal violet, obtained utilizing AuAg nanostars with varying degrees of branch sharpness, as well as AuAg nanospheres.[83] All nanostars give raise to a larger amplification of the signal compared to nanospheres, and among the nanostars, the intensity of the spectra is positively correlated to the sharpness of the branches.

The intrinsic hotspots of rod-like or rod-containing (*i.e.*, branched) colloidal nanoparticles are such that, under suitable excitation conditions, they may be used for SERS measurements without need for prior aggregation.[84] This constitutes an advantage in terms of signal reproducibility, in that the more common extrinsic (*i.e.*, salt-induced) hotspots are inherently stochastic, as stochastic is also the probability of a molecule adsorbing on a hotspot.[85] An interesting way of generating extrinsic hotspots in a more controlled way was recently implemented by Huang *et al.*,[86] who coupled label-free gold nanostars with gold nanohole arrays for the single molecule NIR-SERS detection of both individual DNA bases and single nucleobases within DNA oligonucleotides. Gold nanoholes were size-tuned and suitably spaced to exhibit their LSPR in the NIR I, and then embedded as a partitioning wall in a PDMS

Open Access Article. Published on 22 March 2023. Downloaded on 4/4/2023 3:23:28 PM.
This article is licensed under a Creative Commons Attribution-NonCommercial 3.0 Unported Licence.

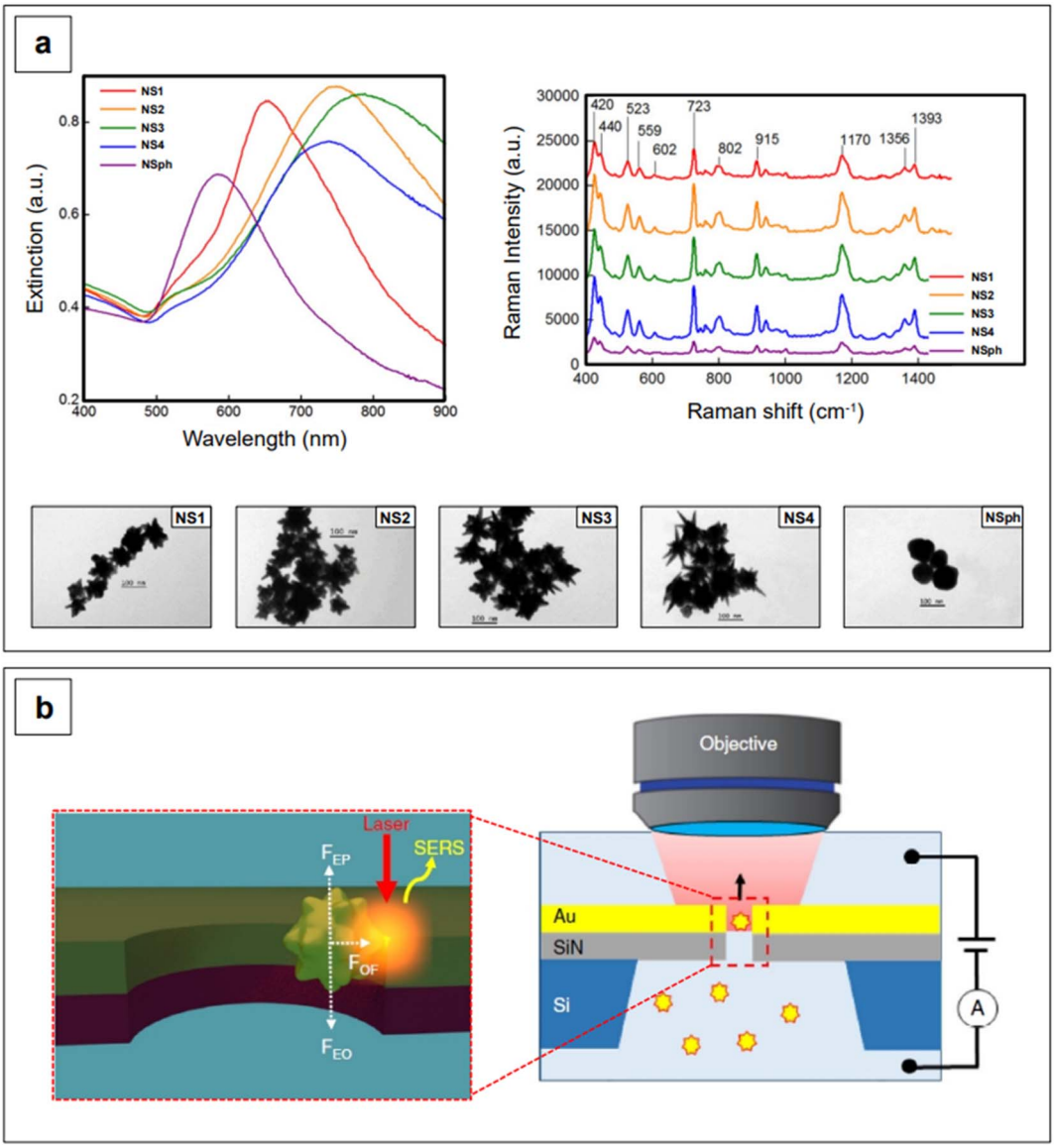

Fig. 3 (a) Extinction spectra (left) and TEM micrographs (bottom) of AuAg nanostars with varying degrees of branch length and sharpness (NS from 1 to 4), and of AuAg nanospheres (NSph). The capping agent is CTAB for all colloidal formulations. These nanomaterials were utilized for the NIR-SERS detection of model analyte crystal violet at a final concentration of 1 μM (right). It can be easily observed that all branched morphologies give rise to intense SERS spectra compared to the nanospheres, and that the sharpest morphologies yield strongest SERS signals among the branched morphologies (*lightning rod effect*). Adapted with permission from He *et al.*, *J. Opt.*, 2015, **17**, 114013–114026. Copyright IOP Publishing. All rights reserved. (b) Schematic of the flow-through detection platform developed by Huang *et al.* A nanostar is trapped in a nanohole *via* the application of a voltage and laser illumination at 785 nm. The trapping is the result of the combination of electrophoretic (F_{EP}), electroosmotic (F_{EO}), and optical (F_{OF}) forces and allows for the formation of on-demand, controllable tip-wall hotspots. Adapted from Huang *et al.*, *Nat. Commun.*, 2019, **10**, 5321; figure licensed under CC BY 4.0, https://creativecommons.org/licenses/by/4.0/.

microfluidic chamber. Gold nanostars were then incubated with either the individual DNA bases or the DNA oligonucleotides and let diffuse from one compartment to the other inside the microfluidic chamber. By concomitant application of a 785 nm laser light and an electrical potential, a plasmonic gradient inside the nanohole and two equal and opposing electrokinetic and electroosmotic forces are generated, respectively (Fig. 3b). The plasmonic gradient gives rise to an optical force that brings the nanostar-analyte complex towards the nanohole sidewalls, creating on-demand, controllable tip-wall hotspots in which the analyte can reside. On the other hand, the combined effect of the two equal and opposing electrokinetic and electroosmotic forces causes the electrophoretic motion and entropic flow of the nanostar through the nanohole to be abated. This electro-opto-kinetic trapping and on-demand hotspot manipulation can be sustained up to a few minutes, allowing for sufficient time to detect rare single molecule events (*e.g.*, the detection of A as a single nucleobase in 5′-CCCCCCCCCA-3′) across multiple acquisitions.

© 2023 The Author(s). Published by the Royal Society of Chemistry

Open Access Article. Published on 22 March 2023. Downloaded on 4/4/2023 3:23:28 PM. This article is licensed under a Creative Commons Attribution-NonCommercial 3.0 Unported Licence.

Oblique Angle Deposition (OAD) can also be utilized to fabricate planar substrates based on anisotropic elements *and* with controlled spatial distribution of hotspots. Li *et al.*[87] developed an OAD-based gold nanorod planar substrate with nanorod spacing optimized to be active in the NIR I, and applied it to the fast (8 minutes), label-free, and direct detection of the protective antigen (PA) produced by *Bacillus anthracis* upon anthrax infection.[88] Their method was demonstrated to have a sensitivity of 100 pg mL^{-1} both in standard solutions and in human serum albumin (HSA), and discrimination of HSA from HSA/PA mixtures was aided by principal component analysis (PCA).[88] Although real serum samples contain species other than HSA, the determined limit of detection is four orders of magnitude lower than the typical levels of protective antigen found in infected human serum, and, thus, reasonably fit-to-purpose.[88]

The anisotropic arrays described by Li *et al.*[87,88] are not the most common type of SERS-ctive substrate; in fact, colloidal suspensions have a much wider prevalence in analytical work, due to their low cost and versatility. Colloidal nanoparticles can be delivered *in situ*,[89] incubated into cells or injected through tissues,[90,91] utilized for measurements in transmission configuration,[92] and immobilized on planar supports to produce arrays.[93–95] However, the elucidation of the mechanisms that enable anisotropic growth in colloidal sols is still subject of animated debate and research, in that several factors limit the realistic formulation of a punctual and unambiguous unified theory. While the growing accessibility of computational methods such as molecular dynamics simulations has recently aided in the exploration of otherwise inaccessible nanoscale phenomena, the real-time atomic-scale imaging and chemical mapping instrumentation that would be requisite to observe such processes *directly* and in their *native* environment is not widely accessible yet (*e.g.*, cryogenic transmission electron microscopy, cryo-TEM), or existent. Furthermore, the enormous number of different synthetic protocols that have been implemented in the last two decades poses in and of itself a limitation to the extent of the reaction space parameters that can be realistically explored and compared experimentally. However, from a strictly practical standpoint, it is well known that anisotropic gold and silver nanoparticles can be achieved *via* the introduction of *shape-directing agents*, and their rational modulation allows fine plasmonic tuning for tailored NIR-active substrates. Shape-directing agents can be categorized into two groups—surfactants and small ions (*i.e.*, silver and halides). In the case of gold nanorods, both agents are utilized for the control of the aspect ratio for plasmon tuning, as well as for morphological yield and crystallinity control.

CTAB is probably the most famous among the shape-directing surfactants and it is essential in the fabrication of nanorods. The general mechanism by which it assists in the formation of these nanoparticles is understood to be the result of the different affinity the surfactant has towards different Au facets, such that growth on the longitudinal axis is faster than on the transverse axis, leading to rod-shaped nanoparticles.[96,97] As previously mentioned, advances in the field of computational chemistry have recently allowed for the elucidation of mechanistic aspects that are otherwise experimentally elusive. Of particular importance is the modeling of surfactants as micelles and the study of their behavior at the interface with nanoscale plasmonic surfaces in solution. For example, molecular dynamics simulations by Meena and Sulpizi[98] and Da Silva and Meneghetti[99] have shown that the adsorption of CTAB on the seed and growing nanorod likely occurs as individual micelles. In analogy to what postulated in the early developments of nanorods synthesis,[96,97] CTAB micelles adsorb with different packing density depending on the crystal facet and surface curvature.[98–100] This creates facet- and curvature-specific intramicellar channels of varying width, where the solution environment can easily reach the surface of the seed or growing rod.[98–100] This affects the growth kinetics and ultimately results in a faster deposition of reduced gold on the facets that are less densely packed by the CTAB micelles (*i.e.*, curved, (111) facets).[98–100]

The event that breaks the symmetry of the initial isotropic gold seed is not generally attributed to CTAB.[94] For penta-twinned nanorods, this event is identified with the stochastic formation of twinning planes in the growing seed,[101] while for single-crystal nanorods, which are obtained in the presence of silver, the general belief is that silver itself is responsible for symmetry breaking.[102–105] Because symmetry breaking is an inherently stochastic process, more families of nanorods inevitably coexist in the same colloidal sol ("*popcorn*" *mechanism*),[106] thus affecting its homogeneity. Colloidal polydispersity is reflected by the width of the longitudinal LSPR band in extinction spectroscopy, and it is generally associated to a non-optimal batch to batch reproducibility of the SERS enhancement. This issue has been addressed by Liz-Marzán's group,[107] who introduced the use of small AR nanorods as seeds. This variation in the original procedure causes an effective temporal and spatial decoupling of symmetry breaking and growth events, thus leading to an improved morphological homogeneity and reproducibility of the SERS signal.[107] This is an elegant example of how the understanding of fundamental nanoscale processes can lead to very practical outcomes at the analytical level. The necessary high yield and uniformity of the rod-shaped seeds was achieved by the introduction of *n*-decanol as a co-surfactant;[107] by finely tuning the *n*-decanol : CTAB ratio, growth of low-dispersion, higher aspect ratio nanorods was achieved (Fig. 4a).[107] It must be recalled that the possibility of utilizing co-surfactants to obtain nanorods with higher AR, and thus NIR II activity, was found also early in the nanofabrication development of this morphology,[96] although with lower shape uniformity, which is reflected by the wide longitudinal LSPR band (Fig. 4b).

A practical advantage of the nanorods developed by Liz-Marzán's group is that they are characterized by narrow longitudinal LSPR bands that can be straightforwardly tuned from the NIR I (760 nm) to the NIR II (1125 nm), by simple manipulation of the pH *via* HCl : $HAuCl_4$ ratio, from 40 to 160, and control of the reaction temperature at 16 °C.[107] The combination of a lower pH, which decreases the redox potential of ascorbic acid, and a lower temperature (T < room T) slows the kinetics of the growth reaction, thus achieving a more controlled

Open Access Article. Published on 22 March 2023. Downloaded on 4/4/2023 3:23:28 PM.
This article is licensed under a Creative Commons Attribution-NonCommercial 3.0 Unported Licence.

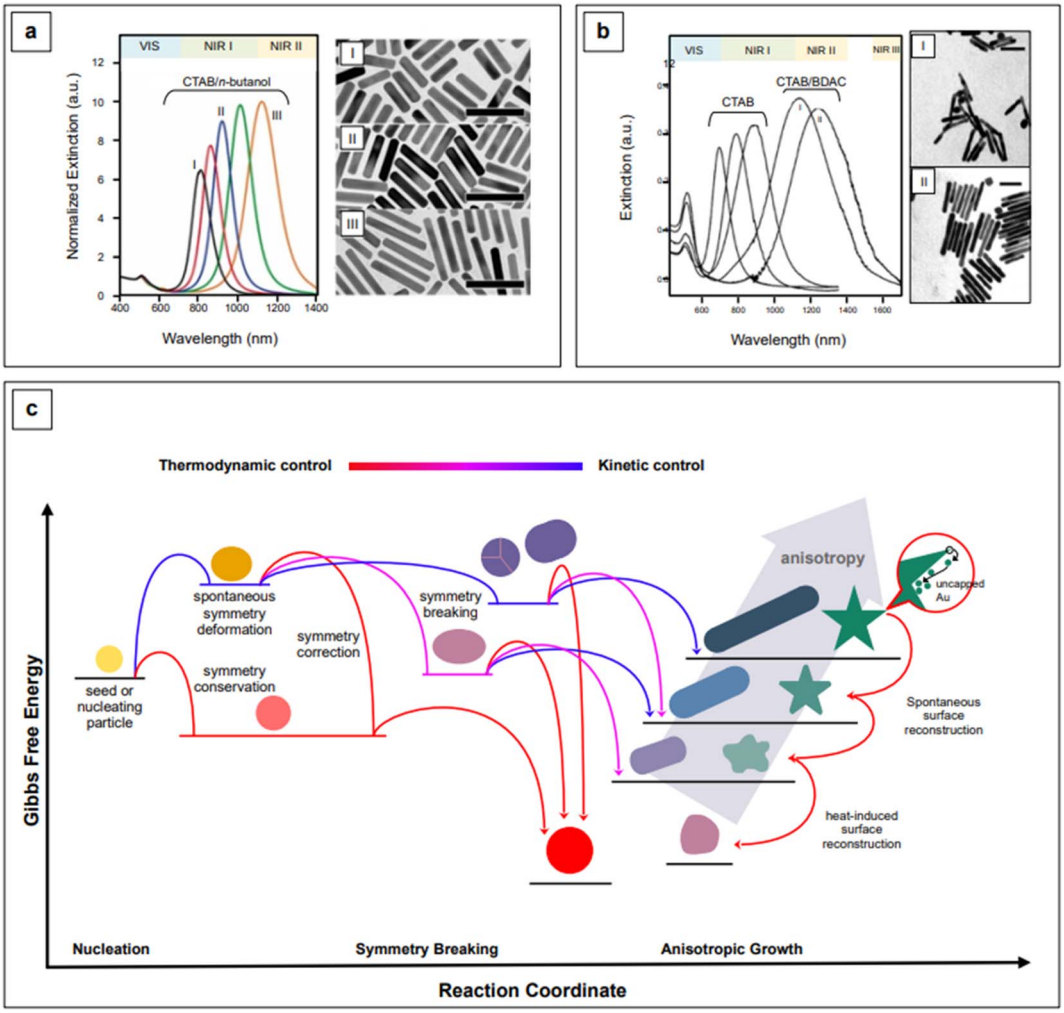

Fig. 4 Comparison between high aspect ratio nanorods synthesized in co-surfactant mixtures with (a) small anisotropic seeds and (b) traditional, spherical seeds. Panel a adapted with permission from González-Rubio *et al.*, *ACS Nano*, 2019, **13**, 4424–4435. Copyright 2019 American Chemical Society; panel b adapted with permission from Nikoobakht *et al.*, *Chem. Mater.*, 2003, **15**, 1957–1962. Copyright 2003 American Chemical Society. (c) Kinetic *vs.* thermodynamic control in nanoparticle growth. Figure inspired by González-Rubio *et al.*, 2020.[110]

manipulation of anisotropy.[107,108] Anisotropic morphologies are indeed kinetic products (Fig. 4c),[109,110] and reaction kinetics strongly influences the morphology and morphological yield of the final product. As previously noted, differences in thermodynamic parameters, such as the affinity of a particular capping agent for a specific crystal facet, do have kinetic outcomes—a more strongly bound or more tightly organized capping agent can slow down the deposition rate of the precursor noble metal.[99,100,107] This has been recently demonstrated by Chen *et al.*[111] for the formation of silver nanocubes with (poly)vinylpyrrolidone (PVP) as the shape director. For pentatwinned gold nanorods, Sánchez-Iglesias *et al.*[112] have further explored the topic by achieving aspect ratio tuning in the NIR I and II *via* the sole temperature control, in the presence of CTAC as CTAB's co-surfactant.

If the elucidation of anisotropic growth in nanorods still proves to be challenging, the elucidation and fine control of the development of branched morphologies are even more elusive. Branched nanoparticles, often called nanostars (but also *nanourchins*[113–115] or *nanoflowers*[116–118]), are typically synthesized *via* seed-mediated processes, in the presence of silver ions from silver nitrate, as well as a surfactant or a polymer (*e.g.*, CTAB,[119,120] Triton-X,[121–123] anionic dioctyl sodium sulfosuccinate, AOT, and AOT/dimethyldodecylbenzylammonium bromide,[124] PVP,[125,126] chitosan,[127,128] *etc.*). While the role of silver is understood to be—at a minimum—that of a symmetry breaking agent like with nanorods, the role of the various surfactants and polymers has not been fully elucidated yet. This is to be attributed not only to the low accessibility and affordability of *in situ* atomic-scale organic phase-compatible characterization techniques, but also to the high degrees of freedom that this morphological class inherently bears. Compared to nanorods, where the morphological parameters are essentially circumscribed to length and width, nanostar subclasses can be identified based on a wider range of parameters, such as the length and thickness of branches, their sharpness, their number, the presence or absence of tip decorations. This readily translates to an enormous number of variations along the same

© 2023 The Author(s). Published by the Royal Society of Chemistry

Open Access Article. Published on 22 March 2023. Downloaded on 4/4/2023 3:23:28 PM.
This article is licensed under a Creative Commons Attribution-NonCommercial 3.0 Unported Licence.

fundamental shape (Fig. 5), and thus, an accompanying enormous number of synthetic protocols that can be hardly rationalized for mechanistic purposes. However, by analogy with what has been illustrated for nanorods and for anisotropic growth in general, it can be said that a combination of selective adsorption,[121] configuration at the solid/liquid interface,[129] and modulation of redox potentials and reaction kinetics[53,109,123] is likely to compound in the generation of a specific branched nanoparticle.

An important difference compared to nanorods is that surfactant-free procedures for the fabrication of colloidal gold nanostars can also be implemented,[83,113,130–133] indicating that surfactants are not as necessary as in the fabrication of nanorods. In fact, while surfactant-free nanorods can be obtained only in the presence of a template,[134,135] this is not necessary for the surfactant-free synthesis of gold nanostars; rather, a quick look at the literature might suggest that the only indispensable reagent is silver. It has indeed been amply shown that, regardless of the synthetic strategy (*i.e.*, surfactant-mediated or surfactant-free, seed-mediated or one pot), the removal of silver from branched gold nanoparticle syntheses can lead to the formation of spheroids.[83,123,131,136] This has been reconducted to the role of silver in inducing anisotropy-favoring twinning defects on the nucleating crystals or growing seeds.[53,123]

However, a more accurate look at the literature would show that synthetic protocols for the fabrication of branched gold nanoparticles can also be achieved without silver, often in association with reducing agents different than ascorbic acid.[113,130,132,137] This demonstrates the previously mentioned complexity of this type of growth, and the difficulty in finding a unifying mechanistic theory. However, when silver is utilized, it has been frequently observed to influence the branches extent, length, and sharpness[83,123,131,136,138,139]—an effect that is important for NIR and hotspot tuning.[83] Moreover, as observed in the stabilization of symmetry-breaking outcomes in the evolving seed in nanorod synthesis,[103,104] silver has been associated to the stabilization of shape *via* underpotential deposition.[123]

As previously discussed, anisotropic nanoparticles are kinetic products,[109,110] and they have a higher density of high energy facets (*i.e.*, {110} and {100}) compared to isotropic shapes such as spheroids, as well as a larger number of low coordination surface atoms.[140] Therefore, their formation and the retention of their shape and crystallinity is not thermodynamically favored, thus leading to surface reconstruction

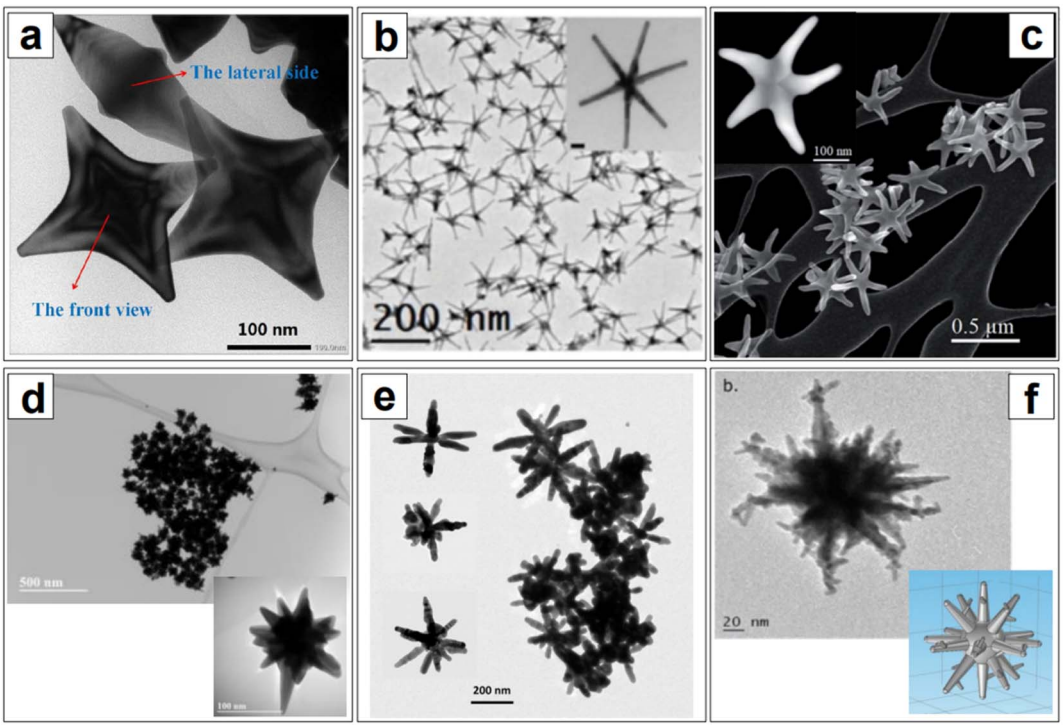

Fig. 5 Examples of branched nanoparticles. (a) Highly symmetrical and homogeneous Ag-coated gold tetrapods. Reprinted from *Spectrochim. Acta Part A*, **211**, Zhu *et al.*, 154–165, Copyright 2019, with permission from Elsevier. (b) Highly symmetrical and homogeneous six-branches AuAg nanostars. Used with permission of Royal Society of Chemistry, from Atta *et al.*, *Nanoscale*, **11**, 2019; permission conveyed through Copyright Clearance Center, Inc. (c) Gold-copper starfish-like nanostars. Adapted from Sanchez *et al.*, *RSC Adv.*, 2021, **11**, 25788–25794; figure licensed under CC BY-NC 3.0, https://creativecommons.org/licenses/by-nc/3.0/. (d) Citrate-capped one-pot multibranched AuAg nanostars. Adapted with permission from Deriu *et al.*, *J. Phys. Chem. C*, 2022, **126**, 2023–2040. Copyright 2022 American Chemical Society. (e) Predominantly hexapod silver nanostars. Reprinted from Garcia-Leis *et al.*, *Colloids Surf., A*, **535**, 49–60, Copyright 2017, with permission from Elsevier. (f) Branches-on-branches gold nanostars. Adapted with permission from Atta *et al.*, *J. Phys. Chem. C*, 2016, **120**, 20749–20758. Copyright 2016 American Chemical Society.

Open Access Article. Published on 22 March 2023. Downloaded on 4/4/2023 3:23:28 PM. This article is licensed under a Creative Commons Attribution-NonCommercial 3.0 Unported Licence.

(Fig. 4c).[123,140] This phenomenon is particularly evident in gold anisotropic nanoparticles, due to the known high mobility of this element.[123,141] Atta *et al.*[123] studied the fate of silver in the evolution of highly uniform, seed-mediated, six-branches gold nanostars in Triton X-100, and found that their morphology, and thus the LSPR, was stable when an optimal concentration of 100 μM $AgNO_3$ was utilized for their nanofabrication. In all other instances, a decrease in the length of the spikes and rounding of the tips was observed. Line-scanned energy-dispersive X-ray spectroscopy (EDS) data of the nanostars obtained with varying Ag^+ concentration showed that silver is uniformly present throughout the nanoparticle, but only forms a thicker layer on the side walls of the branches when 100 μM is used; this is believed to prevent the thermodynamically favored diffusion of gold atoms from the tips towards the core, thus allowing shape retention.

Nanoparticle restructuring towards more thermodynamically favored shapes was also noticed in the surfactant-free gold nanostars optimized by Xie *et al.*,[137] in which silver is absent, and in those optimized by He *et al.*,[83] in which silver is present as a trace constituent (Au : Ag of 18 : 1). In these cases, boiling and aging, respectively, blueshift the plasmon, indicating the collective regression of the nanoparticle population to spheroids or a less anisotropic shape.[83,137] Thermally induced restructuring of *individual* plasmonic nanostars was recently observed *in situ*, thanks to the advances in electron microscopy cells with both heating and tilting capability.[142] These were utilized in the development of a scanning TEM (STEM) acquisition method based on the collection of high angle annular dark field (HAADF) 2D projections of individual nanostars and consequent 3D shape reconstruction (HAADF-STEM tomography). The novelty of this method is that it can be performed at a rate that is 10 times faster than conventional electron tomography approaches, thus allowing the direct observation of individual nanostars *during* temperature-induced reshaping.[142] During these *in situ* heating experiments, it was directly observed for the first time that gold atoms migrate from the tip of the branches towards the core of the nanostar as a function of increasing temperature, and that the majority of the reshaping occurs within the first minute of heating, regardless of the temperature.[142]

Because of the tight relationship between morphological and optical properties in plasmonic nanoparticles, and because laser illumination during a SERS experiment might cause plasmon-induced heating, heat-mediated shape restructuring of nanoparticles should be taken into serious consideration. This is particularly true when implementing NIR-SERS analytical protocols, as they are likely to make use of highly anisotropic morphologies in conjunction with high energy and long acquisition times (*i.e.*, to counterbalance the energy dependence of the signal intensity), which tend to generate heat within the sample.

Regardless of applied heat, surface restructuring of highly anisotropic nanoparticles is thermodynamically favored, and a common strategy to hinder and slow down the process is the use of surface ligands. Besides modulating colloidal stability, surface ligands can indeed minimize surface energy. Shape conversion of gold nanostars can thus be prevented by capping them with strongly interacting surfactants, such as CTAB,[83] weakly chemisorbed small molecules such as citrate,[53,143] or other ionic species such as HEPES[129] and carbonate.[53] It must be recalled that the choice of nanoparticle capping agents is not only critical for the retention of shape and colloidal stability,[53,140] but also for optimal signal enhancement[53] and biocompatibility.[144,145] The relevance of the latter aspect will be apparent in Sections 2.1.3 and 2.2 of this review.

The nanoparticles developed by Atta *et al.*[123] are of particular interest in the NIR as they have very thin and long branches, which shifts the plasmon from the usual NIR I to the NIR II, offering the possibility to explore the second biological window. The second biological window and the SWIR region are seldom explored compared to the NIR I, not only because of the technological limitations that we have previously discussed (*i.e.*, performance of NIR I and SWIR detectors), but also because highly homogeneous and controlled thin branching are difficult to obtain, and there is at present little to no knowledge on how to tailor this shape such that no core ripening or thickening of the branches occurs during growth (besides impeding restructuring). Atta *et al.*[123] also observed how, beyond the optimal silver concentration they found for their synthetic protocol, silver deposited at the core, enlarging it. Moreover, it has been observed that the seed size also influences the branching extent and individual branch growth.[146,147]

In gradient array growth experiments on planar substrates that were intended to unveil the morphological transition of poly(*N*-isopropylacrylamide)-encapsulated gold seeds into silver-free nanostars, Kuttner *et al.*[147] observed that new branches are formed at the expense of branch growth with increasing seed diameter, which was attributed to the progressively larger surface that was available for autocatalytic reduction, and thus, for the nucleation of new branches. The same authors also studied the interplay of seed size with the concentration of gold precursor, noticing that for bigger (>12 nm) seeds to grow into longer-branched nanostars and counteract an overall isotropic growth in volume, a gold precursor supply higher than the usual 0.25 mM concentration was necessary.[147] After prior screening of SERS efficiency using model analyte nitrothiophenol, and identification of a nanostar morphology along the gradient array that was best suited for NIR I 785 nm irradiation, Kuttner *et al.*[147] were able to exploit the encapsulated nanoparticles as hydrophobic platforms for the label-free surface enhanced *resonance* Raman (SERRS) detection of the elusive *Pseudomonas aeruginosa* infection biomarker pyocyanin. This was achieved *via* a tempering-promoted entrapment of the analyte at the nanoparticle-polymer interface, which allowed poly(*N*-isopropylacrylamide) to undergo volume-phase transition without altering the optical properties of the encapsulated nanostars, thus enabling pyocyanin detection at clinically relevant concentrations (dynamic range 10^{-5} to 10^{-7} M) by bringing it closer to the plasmonic surface.[147]

Label-free SERS, that is, SERS in the absence of nanotags, can be challenging for the reasons illustrated in the overview section of this review; in fact, the majority of recent works on

 © 2023 The Author(s). Published by the Royal Society of Chemistry

Open Access Article. Published on 22 March 2023. Downloaded on 4/4/2023 3:23:28 PM.
This article is licensed under a Creative Commons Attribution-NonCommercial 3.0 Unported Licence.

NIR-SERS, and in particular those targeted at the detection of biomolecules in complex biological media, are characterized by the use of *functionalized* anisotropic nanoparticles. A selection of these anisotropic nanotag-based studies will be discussed in the dedicated section. It must also be mentioned that, although the present section is focused on the examination of nanorods and nanostars, these are not the only morphologies available to the SERS scientist. Other anisotropic materials with fit-to-purpose SERS activity in the NIR can also be fabricated. For example, interested readers can refer to the works on NIR-active silver nanowires by Becucci *et al.*[148] and on gold nanoplates by Luo *et al.*,[149] or the synthetic study on the role of iodide ions in the transition of copper nanowires to nanoplates by Kumar's group.[150]

2.1.2 Alternative plasmonic nanomaterials. So far, our discussion has involved the sole use of noble metal nanoparticles—as we have delineated, they are the most commonly utilized substrates for SERS, and the manipulation of their morphology represents a way to access the NIR domain. As previously mentioned, another way to access the NIR and SWIR regions is to act on the ε parameter in eqn (2), and utilize materials other than gold and silver, with native properties in these spectral ranges. The intrinsic ability of a material to display LSPR in the NIR can be explained in terms of the Drude model,[151,152] according to which the frequency of the LSPR of a nanomaterial, ω_{LSPR}, is given by:[153]

$$\omega_{LSPR} = \sqrt{\frac{{\omega_p}^2}{1 + 2\varepsilon_{env}} - \gamma^2} \quad (3)$$

where ω_p is the plasma frequency and γ is the damping factor, which contains information about the size and shape. Since the plasma frequency is directly proportional to the electron density,[153] choosing materials with lower electron density than gold and silver shifts the plasmon to lower frequencies, and thus, longer wavelengths. Semiconductors are one of the most sought-after candidates for use as alternative SERS substrates in that, by definition, they have lower electron density compared to metals. Moreover, they typically have good chemical stability, cost-effectiveness, they can be fabricated *via* facile syntheses, and are easily tuneable both in terms of morphology and surface chemistry.[154–156]

However, what constitutes the main advantage of using semiconductors as SERS substrates is also their main challenge. The LSPR bands generated by these materials are not as intense as those observed for noble metals, as semiconductors intrinsically have scarce electrons in the conduction band.[157] Consequently, they have a very low enhancement factor (10 to 10^2) compared to the commonly used noble metals (10^6 to 10^{10}).[158] It must be recalled that the overall SERS enhancement is understood to be the product of two different phenomena, the electromagnetic effect, cited in the preceding section, and the *chemical effect*, of which charge transfer is the main enabling mechanism. Charge transfer is an analyte-specific mechanism that entails a chemical interaction between the analyte and the SERS substrate, in which an electron can be transferred through vibronic coupling from the Fermi level of the substrate (*i.e.*, metal) to a frontier orbital of the analyte molecule, or *vice versa*.[159] While this phenomenon does not account for the majority of the total enhancements observed in SERS using traditional plasmonic nanomaterials, it represents instead the main mechanism by which semiconductor-based SERS is enabled. Because the comparatively weaker signal obtained by semiconductors is due to their low electron density, and thus, low amount of charge transfer from the valence to the conduction band, the biggest challenge for the direct implementation of semiconductors in SERS is to engineer them such to improve and promote the chemical enhancement.

To achieve this materials engineering objective, the possible ways in which charge transfer can occur must be taken into consideration. These can be broadly classified into three types: (1) movement of electrons within the atoms of semiconductor, (2) electronic excitations in the target molecule, and (3) mutual transfer of electrons between the semiconductor and target molecule by photo-induced charge transfer (PICT).[157] While the exploitation of the latter mechanism is self-explanatory, the first two need some clarification. The transfer of electrons within the semiconductor depends on their band gap, density of electrons in the valence and conduction bands, and on the wavelength of incident light. Similarly, the transfer of electrons in the target molecule depends on the highest unoccupied molecular orbital (HOMO) and the lowest unoccupied molecular orbital (LUMO). Upon excitation, electrons from the ground state (HOMO) transit to a higher energy level (LUMO); these electrons, being thermodynamically unstable, move back to the relaxed state in HOMO. The energy released in this process contributes to the Raman signal.[160] Based on this principle, the positions of the conduction and valence bands of a semiconductor can be adjusted to come close to the HOMO–LUMO of the target analyte, thus facilitating the charge transfer process, and with it, the SERS chemical enhancement.

Tailoring of the band gap of a semiconductor can be achieved in three main ways: by fabricating heterojunctions, through doping, and *via* defect engineering (Fig. 6). With *heterojunction*, we define the interface resulting from the coupling of two different semiconductors; this physical coupling not only tailors the energy level positions of the resulting material, but also facilitates SERS measurement by the formation of hotspots at the junctions. Doping is defined as the deliberate introduction of impurities into an *intrinsic* (*i.e.*, pure) semiconductor, thus modifying its chemical structure. This introduces additional energy levels in the resulting material, the *extrinsic* semiconductor, which can be exploited to facilitate SERS-enabling electronic transitions. Finally, defect engineering intervenes on the nanocrystal growth to introduce defects such as oxygen incorporation and abstraction. For applications in the NIR, the two most common tailoring strategies for semiconductor-based SERS are doping and defect engineering. Heterojunctions have been utilized in SERS applications, but their application is still primarily confined to the visible spectrum.[161–163]

Semiconductor nanoparticles can be obtained by a variety of bottom-up fabrication techniques,[164] such as precipitation,[165] template assisted,[166] hydrothermal,[160] and sol–gel[167] syntheses.

Open Access Article. Published on 22 March 2023. Downloaded on 4/4/2023 3:23:28 PM.
This article is licensed under a Creative Commons Attribution-NonCommercial 3.0 Unported Licence.

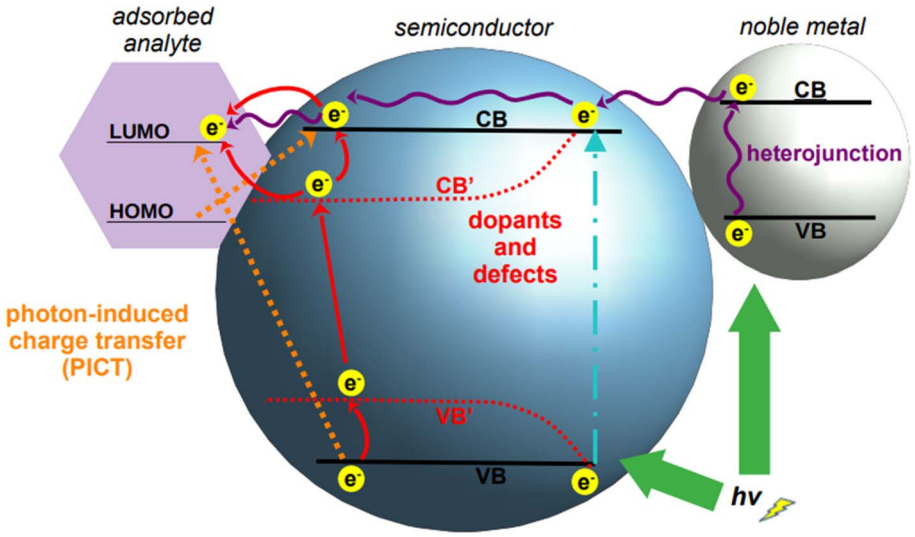

Fig. 6 Mechanisms of charge transfer increase in semiconductors. Upon suitable laser illumination, electrons in the native valence band, VB, of a semiconductor are transferred to the conduction band, CB (cyan dot-and-dash line); electrons in the conduction band can be increased by formation of a heterojunction with a noble metal (right), which feeds its electrons into the conduction band of the semiconductor. Charge transfer can then occur between the enriched conduction band of the semiconductor and an adsorbed analyte (purple wavy arrows). The introduction of doping agents and defects in the crystal structure of a semiconductor modifies the band structure of the resulting material, typically lowering the band gap ($\Delta_{CB'-VB'} < \Delta_{CB-VB}$). Upon appropriate laser illumination, electrons are transferred from VB to the new energy levels VB′ and CB′ and to the original CB. Depending on the relative position of the energy levels of the engineered semiconductor and those of the adsorbed analyte, charge transfer can occur from either CB or CB′ to the analyte (red arrows). A third mechanism can occur when electrons are transferred by photon-induction from the valence band of the semiconductor to the LUMO of the adsorbed analyte, or from the HOMO of the adsorbed analyte to the conduction band of the semiconductor (dotted orange arrows).

The same techniques can be utilized also for the doping of semiconductors by incorporation of dopant ions into the crystal lattice during nanoparticle growth;[168] alternatively, doping can also be achieved by post-synthetic methods such as diffusion or impregnation.[169,170] As depicted in Fig. 6, the introduction of dopants in the crystal lattice of semiconductors creates new energy levels, called sub-energy levels, thereby lowering the band gap. The specific position of the new energy levels and their proximity to the conduction or valence band depends on the charge and number of free electrons in the outermost orbital of the dopant ion. New sub-energy levels can also be achieved by doping-induced formation of defects in the crystal lattice, such as free electrons or electron holes.[160] In the case of free electrons, upon excitation they are trapped by the newly created intermediate bands, which prevent electron–hole recombination, thereby increasing the charge transfer.

To date, numerous studies have focused on the synthesis of doped semiconductor nanoparticles of controlled morphology with different concentration of dopant ions.[171] However, there is a huge gap between the high volume of literature on the synthesis of these materials, and the application of doped semiconductor nanomaterials for SERS detection. A recent effort to synthesize doped semiconductor nanomaterials for SERS detection was made by Wang and co-workers.[172] They doped ZnO oblong nanoparticles (d = 21–87 nm) with varying gallium content using a sol–gel method, and tested their SERS activity using 4-mercaptopyridine as the model analyte. As-synthesized ZnO nanoparticles exhibit a typical UV absorption band at 356 nm, which is attributed to band edge adsorption. By doping these nanoparticles with different concentrations of gallium, the authors were able to generate LSPR bands and tune them in the NIR, without intervening on the morphology, as it is generally done with standard plasmonic materials such as gold and silver. A doping concentration of 5% provided the maximum intensity of the SERS signal. The enhancement was mainly due to the charge transfer mechanism arising from the substitutional incorporation of the trivalent gallium in place of the divalent zinc, which allowed one electron from gallium to behave as a free charge carrier in the crystal lattice, thus producing the LSPR. These free electrons generate LSPRs up to 5% of gallium doping, after which the electron concentration saturates and the LSPR decreases. The enhancement factor (EF) for the detection of 4-mercaptopyridine at a doping ratio of 5% was 6.66×10^4.

Another study employed indium doping of CdO nanoparticles and tested their SERS activity with 4-mercaptopyridine molecules.[173] Indium-doped CdO nanoparticles were synthesized hydrothermally with varying amount of indium doping (0.025–0.200 atomic percentage) and it was observed that the charge transfer, as well as the morphologies of doped particles, is dependent on the doping concentration. With an In^{3+} doping content below 0.05, the nanoparticles formed polygonal shapes, which became more spherical with the increase of doping in the limit of 0.05. When the atomic percentage of doping was further increased (between 0.05 and 0.20), the nanoparticle morphology changed to a heterogeneous structure consisting of nanofibers embedded with 50–100 nm nanoparticles (Fig. 7a). High resolution XPS measurements of O 1s showed that doped

© 2023 The Author(s). Published by the Royal Society of Chemistry

Open Access Article. Published on 22 March 2023. Downloaded on 4/4/2023 3:23:28 PM.
This article is licensed under a Creative Commons Attribution-NonCommercial 3.0 Unported Licence.

and undoped CdO nanoparticles are characterized by a different distribution of oxygen species (oxygen vacancies, ionic oxygen, and surface oxygen, Fig. 7b). This is expected, as doping in metal oxides changes the electronic state of oxygen. Because of the absence of free electrons in the conduction band, bare CdO nanoparticles do not show any SERS signal. However, the additional energy levels generated *via* doping allowed for the production of a SERS signal (Fig. 7c). The observed enhancements were in the order of 10^3 (λ_{exc} 785 nm), with a degree of charge transfer that was maximized at the lower doping ratios that were tested (0.025–0.075, spectra from II to IV, Fig. 7c). The charge transfer mechanism was rationalized to arise from enriched electrons in the conduction band of the nanoparticle to the LUMO of the analyte, mercaptopyridine.

Doping for SERS purposes is often carried out to include plasmonic metals, such as silver or copper. The introduction of these metals causes an increase in the metallic character of the semiconductor, thus improving the ability of the final nanomaterial to elicit the SERS effect by concomitant electromagnetic and charge transfer mechanisms. An example of this type of doped semiconductors utilized for SERS detection in the NIR is the Ag-doped TiO_2 implemented by Zhou *et al.*[174] This doped material was then decorated with Ag nanospheres synthesized by sol-hydrothermal method to further enhance the SERS signal *via* their ability to yield an electromagnetic enhancement, and the formation of hotspots at the junctions between the main surface and the decorations. Interestingly, UV/Vis diffuse reflectance spectroscopy indicated that the reduction in the band gap of TiO_2 after Ag-doping was not sufficient to promote analyte-substrate charge transfer on its own. In fact, the 785 nm laser utilized for the measurements was found to cause charge transfer from the HOMO of the analyte to the lower energy level of the Ag/Ag-doped TiO_2 system, then to the conduction band of TiO_2, and finally to the LUMO of analyte (PICT mechanism).

It might be apparent now that metal oxides are among the most popular semiconductors. The engineering of their band gap is most frequently carried out by engineering defects such as oxygen vacancies. Haldavnekar *et al.*[175] utilized this strategy for the fabrication of undoped quantum sized ZnO with SERS capabilities. Quantum-sized (1.7–18.99 nm) ZnO nanoparticles were synthesized by a multi-photon ionization technique in which ZnO seeds were first created from bulk zinc by pulsed-laser ablation in the presence of atmospheric oxygen, and let self-assemble by melting, collision, and coalescence to form nanorods. The resulting nanomaterial was a hybrid system consisting of nanorods arranged as a ZnO nanodendritic platform, decorated with quantum sized ZnO nanoparticles on the top (Fig. 8a). The authors postulated that the high energy

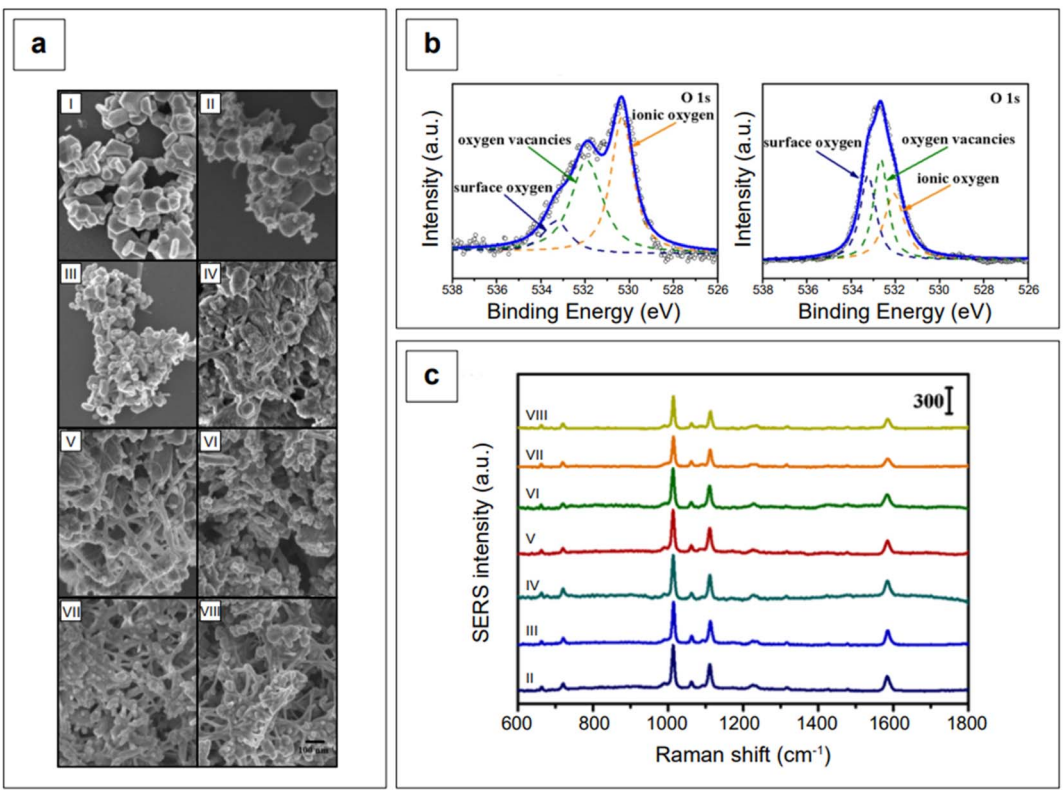

Fig. 7 (a) SEM micrographs of indium-doped CdO with varying In3+ atomic percentages: (I) $x = 0$, (II) $x = 0.025$, (III) $x = 0.050$, (IV) $x = 0.075$, (V) $x = 0.100$, (VI) $x = 0.125$, (VII) $x = 0.150$, and (VIII) $x = 0.200$. (b) High resolution O 1s XPS spectra of bare CdO (left) and indium-doped CdO ($x = 0.075$, IV sample) nanoparticles. (c) SERS spectra of mercaptopyridine obtained using the various iterations of indium-doped CdO substrates depicted in panel a. Mercaptopyridine (1 mM) was first allowed to adsorb on the substrates, then the mixture was centrifuged, rinsed, and dried prior to analysis. The highest enhancements are observed at the lowest doping loadings (II, III, and IV spectra). Adapted with permission from Zhang *et al.*, *J. Phys. Chem. C*, 2021, **125**, 17125–17132. Copyright 2021 American Chemical Society.

Open Access Article. Published on 22 March 2023. Downloaded on 4/4/2023 3:23:28 PM.
This article is licensed under a Creative Commons Attribution-NonCommercial 3.0 Unported Licence.

generated in the pulsed laser ablation technique introduced crystal defects in the ZnO structure, as well as additional electrons in the conduction band. The collective oscillation of the resulting increased electron density gave rise to an LSPR in the NIR range, enabling overall SERS enhancements with standard probes crystal violet, rhodamine 6G, 4-aminothiophenol, and 4-mercaptobenzoic acid around the order of 10^6. These overall enhancements were also the result of charge transfer, as previously described for all semiconductor systems. The charge transfer in this case was attributed to the presence of defects (oxygen vacancies, defects in crystal geometries at the corners and edges, stacking faults, *etc.*) and identified to originate from electronic transfer from the HOMO of the analytes to the conduction band of the semiconductor, and from the valence band of the semiconductor to the LUMO of the analytes.

The same group utilized the described ZnO assemblies for differentiating cancer cells from non-cancerous cells *via* the SERS signatures of their DNA, RNA, protein, and lipid

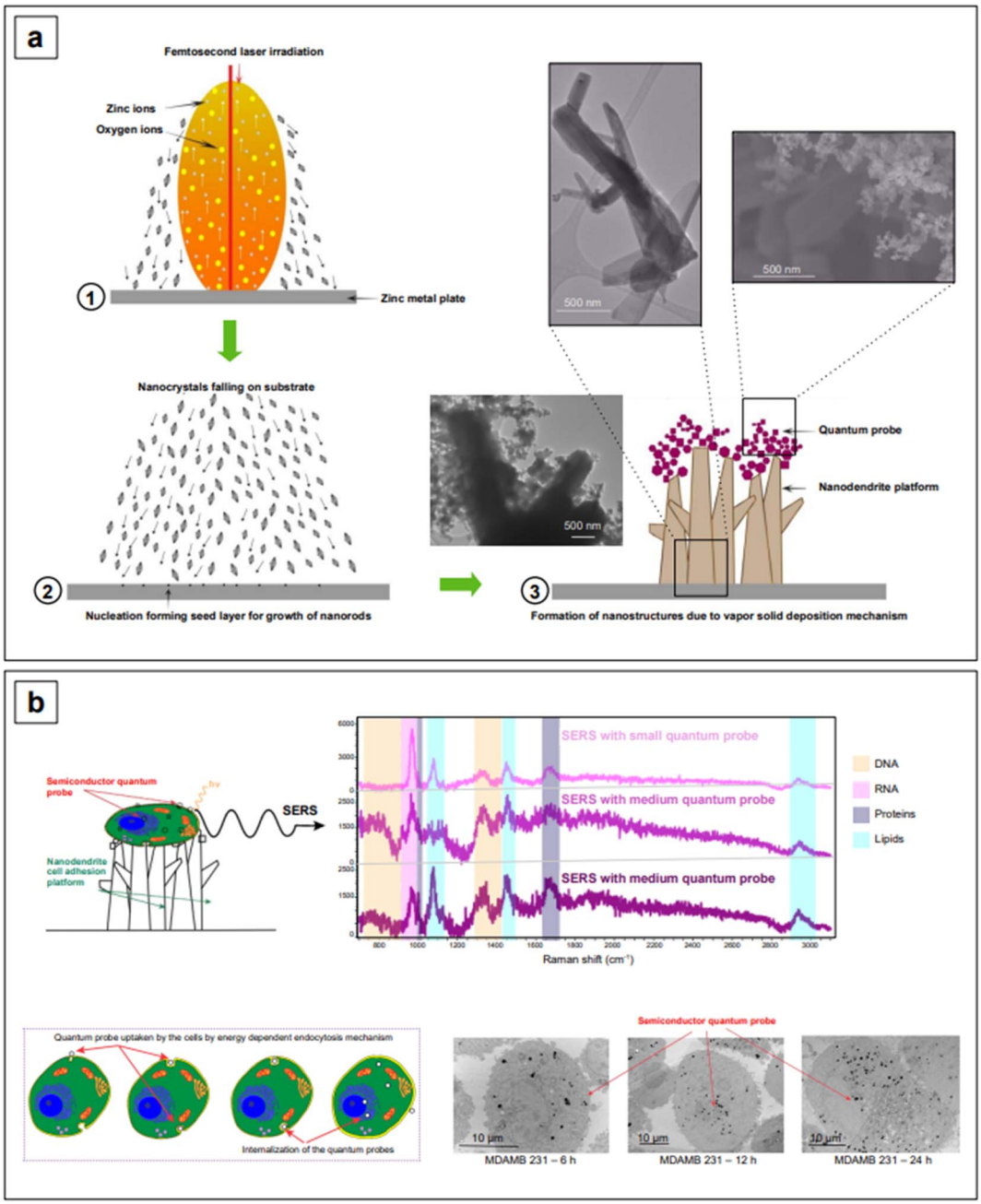

Fig. 8 (a) Fabrication and mechanism of formation of the ZnO nanodendrite-quantum probe assembly. (b) Single-cell detection by SERS. The nanodendrite platform has cell-adhering properties; the quantum probes are internalized by cells, increasingly with time, in an ATP-dependent process. The dimension of the quantum probe also plays a role in the extent of internalization. SERS spectra of adhered cells demonstrate multiplex and label-free detection of cell components: DNA (beige), RNA (pink), proteins (purple), and lipids (cyan). Adapted from Haldavnekar *et al.*, *Nat. Commun.*, 2018, **9**, 3065. Figures licensed under Creative Commons CC BY license, https://creativecommons.org/licenses/by/4.0/.

© 2023 The Author(s). Published by the Royal Society of Chemistry

Open Access Article. Published on 22 March 2023. Downloaded on 4/4/2023 3:23:28 PM. This article is licensed under a Creative Commons Attribution-NonCommercial 3.0 Unported Licence.

constituents. For example, based on the signal intensities of lipids *versus* proteins, they categorized cancer cells as having low lipid : protein ratio compared to healthy cells. The cellular uptake of nanoparticles was also investigated to characterize the limits of detection of the individual biomolecule classes inside the cells. They postulated that the signal intensity of lipids was the highest and the DNA/RNA was the lowest because a smaller number of nanostructures reaches the nucleus, and it took more time for the nanoparticles to reach the nucleus compared to the cytoplasm. This work provides strong evidence that the size and shape of nanoparticles decide the cellular uptake and thusly affect the signal intensity of individual biomolecules inside the cells. Further research into the development of nanostructures with a better cellular uptake can extend the limits of simultaneous detection of biomolecules inside cells and tissues.

Band gap engineering is not the only strategy that can be adopted to improve the SERS performance of semiconductors. Another common strategy is to fabricate composite materials. With *composite materials*, we here identify those substrates resulting from the coupling of two different materials in which only one of them is a semiconductor, such as gold on graphene. Contrary to what has been said about heterojunctions and doping, coupling of semiconductors to SERS-active non-semiconductors (*i.e.*, plasmonic metals) *as composites* does not yield any modification and tailoring of the band gap of the resulting composite material. However, the combined chemical enhancement of the semiconductor (*e.g.*, TiO_2, graphene oxide, …) with the intense LSPR of the plasmonic metal (*e.g.*, gold) gives rise to an improved system for SERS detection. An example of this approach is given by Lee and Kim,[176] who reported an easy procedure to obtain gold nanoparticles of about 7 nm in size, dispersed on a graphene oxide surface, using a photoreduction method to promote the formation of Au^0 (Fig. 9a). The obtained solution was subsequently drop-casted on a hydrophobic paper to fabricate a paper-based SERS sensor for the detection of fungicide thiram at the micromolar level, under 785 nm excitation.[176]

In a recent work, Liu *et al.*[177] fabricated a gold–graphene oxide composite, Au@GO, incorporated with Fe_3O_4 nanoparticles and poly(dopamine), and utilized it for the SERS detection of phenanthrene in standard solution (LOD 10^{-2} ng mL^{-1}). The magnetic character of Fe_3O_4 allows for the reuse of the SERS-active substrate, while the presence of poly(dopamine) prevents the aggregation of the gold nanoparticle component. When a suitably structured analyte is to be detected, such as phenanthrene, the peculiar π–π stacking of graphene or graphene oxide sheets favors π–π interactions with the adsorbed analyte. This promotes a maximization of the electromagnetic enhancement component in graphene-based plasmonic composites by shortening the distance between the analyte and the plasmon-sustaining surface.[152,178,179] π–π interactions are also leveraged in graphene-only substrates (*i.e.*, Graphene-Enhanced Raman Scattering, GERS[180]), optimizing the analyte-substrate contact and favoring signal enhancement *via* charge transfer mechanism. However, GERS is essentially confined to applications in the visible range, and for more information on this topic, the reader is referred to specialized literature.[181–184]

Yang *et al.*[185] reported a graphene–Au hybrid SERS nanoarray for the characterization of neuronal differentiation, where the Raman signal enhancement is obtained by combining the electromagnetic mechanism of the plasmonic Au cones nanoarray with the chemical mechanism of graphene oxide. The degree of subsequent reduction of the latter was tuned to ensure better interaction with the target molecule.[185] The array was obtained by laser-interference lithography (LIL) followed by gold deposition and graphene oxide functionalization *via* prior cysteamine linking. The homogeneous pattern created by LIL ensures a consistent enhancement without high point-to-point signal variations (Fig. 9b). The resulting graphene oxide/reduced graphene–Au nanoarray exhibits SERS activity in both the visible (λ_{exc} 514 and 633 nm) and NIR range (λ_{exc} 785 nm), although the highest local electric field responses were obtained when exciting at 633 nm, due to the specific morphological design of the plasmonic component of the nanoarray.[185] Further tuning in the NIR could be achieved by intervening on the morphological aspects of the nanoarray, as seen for colloidal nanoparticles in Section 2.1.1.

Another interesting example of NIR-SERS composite plasmonic-semiconductor substrates has been described by Yang *et al.*,[186] who have also incorporated up-conversion nanoparticles for use in both luminescence resonance energy transfer (LRET) and NIR-SERS experiments (λ_{exc} 980 nm). These substrates consisted of heterojunctions arising from the combination of Ag nanorices with $W_{18}O_{49}$ nanowire films coated with up-conversion nanoparticles ($NaYF_4$:Yb^{3+}, Tm^{3+}). The plasmons generated in the Ag/$W_{18}O_{49}$ nanowires not only contributed to the SERS signal but also improved the up-conversion photoluminescence efficiency of $NaYF_4$:Yb^{3+}, Tm^{3+} nanoparticles. Three-dimensional finite element simulations demonstrated that the maximum SERS enhancement is reached when the heterojunction interface is aligned in such a way that the tip of a silver nanorice is in vertical contact with the sides of a $W_{18}O_{49}$ nanowire. In the size optimization of the up-conversion component, it was found that 10 nm $NaYF_4$:Yb^{3+}, Tm^{3+} nanoparticles showed maximum LSPR response in the NIR, while a significant decrease was observed upon further increasing of the size.

The combination of plasmonic and other materials can also be achieved *via* the fabrication of core–shell structures. Plasmonic metals such as Au, Ag, and Cu are typically used as the core, while other materials, such as other transition metals, semiconductors, or SiO_2, are generally selected as the shell phase. This nanostructure architecture tunes the electronic structure and the optical properties of the final material by exploiting the phenomenon of *borrowing SERS activity*. When a target molecule is adsorbed on the shell surface of a plasmonic–nonplasmonic core–shell nanostructure, there is no direct contact with the plasmonic metal; however, the shell architecture allows the nonplasmonic material to *borrow* SERS activity from the plasmonic core, amplifying the Raman signal of the analyte by the electromagnetic mechanism. Because the SERS enhancement is strongly related to the distance between

Open Access Article. Published on 22 March 2023. Downloaded on 4/4/2023 3:23:28 PM.
This article is licensed under a Creative Commons Attribution-NonCommercial 3.0 Unported Licence.

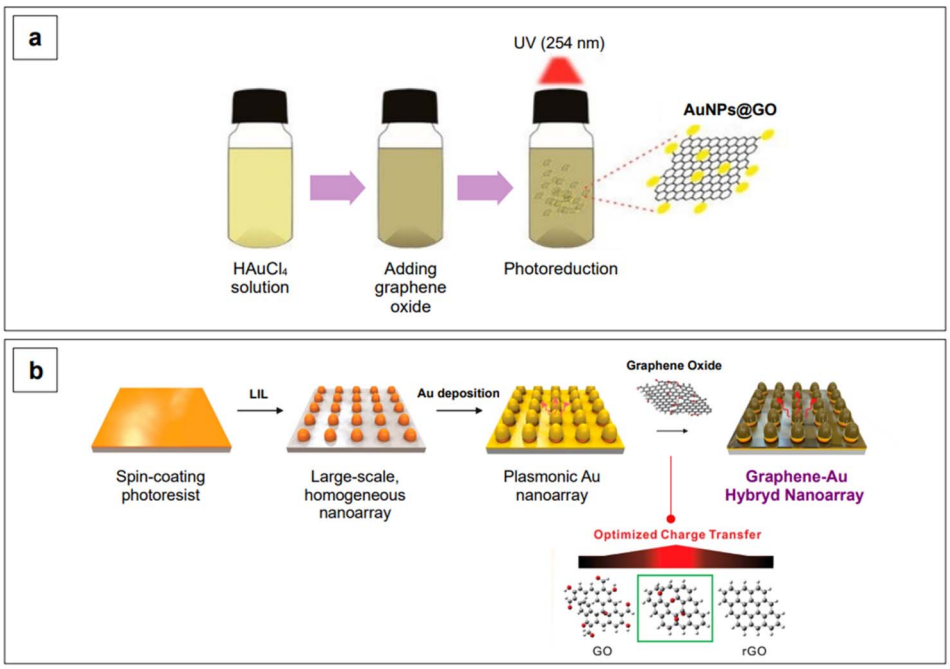

Fig. 9 Examples of synthetic strategies for gold–graphene oxide composite production. (a) Photoreduction method using UV light. Adapted from Lee, D.-J. and Kim, D. Y., *Sensors*, 2019, **19**, 5471. Figure licensed under Creative Commons CC BY license, https://creativecommons.org/licenses/by/4.0/. (b) Homogeneous plasmonic nanoarray generated by laser interference lithography (LIL) on a polymeric substrate, followed by gold coating by physical vapor deposition. An additional graphene oxide layer was established by electrostatic interactions after prior functionalization of gold with cysteamine. The degree of reduction of graphene oxide was tuned based on the maximization of the SERS performance of the substrate. Adapted with permission from Yang *et al.*, *Nano Lett.*, 2019, **19**, 8138–8148. Copyright 2019 American Chemical Society.

the analyte and the plasmon-sustaining material,[152] the non-plasmonic shell is required to be very thin. As previously described for traditional spherical nanoparticles (Fig. 2a), the position of the λ_{LSPR} of core–shell nanoparticles is influenced by the size of the plasmonic component; for example, the larger the core size, the higher the λ_{LSPR}. It is therefore apparent that large cores must be utilized to push the SERS activity of these nanostructures in the NIR. Unfortunately, ultrathin shells without defects (*pinhole-free shells*) are difficult to prepare, and thus, for applications in the NIR, the research has moved towards inverse architectures, in which the plasmonic metal is utilized to fabricate a thick shell, while another material (another transition metal, a semiconductor, SiO_2, …) is utilized as the core.

Interestingly, it is possible to create a complex core–shell structure using SiO_2 as the shell also on an anisotropic core, as reported by Atta *et al.*[187] In their work, they demonstrated that it is possible to obtain *both* anisotropic SiO_2 shells that follow the morphology of gold nanostars, *and* isotropically etched core-covering shells that leave the nanostar branches exposed, without altering their length or sharpness. The first type of core–shell structure is obtained during the initial phases of the silica shell growth, as this initially follows the anisotropic morphology of the nanostar. The second type of core–shell structure, on the other hand, is obtained after prior growth of a full, isotropic silica shell, with an optimized protocol that ensures the morphological preservation of the nanostar core. After the formation of a thick silica shell around the nanostars, a silica etching step is performed using a mild etching reagent, $NaBH_4$, instead of the more common and stronger reagent NaOH. This demonstrated to be the crucial step to chemo-selectively etch silica, leaving the branches of the gold nanostar exposed and unaltered.

Rare-earth semiconductors can also be utilized to form shells on plasmonic cores, the most common of which is CeO_2. Bao *et al.*[188] proposed a method that is easily adaptable to several combinations of metal@mesoporous oxide architectures, by simple variation of the pre-formed metal core or shell precursors. The same protocol also allows a facile modification of the shell thickness from 4 to 30 nm, by varying the Ce^{3+} added to the colloidal gold sol. The plasmonic behavior of the gold core (55 nm) was tuned to the NIR region owing to the confinement effect of the CeO_2 porous shell. The structure based on gold core and CeO_2 shell was tested to detect toluene vapor at concentrations of 10 ppm (λ_{exc} 785 nm), and the observed SERS enhancement is attributed to the high number of micropores in the shell, that can trap target molecules, bringing them closer to the plasmonic core where the SERS effect is higher.

Among novel structures, shell components can also be made with Metal–Organic Frameworks (MOFs).[189] MOFs are highly ordered porous materials synthesized by combining metal ions or clusters with an organic ligand, following the commonly adopted supramolecular approach. Due to their rational design

© 2023 The Author(s). Published by the Royal Society of Chemistry

Open Access Article. Published on 22 March 2023. Downloaded on 4/4/2023 3:23:28 PM. This article is licensed under a Creative Commons Attribution-NonCommercial 3.0 Unported Licence.

and functionalization, this class of materials is widely applied in multiple fields such as catalysis,[190] gas storage,[191] drug delivery,[192] and sensing,[193] including SERS. For instance, Zhang and co-workers[194] presented a one-pot synthesis for a series of SERS substrates composed of a Mg-based MOF, MOF-74, as the shell of varying thickness, and a gold core. While dimethylformamide (DMF) is the most commonly used solvent in MOF syntheses, these Au-MOF core–shell nanoparticles were synthesized in DMF–ethanol. The resulting nanoparticles were utilized for the detection of model analyte 4-nitrothiophenol by NIR-SERS (λ_{exc} 785 nm) with a LOD of 69 nM, as well as for the *in situ* monitoring of plasmon-assisted reactions. MOFs have also been utilized in composites, such as in the very recent work by Zhao *et al.*,[195] in which a Fe-MOF was utilized as a substrate to anchor gold nanorods, and implemented for the catalytic degradation and SERS detection of methylene blue, with a LOD of 9.3×10^{-12} M.[195]

Exploiting the concept seen for thicker plasmonic shell-nonplasmonic core nanoparticles, NIR-active substrates can also be fabricated by creating assemblies *via* plasmonic decorations on non-plasmonic large nanoparticles. In a very recent work, Bock *et al.*[196] prepared silica nanoparticles decorated with Au nanoparticles and demonstrated SERS activity and fit-to-purpose homogeneity for potential applications for *in vivo* imaging. In brief, after the separate synthesis of SiO_2 (~190 nm) and Au (~3 nm) nanoparticles, the latter were introduced into the SiO_2 sol to form SiO_2@Au seeds. The final product was then obtained by a seed-mediated method in which the Au growth was controlled by varying the concentration of the Au^{3+} precursor. By increasing the Au precursor concentration, the λ_{LSPR} also increases. This behavior was explained by the simultaneous presence of multiple factors: a higher number of Au nanoparticles, a narrow nanogap among the Au nanoparticles (1 nm for the highest Au precursor concentration), and thus, a stronger plasmonic coupling of the Au nanoparticles on the SiO_2 surface. The highest enhancements upon 785 nm illumination were therefore achieved at those Au concentrations that reduced the gap between adjacent Au nanoparticles on the surface of silica nanoparticles, generating hotspots. The Au-decorated silica nanoparticles were then labeled with more than ten Raman-active compounds and tested as potential SERS tags during *in vivo* NIR-SERS measurements.

Although the majority of alternative materials that we have listed so far are metal oxides, some alternative metals,[197–199] as well as transition metal nitrides (*e.g.*, TiN dimers and ZrN)[200] and chalcogenides (*e.g.*, CuTe nanocubes,[201] AuCu nanostars/MoS_2 [202]), also show potential for use as SERS-active plasmonic substrates in NIR applications. Transition metal nitrides TiN and ZrN, for example, exhibit high electron conductivity[200] compared to metal oxides, have optical properties in the NIR thats are comparable to gold,[200,203,204] and their electronic structure can be easily tailored *via* nitrogen vacancies engineering,[197] as previously illustrated for oxygen vacancies in metal oxides. Among the alternative metallic nanomaterials beyond gold and silver, magnesium nanoparticles have garnered interest in the last few years, demonstrating interesting optical properties, including near-field scattering that can be exploited in enhanced spectroscopies applications such as SERS.[205] Hopper *et al.*[199] elucidated and optimized the colloidal synthesis of Mg nanoparticles with varying size and broad LSPR in the visible and NIR ranges (Fig. 10a and b). The broad plasmonic response was attributed to the polydispersity of the sample, as well as to nanoparticle aggregation caused by the absence of stabilizing agents. However, numerical simulations by Discrete Dipole Approximation (DDA, Fig. 10c) show a correlation with the extinction spectra obtained by dark field scattering of individual nanoparticles (Fig. 10d), indicating promising avenues for less polydisperse versions of these materials. It must be recalled that magnesium, as any other non-noble metal, has high susceptibility for oxidation and chemical reactivity in general; this disadvantage, however, can be exploited to generate SERS-active composite nanomaterials, such as Au- and Ag-decorated Mg nanoparticles obtained by galvanic replacement.[206] A graphical summary of the alternative materials discussed in this section is reported in Fig. 11, along with a list of the diverse synthetic strategies that have been adopted for their fabrication.

2.1.3 NIR and SWIR reporters for infrared-active nanotags. The applications illustrated so far are all examples of direct, label-free detection. As mentioned in the introduction, *indirect* detection by SERS can also be implemented, that is, the production of a SERS signal from a *label molecule* upon recognition or capture of the actual target analyte. Because of the recognition element that is involved in the analyte capture, indirect detection is highly selective, and thus, it is most suited for complex, untreated samples such as those in biological matrices (*e.g.*, cell culture media, tissue). Moreover, it is ideal for analytes with molecular structure that is not conducive to direct adsorption and/or have a small SERS cross section. The recognition *and* enhancing substrate that is utilized to achieve indirect detection is called a *SERS nanotag*, which we here define as a functionalized plasmonic nanoparticle that comprises of a Raman reporter, a recognition element, and a biocompatible capping layer that confers stability to the whole system, in both fabrication and measurement environments. Although these systems can be referred to by other names in the literature, in the present review we will only be referring to them utilizing the terminology presented for their definition and highlighted in Fig. 12.

Because SERS nanotags are especially utilized in complex biological samples such as cell cultures and tissues, biocompatibility and stability in physiological conditions are of paramount importance. For these reasons, biocompatible capping systems, typically polymeric in nature such as bovine serum albumin (BSA) or varyingly functionalized polyethylene glycol (PEG: PEG-SH, NH_2-PEG-SH, *etc.*), are utilized to prevent opsonization.[209] The latter consists in the formation of a multi-layer protein corona around the nanoparticle, which causes passivation of the surface from analyte adsorption and, ultimately, irreversible colloid aggregation.[209,210] The growth of silica shells around plasmonic nanoparticles, which was described in the previous section of this review, can also be implemented as an alternative to the use of natural or synthetic polymers, as they not only offer a platform to tune the plasmonic response of the

Open Access Article. Published on 22 March 2023. Downloaded on 4/4/2023 3:23:28 PM.
This article is licensed under a Creative Commons Attribution-NonCommercial 3.0 Unported Licence.

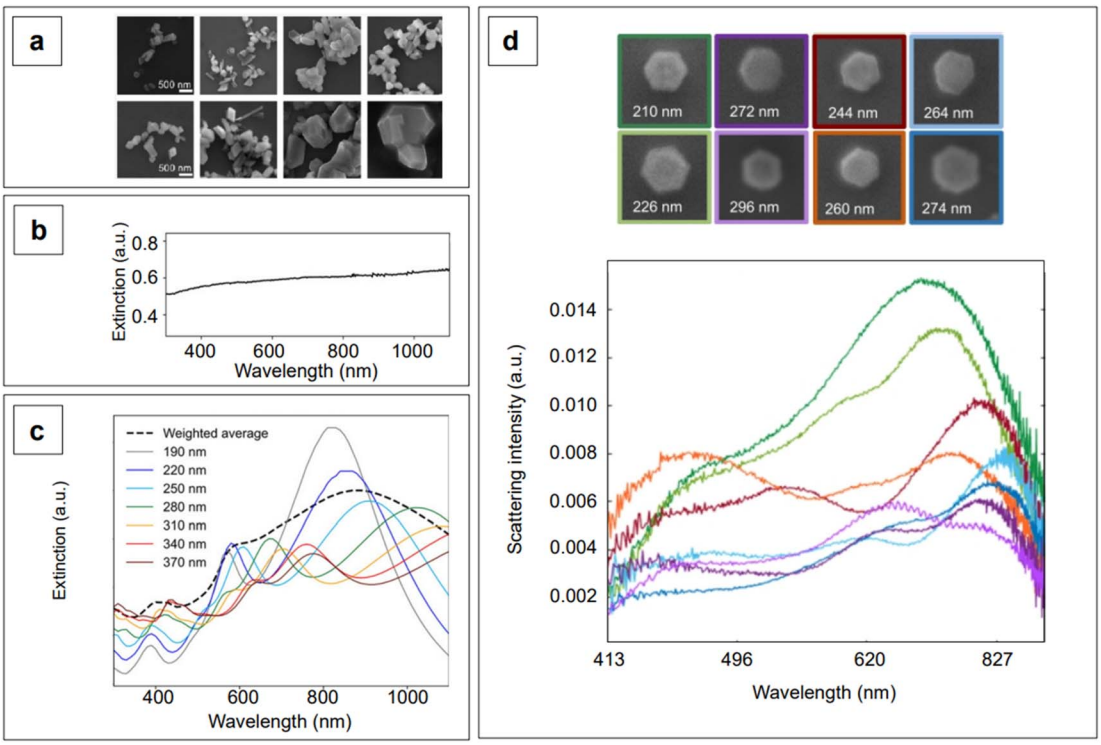

Fig. 10 (a) Magnesium nanoparticles as prepared by Hopper *et al.*,[199] obtained with overall increasing reactant concentrations (from left to right) and decreasing reaction temperature (top to bottom). (b) Experimental extinction spectrum of colloidal magnesium nanoparticles dispersed in isopropyl alcohol and having an average size of 300 ± 60 nm. (c) DDA-simulated extinction spectra of magnesium nanoparticles having varying size, hexagonal shape as found in real samples, and thickness ~0.1 times their tip-to-tip length. The weighted average obtained on the basis of the experimental size distribution is reposted as a black dashed profile. (d) Color-matched SEM micrographs (top) and scattering spectra (bottom) of Mg hexagonal platelets of varying tip-to-tip size. Adapted from Hopper *et al.*, *J. Phys. Chem. C*, 2022, **126**, 563–577; figures licensed under CC BY 4.0, https://creativecommons.org/licenses/by/4.0/.

nanoparticle system, but also achieve biocompatibility and stability in physiological media. Examples of this strategy can be seen in the works by Kircher's group,[90,211–214] who utilizes SERS nanotags for *in vivo* SERRS and SESORRS (see Section 2.2) imaging and thus, have stringent biocompatibility needs. An additional requirement that a nanotag capping system might have is the selectivity towards a particular biological target. For example, Dugandžić *et al.*[215] capped their silica-encapsulated nanotags with mannose for fast uptake by mature macrophages, which are known to express a mannose-specific C-type lectin receptor.

The recognition element can be a peptide,[214,216] an antibody,[90,115] or an aptamer,[213,217] and it is typically covalently bound to the nanoparticle *via* the Raman reporter, taking advantage of thiol chemistry or *via* the use of coupling agents such as heterobifunctional cross-linkers.[218,219] For example, Song *et al.*[216] utilized a commonly adopted bioconjugation strategy known as EDC-NHS chemistry[218–220] (1-ethyl-3-(3-dimethylaminopropyl)carbodiimide, *N*-hydroxysuccinimide) to anchor arginylglycylaspartic acid (RGD), a peptide recognition element for adenocarcinoma biomarker $\alpha_v\beta_3$ integrin, to gold nanostars. This strategy is utilized when the bioconjugation reaction involves an amine and a carboxylate; in this case, the amine comes from the RGD peptide, while the carboxylate comes from the Raman reporter 4-mercaptobenzoic acid (4-MBA). As shown in Scheme 1, EDC activates the carboxylate by forming a reactive *O*-acylisourea ester conjugate, making the charged form of NHS, SuO^-, able to yield an NHS-ester by transesterification.[219–221] The formed NHS-ester is an amine-reactive species that reacts with the primary amine in the arginine's residue of RGD, yielding the final reporter-recognition element adduct, RGD/4-MBA.[218–220] Such a bioconjugate was obtained after prior incubation of 4-MBA with gold nanostars, during which the Raman reporter chemisorbs to the gold substrate (Fig. 13a). Another example of bioconjugation reaction for the fabrication of SERS nanotags is illustrated by Bhamidipati *et al.*,[217] who utilized a thiolated aptamer as the recognition element for epithelial cell adhesion molecule (EpCAM), a protein that is utilized as a metastasis biomarker of different oncological diseases. The bioconjugation reaction was undergone step-wise, utilizing a heterobifunctional cross-linker, sulfo-succinimidyl 4-[*N*-maleimidomethyl] cyclohexane-1-carboxylate (sulfo-SMCC, Fig. 13b). 4-Aminothiophenol was pre-adsorbed onto gold nanostars *via* its sulfhydryl group, leaving its primary amine able to react with the NHS-ester terminus of sulfo-SMCC, yielding an amide bond.[218,222] The introduction of the thiolated aptamer at this point initiates a reaction with the maleimide terminus of sulfo-SMCC, producing a stable thioether bond between the aptamer and the linker/reporter system.[218,222] In those cases in which

© 2023 The Author(s). Published by the Royal Society of Chemistry

Open Access Article. Published on 22 March 2023. Downloaded on 4/4/2023 3:23:28 PM.
This article is licensed under a Creative Commons Attribution-NonCommercial 3.0 Unported Licence.

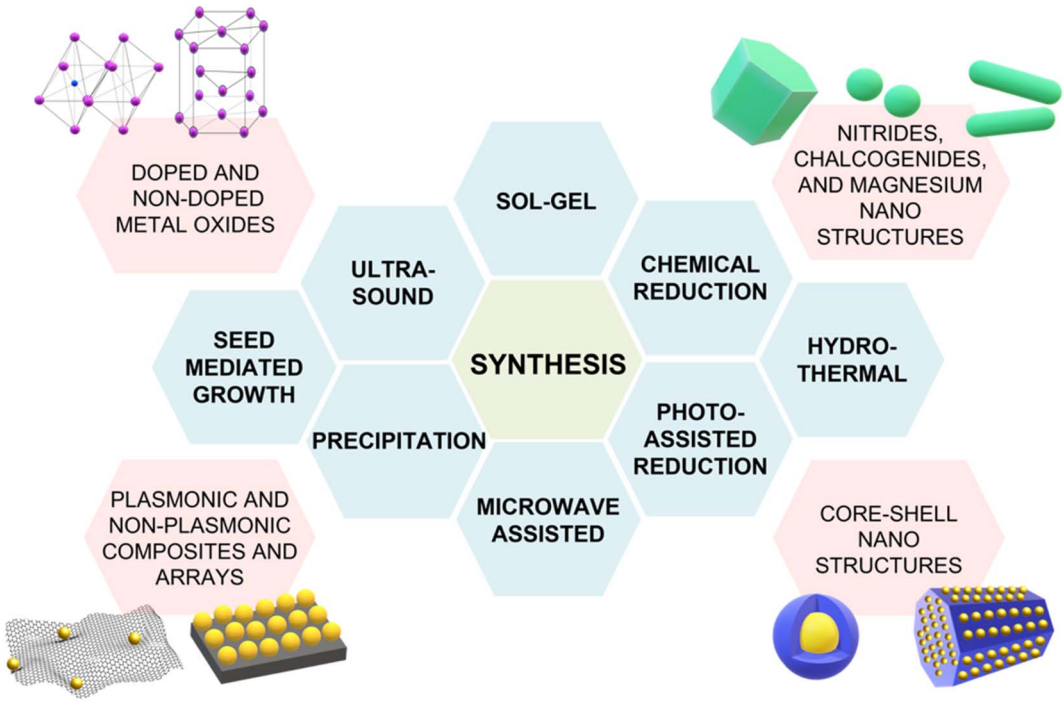

Fig. 11 Summary of the alternative NIR-active SERS substrates discussed in this section and their varying synthetic strategies: sol–gel,[172] chemical reduction,[199] hydrothermal synthesis,[173] photo-assisted reduction,[176] microwave-assisted synthesis,[207] precipitation,[188] seed-mediated growth,[196] ultrasound.[208]

a silica shell is chosen as the capping material, prior functionalization of silica is necessary to perform any subsequent bioconjugation reaction. For example, in a work by Kircher's group on the *ex vivo* and *in vivo* SERRS imaging of breast cancer lung metastases,[90] SERRS nanotags for transmembrane glycoprotein Tissue Factor (TF) were obtained by first growing a silica shell

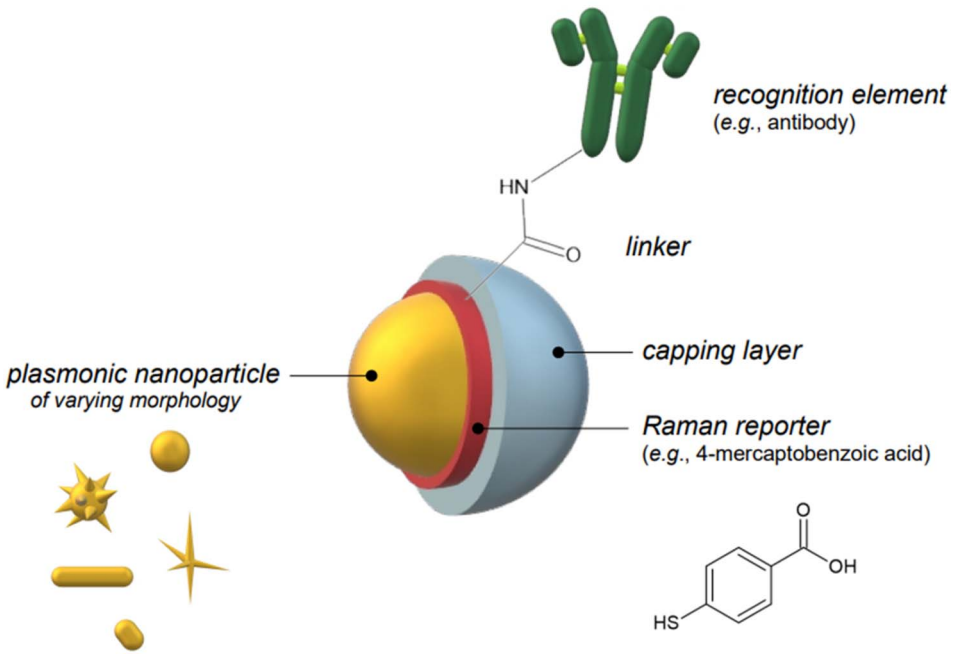

Fig. 12 Schematic representation of the components of a SERS nanotag: a plasmonic nanoparticle of varying morphology (yellow), an embedded or chemisorbed Raman reporter (red), a biocompatible capping layer (*e.g.*, silica, a polymer such as polyethylene glycol or bovine serum albumin, *etc.*; pale blue), and a recognition element such as an antibody (green), covalently conjugated to the Raman reporter *via* the use of a linker molecule. The SERS nanotag components are not in scale.

Open Access Article. Published on 22 March 2023. Downloaded on 4/4/2023 3:23:28 PM.
This article is licensed under a Creative Commons Attribution-NonCommercial 3.0 Unported Licence.

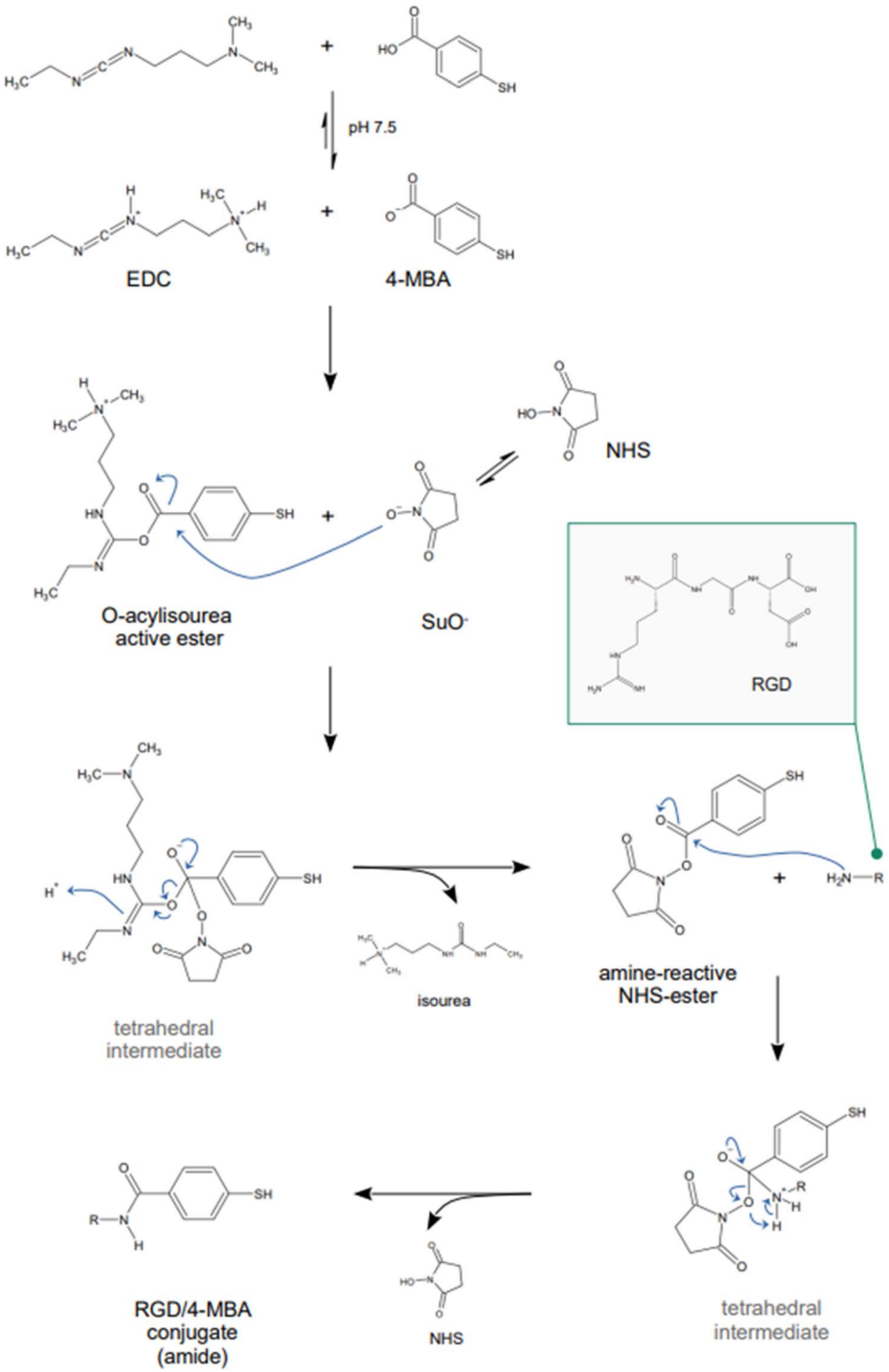

Scheme 1 EDC-NHS chemistry exemplified by the arginylglycylaspartic acid peptide/4-mercaptobenzoic acid (RGD/4-MBA) conjugate utilized in the fabrication of the SERS nanotags developed by Song *et al.*[216] Abbreviations: EDC, 1-ethyl-3-(3-dimethylaminopropyl)carbodiimide; NHS, *N*-hydroxysuccinimide; SuO-, anionic *N*-hydroxysuccinimide.

around gold nanostars in the presence of resonant Raman reporter IR780. Subsequently, the silica surface was functionalized with (3-mercaptopropyl)trimethoxy-silane (MPTMS), providing sulfhydryl groups for further grafting of the recognition element, an antibody targeted against glycoprotein TF. Anti-TF conjugation was then achieved by utilizing the heterobifunctional linker poly(ethylene glycol) (*N*-hydroxysuccinimide 5-pentanoate) ether *N*′-(3-maleimidopropionyl) amino ethane (NHS-PEG4k-Mal), which reacts in a similar way as illustrated for sulfo-SMCC (Fig. 13c).

 © 2023 The Author(s). Published by the Royal Society of Chemistry

Open Access Article. Published on 22 March 2023. Downloaded on 4/4/2023 3:23:28 PM.
This article is licensed under a Creative Commons Attribution-NonCommercial 3.0 Unported Licence.

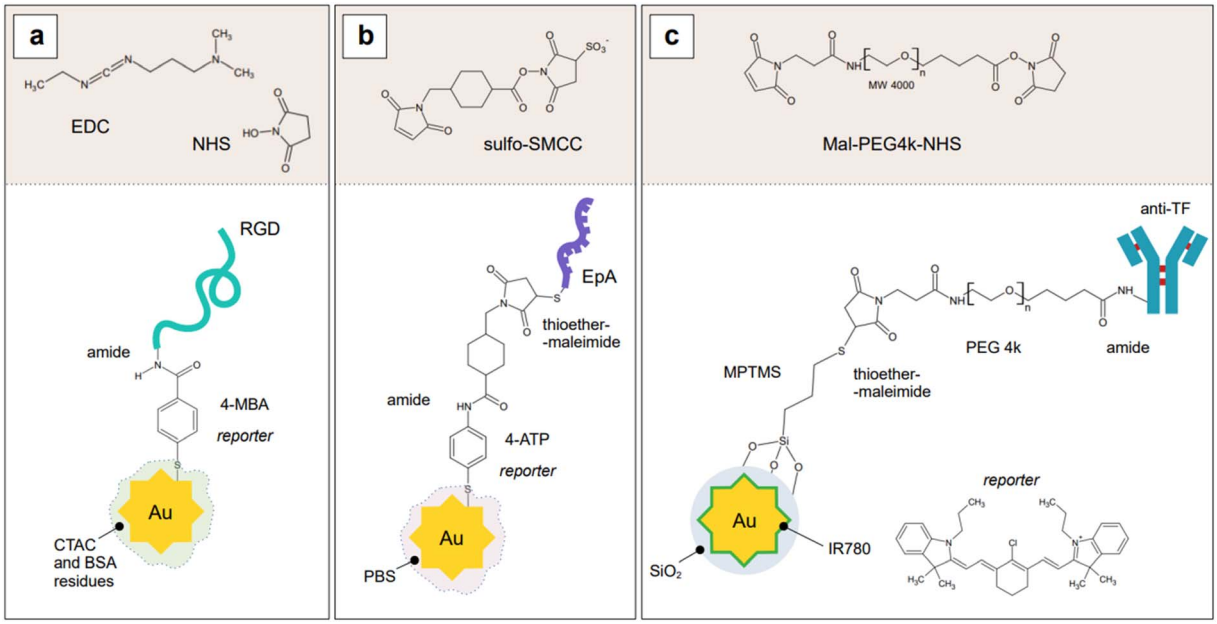

Fig. 13 Architecture of SERS nanotags and crosslinking chemistry. (a) Schematic representation of the SERS nanotags developed by Song *et al.*,[216] obtained utilizing EDC-NHS chemistry. Gold nanostars were incubated with 4-mercaptobenzoic acid (4-MBA) and conjugated *via* the formation of an amide bond to the arginylglycylaspartic acid peptide (RGD). The capping layer is likely constituted by remaining residues of cetyltrimethylammonium chloride (CTAC) and bovine serum albumin (BSA) originating from synthesis and SERS nanotag fabrication, respectively. (b) Schematic representation of the SERS nanotags developed by Bhamidipati *et al.*,[217] obtained utilizing sulfo-SMCC as the cross-linking agent. Surfactant-free gold nanostars were incubated with 4-aminothiophenol (4-ATP), which was then allowed to react with the NHS-ester terminus of the cross-linking agent. The maleimide terminus was subsequently allowed to react with the thiolated aptamer, EpA. The capping layer is likely formed by phosphate ions coming from the PBS buffer utilized to redisperse the SERS nanotags after fabrication and purification. (c) Schematic representation of the SERS nanotags developed by Nayak *et al.*,[90] obtained utilizing Mal-PEG4k-NHS as the cross-linking agent. Surfactant-free gold nanostars were encapsulated in silica shells, obtained in the presence of Raman reporter IR780, which remains embedded in the silica shell. The shell was then functionalized with mercaptopropyltrimethoxysilane, MPTMS, providing it with sulfhydryl groups to react with the maleimide group of the cross-linking agent. The antibody anti-TF was then conjugated *via* the NHS functionality of the cross-linking agent. Drawings are not in scale.

It must be noted that case-specific experimental parameters like pH, temperature, pre-treatments, incubation environment and time, all compound into an efficient functionalization of nanoparticles into SERS nanotags. For example, EDC chemistry is most efficient at a pH of 4.5, but it can be also successfully carried out at higher pH values, close to neutral, if required by the system (*e.g.*, use of PBS buffer).[218] As another example, reducing conditions (*e.g.*, incubation in tris(2-carboxyethyl) phosphine, TCEP[223]) are used as a pre-treatment to the adsorption of thiols, to cleave any disulfide bonds resulting from either self-reaction between probes or the presence of protecting capping groups. As for thiol-mediated functionalization reactions of gold substrates, temperature has proven to be a crucial parameter. Liu *et al.*[224] demonstrated that functionalization of gold nanoparticles at freezing conditions (−20 °C) leads to an increase in the loadings of thiolated oligonucleotides, compared to traditional room temperature and reagent-based (*i.e.*, salting out, low pH) procedures. This is the result of the formation of micropockets of segregated reactants during the freezing process. This segregation causes an increase in the local concentration of the thiolated reactants, thus increasing their rate of adsorption and, with it, their resulting packing density on the surface.[224] While this procedure was originally established for the fabrication of nanoflares,[224,225] it has been seamlessly transferred to analogous systems such as SERS nanotags.[226,227]

The systems described so far all make use of nanostars as the plasmonic component of the nanotag. This is because control of the hotspots formation *via* the use of intrinsic features such as nanostars branches is the preferred way of creating them in these analytical systems. Indeed, they allow for a reproducible, constant enhancement compared to the formation of hotspots by salt-induced aggregation, thus allowing fully quantitative studies. An alternative, although more complex, way of generating hotspots is the assembly of dimers or sandwich superstructures among SERS nanotags, such as in the case of the previously mentioned work by Bhamidipati *et al.*[217] The SERS nanotags described in Fig. 13b were utilized as the components of a planar array-based sandwich assay for the detection of EpCAM, both as a soluble protein in standard solution (binding buffer: 1× PBS, pH 7.4, 4.5 g L^{-1} glucose, 5 mM $MgCl_2$) and as a transmembrane protein in cell culture, under a 785 nm illumination. EpCAM-deficient HeLa cell lines were utilized as negative controls and thus, as substrates for assay selectivity studies. The planar array was prepared by first adhering surfactant-free gold nanostars onto a silanized and BSA-coated

Open Access Article. Published on 22 March 2023. Downloaded on 4/4/2023 3:23:28 PM.
This article is licensed under a Creative Commons Attribution-NonCommercial 3.0 Unported Licence.

glass substrate, and by subsequently functionalizing the nanostars with the same thiolated aptamer utilized in the fabrication of the SERS tags. To aid in the minimization of non-specific target binding, a 6-mercaptohexanol backfilling was established on the substrate-adhered nanostars by simple incubation. EpCAM protein was then incubated on such prepared substrates, after which washing and subsequent incubation with the SERS nanotags were performed. Captured EpCAM targets are in this way immobilized between the two plasmonic elements of the sandwich, thus benefiting from an increased enhancement given by the formation of hotspots between the SERS nanotags and the immobilized nanostars. This method allowed for a LOD of 10 pM for the soluble protein and 10 cells for the transmembrane protein when a truncated aptamer, EpA, was utilized as the recognition element.

When sandwich configurations are implemented such that transmission measurements are required, for example in solution, considerations on the λ_{max} of the plasmon band of the final dimer or aggregate must be taken into account. As seen in Section 2, the formation of dimers, trimers, and multiple aggregates shifts the plasmon band to higher wavelengths. This can be an advantage, in that it can be used to tune the enhancing substrate such that the LSPR can be excited by higher wavelength excitation sources than those that would excite its native, well-disperse colloidal form. However, the extent of this shift for measurements *in transmission* must never exceed the amount given by the difference between the native λ_{LSPR} and the wavelength of the excitation source. In other words, when working in transmission mode, pre-resonance conditions between the enhancing substrate and the laser source must be maintained for ideal LSPR excitation, and thus, ultimately, for best analytical performance. Readers interested in the physics behind this best practice point can refer to Sivapalan *et al.*[228] The practical effect of this can be observed in Tatar *et al.*,[115] where two versions of the same solution-based sandwich assay were implemented utilizing nanostars–nanostars and nanostars–nanosphere SERS tags dimers. The dimers were obtained by the bridging upon analyte capture of a 4-ATP/antibody SERS nanotag based on nanostars with "SERS amplifiers", PEG-SH/antibody-functionalized gold nanospheres or nanostars. The plasmon band of both dimer types falls past the utilized 785 nm excitation: this resulted in lower SERS signal than expected for a sandwich configuration. However, the nanostar–nanostar dimer system is able to compensate for this drawback because of the lightning rod effect given by the branched morphology. The nanostar–nanostar configuration of the assay was thus able to achieve an LOD in the range of 1 to 3 ng mL^{-1} for the detection of biomarker carcinoembryonic antigen-related cell adhesion molecule 5 (CEA-CAM5).

Because the Raman reporter is the actual element that produces the SERS signal, its quality must be such to guarantee low limits of detection and low fluorescence background. This can be achieved if the chosen reporter has the general characteristics of having a clean, defined spectrum, high photostability, and a large SERS cross section with low fluorescence quantum yield under the chosen illumination conditions. This implies that molecules that behave as effective Raman reporters under visible excitation might not behave equally well when illuminated in the NIR II, III, or SWIR. While common visible range Raman reporters such as 4-mercaptobenzoic acid,[57,216,229] 4-aminothiophenol,[115,217] methylene blue,[230] 1,2-bis(4-pyridyl) ethylene (BPE),[57] or rhodamine 6G,[230] can still be successfully utilized in the NIR I, such as under 785 and 1064 nm illuminations, moving towards higher wavelengths brings about the need of engineering this aspect, too, in analogy to what was illustrated for the nanoparticle morphology (Section 2.1.1). Moreover, exploitation of resonance effects to further increase the signal by working under NIR-SERRS conditions also requires engineering of the reporter molecule such that it possesses resonances under the given illumination.

Although this line of research has not seen many additions in the most recent years, groups such as Kircher's and Graham's and Faulds' produced notable work in the years between 2015 and 2017, deserving a mention here. Harmsen *et al.*[231] developed for the first time five 785 nm-resonant chalcogenpyrylium reporters for improved SERRS tags with attomolar sensitivity. These reporters were designed to exhibit low fluorescence due to increased intersystem crossing given by the presence of chalcogens, an absorption maximum that was tunable with chalcogen atom substitution (*i.e.*, S *vs.* Se), and high affinity for gold *via* the introduction of coplanar 2-thienyl groups that allow for direct adsorption. Synthesis is achieved by coupling reaction products **5** and **8** in Scheme 2a, after prior methylation and dehydration of known chalchogenpyranones **4** and **6** with methylmagnesium bromide, respectively, and condensation of **7** with *N*,*N*-dimethylthioformamide and hydrolysis of the resulting iminium salt intermediate.[231] SERRS nanotags prepared with thiopyrylium Reporter **3** produced the highest SERRS signal, and this was attributed to the better adsorption ability of 2-thienyl groups to the gold surface as compared to phenyl groups. This was hypothesized in the rational design of the reporters,[231] as 2-thyenyl groups are known to be more efficient at charge delocalization compared to phenyl substituents,[232] which could aid in π-metal interactions. Moreover, 2-thienyl groups are known for shifting the absorption maximum of a compound,[232] thus resulting in Reporter **3** having the most red-shifted λ_{max}. As a consequence, SERRS intensity could be ranked ($P < 0.05$) in terms of the number of 2-thyenyl groups, as follows: Reporters **1a**/**1b** (no 2-thienyl group) < Reporters **2a**/**2b** (two 2-thienyl groups) < Reporter **3** (four 2-thienyl groups).[231] Nanotags assembled with Reporter **3** showed attomolar sensitivity and were utilized for *in vivo* tumor margin delineation with an antibody targeting the epidermal growth factor receptor, EGFR.[231]

The synthesis presented by Harmsen *et al.*[231] was then expanded by Bedics *et al.*[233] to fabricate a library of 14 non-resonant chalcogenpyrylium reporters with activity in the NIR II (λ_{exc} 1280 nm) and picomolar sensitivity. In this work, the relationship between the SERS performance of the nanotag and the structural elements of the reporter, such as the number and type of chalcogen atoms and the number of methine groups, was further studied. In addition to the previously identified 2-thienyl groups,[231] it was found that 2-selenophenyl substituents also make optimal moieties for the adsorption of the reporters

© 2023 The Author(s). Published by the Royal Society of Chemistry

Open Access Article. Published on 22 March 2023. Downloaded on 4/4/2023 3:23:28 PM.
This article is licensed under a Creative Commons Attribution-NonCommercial 3.0 Unported Licence.

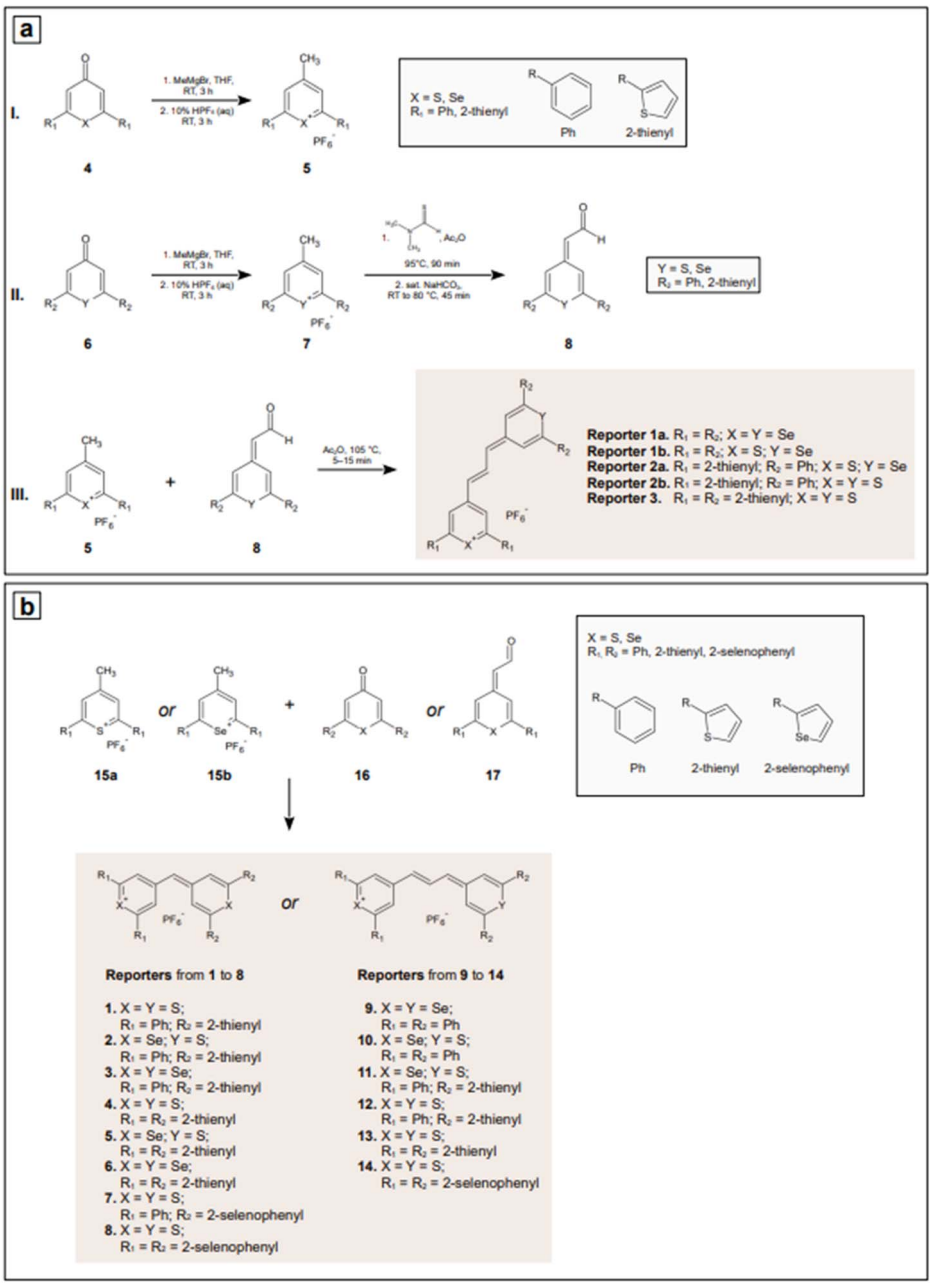

Scheme 2 (a) Reaction scheme for the synthesis of 785 nm-resonant chalcogenpyrylium reporters as prepared by Harmsen *et al.*[231] Abbreviations: THF, tetrahydrofuran; RT, room temperature; Ph, phenyl; Ac_2O, acetic anhydride; sat., saturated. (b) Precursors and final chalcogenpyrylium reporters active under 1280 nm excitation, as prepared by Bedics *et al.*[233]

onto gold nanoparticles.[233,234] In fact, when comparing the SERS signal obtained from Reporter **13** (four 2-thienyl substituents) with that obtained from Reporter **14** (four 2-selenophenyl substituents) after prior adsorption onto hollow gold nanospheres, a significant difference in intensity can be observed, where the 2-selenophenyl-substituted reporter shows the highest values. This is in line with prior reports that indicate a greater affinity for gold of selenolates than thiolates.[235,236] The library of reporters was in this case obtained by synthesizing starting materials 4-methylthiopyrylium or 4-methylselenopyrylium anions **15a** and **15b** and either chalcogenopyranone **16** or (4-chalcogeno-pyranylidene) acetaldehyde derivative **17**, which were then condensed in a similar manner as seen in Harmsen *et al.*,[231] to yield a series of monomethine (reporters from **1** to **8**) or polymethine (**9** to **14**) reporters (Scheme 2b).

Bedics *et al.*[233] observed that polymethine reporters exhibit higher SERS intensity under 1280 nm excitation compared to monomethine reporters, and attributed this behavior to the number of sp^2 carbons in the chalcogenpyrylium backbone. For this reason, Kearns *et al.*[237] prepared two chalcogenpyrylium pentamethine reporters having four 2-thienyl and four 2-

Open Access Article. Published on 22 March 2023. Downloaded on 4/4/2023 3:23:28 PM. This article is licensed under a Creative Commons Attribution-NonCommercial 3.0 Unported Licence.

selenophenyl substituents, respectively, and tested them after assembly as gold nanosphere-based SERS nanotags, verifying the trends highlighted by Bedics *et al.*[233]—2-selenophenyl substituents and longer polymethine bridges are the optimizing structural parameters for brighter, NIR-active chalcogenpyrylium SERS reporters.[233,237] The prepared pentamethine chalcogenpyrylium reporters have absorption maxima at 959 nm (2-selenophenyl-substituted thiopyrylium) and 986 nm (2-thienyl-substituted selenopyrylium), and allowed for limits of detection of 51 ± 5 pM and 63 ± 5 pM when utilized in 100 nm hollow gold nanosphere-based nanotags under non-resonant 1550 NIR III illumination. These LODs are one order of magnitude higher than those achievable under the same experimental conditions utilizing commercially available reporters in the SERS nanotag assembly, as BPE. Given the absorption maxima of these pentamethine compounds, they were subsequently successfully implemented as resonant reporters in the fabrication of femtomolar-sensitive SERS nanotags for 1064 nm illumination.[238]

The library of chalcogenpyrylium reporters obtained by Bedics *et al.*,[233] although very structurally similar to each other, shows non-overlapping SERS spectra. This is an intrinsic characteristic of Raman and SERS spectra, which combine the molecular fingerprint capability to narrow bands, thus making Raman reporters amenable to *multiplexing*. As opposed to the common *singleplex* strategy, multiplexing allows for the concomitant detection of multiple targets in a single measurement. Multiplexing is typically implemented by making use of different nanotags at the same time; heterogeneously functionalized (*i.e.*, mixed-ligand) nanotags can also be in principle implemented, but their fabrication poses challenges in terms of differential enrichment given by the different reporters, which may negatively impact sensitivity and quantitation. Although more control and knowledge about mixed-ligand nanoparticles fabrication processes are progressively achieved,[239] the use of a series of mono-reporter SERS nanotags in place of single, mixed-reporter SERS nanotags is the current preferred approach in SERS multiplexing.

An example of multiplexed detection using NIR-active SERS nanotags can be seen in the work by Zhang *et al.*,[230] who developed a lateral flow SERS immunoassay for the multiplexed detection, on a single test line, of three myocardial infarction biomarkers, creatine kinase-MB isoenzymes (CK-MB), cardiac troponin I (cTnI), and myoglobin (Myo) (Fig. 14). Three SERS nanotags active under 785 nm excitation and targeted each at one of the three biomarkers were prepared utilizing silver-core gold-shell nanoparticles as the plasmonic element, antibodies targeted at CK-MB, cTnI, and Myo as the recognition element, and methylene blue, Nile blue A, and rhodamine 6G as the Raman reporters. The latter were incorporated by direct adsorption to silver, and subsequently embedded in the gold shell of the resulting bimetallic nanosphere; optimal enhancement is therefore obtained by exploiting the core–shell interface as a hotspot. The tags were further functionalized with SH-PEG-COOH as the stabilizing coating, which was utilized for the bioconjugation reaction with the antibodies using EDC-NHS chemistry. Indirect, multiplexed detection of the cardiac biomarkers on the lateral flow assay strip was implemented using a sandwich configuration, obtained by immobilizing antibodies targeted at the biomarkers on the same test line, which hybridize with the SERS nanotag/biomarker complexes formed in the conjugation pad area of the strip (left panel, Fig. 14).

The immobilization of all three nanotag/biomarker complexes on the same test line constitutes an improvement of a previous lateral flow design from the same research group, which had three separate test lines (*i.e.*, sequential singleplex design), and thus, required longer times for the readout SERS signal to be acquired. The new design allowed for the total detection time to be reduced to one third, amounting to 17 minutes, while maintaining the limit of detection for each biomarker essentially unaltered, in the clinically relevant low to sub-pg mL^{-1} range. This is an example of how multiplexed detection can be especially of aid in time-sensitive applications, such as in the development of diagnostic tools for emergency room situations: myocardial infarction, as in this case, as well as potentially other acute cardiovascular diseases, or poisoning and overdosing events.

2.2 Collection set-up

In the introductory section we discussed how infrared radiation can penetrate tissues more in depth compared to visible light, reaching about 1 cm below the surface if a 785 nm source is used.[60] What if we need to illuminate a target that is located at a larger depth? As previously mentioned, the concept of Spatially Offset Raman Spectroscopy can be exploited in SERS or SERRS terms too, setting up SESORS or SESORRS experiments. These *deep Raman* techniques require an intervention on the design of the instrumentation, in that the collection probe has to be placed at an offset position compared to the laser source,[240] as depicted in Fig. 15a. The offset is necessary as it is the element that enables larger depth sampling; photons migrating laterally into a sample statistically tend to populate deeper volumes, because those that approach the air-sample interface tend to escape the sample instead, resulting undetected by an offset collection probe.[241,242] Readers interested in the basics of SORS as an introduction to SESORS can refer to a recent tutorial review by Mosca *et al.*[240]

The first account of SESO(R)RS was published by Stone *et al.* in 2010,[243] and demonstrated the applicability of surface-enhancement in a SORS context for the detection of lesions located 1.5 to 2.5 cm below the surface of a porcine tissue sample. The measurements were performed in transmission mode (Fig. 15b, VI) and were enabled by the injection of resonant (λ_{exc} 830 nm) SERS tags based on citrate-reduced silver nanospheres into the tissue sample. By the sole examination of this pioneering experiment, it is easy to notice the many factors that must be considered in a SESORS or SESORRS experiment: the delivery of SERS-active substrates inside the sample at the depth of interest, the SERS-substrate formulation, and thus, its biocompatibility and stability in biological media, as well as its concentration or number of administered nanoparticles per target cell (*i.e.*, *dose*). The latter was determined by Stone *et al.*[243]

© 2023 The Author(s). Published by the Royal Society of Chemistry

Open Access Article. Published on 22 March 2023. Downloaded on 4/4/2023 3:23:28 PM.
This article is licensed under a Creative Commons Attribution-NonCommercial 3.0 Unported Licence.

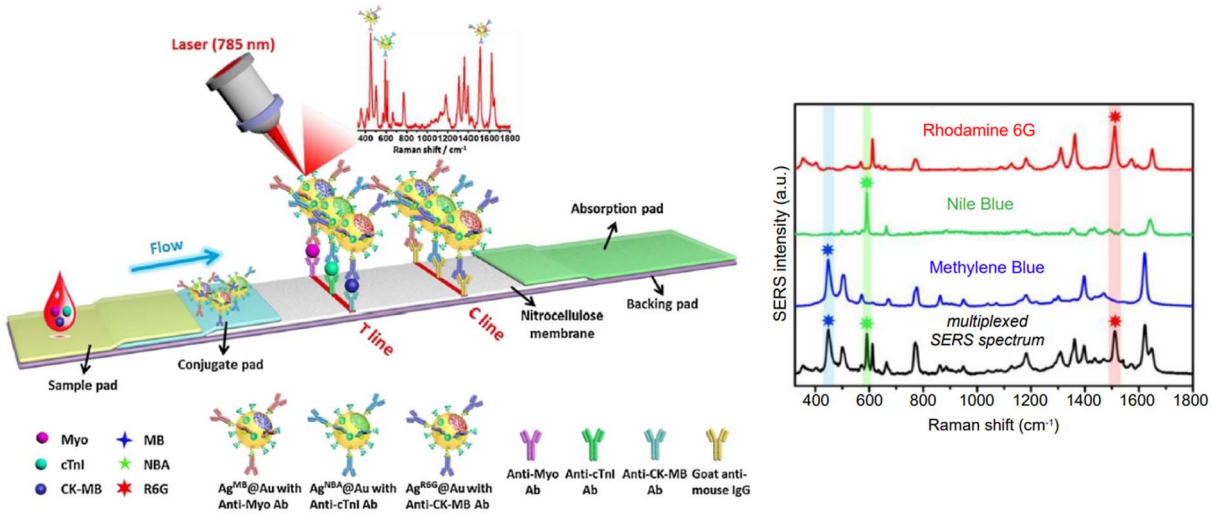

Fig. 14 Schematic representation of the multiplexed NIR-SERS single test line lateral flow assay developed by Zhang *et al.*[230] A mock-up or clinical blood sample is deposited on the sample pad. By capillary action, the analytes (Myo, myoglobin, purple sphere; cTnI, cardiac troponin I, cyan sphere; CK-MB, creatine kinase-MB isoenzymes, blue sphere) travel towards the conjugate pad, where they react with targeted SERS nanotags, pre-deposited on a single test line (T). A positive control line (C) is also implemented. The test line is imaged by SERS mapping, giving rise to a multiplexed SERS spectrum (red on the schematic, black on the right panel) when a positive sample is analyzed. The right panel illustrates the interplay between the three spectra of the nanotag reporters and the bands that are used for calibration and quantitation purposes. Drawings are not in scale. Reprinted with minor adaptations from Zhang *et al.*, *Sens. Actuators B Chem.*, 2018, **277**, 502–509, Copyright (2018), with permission from Elsevier.

by taking into account the thickness of the sample, the collection geometry (*i.e.*, transmission), the resulting sampled volume and number of cells in that volume, and the possible lesion size. For a 10 mm lesion, less resonant SERS tags per cell are necessary (estimated 3.5 SERS tags per cell), while the number increases to about 3500 per cell for a 1 mm lesion.[243] In another early work by Sharma *et al.*,[244] who demonstrated the feasibility of SESORS for the detection of species through bone and in

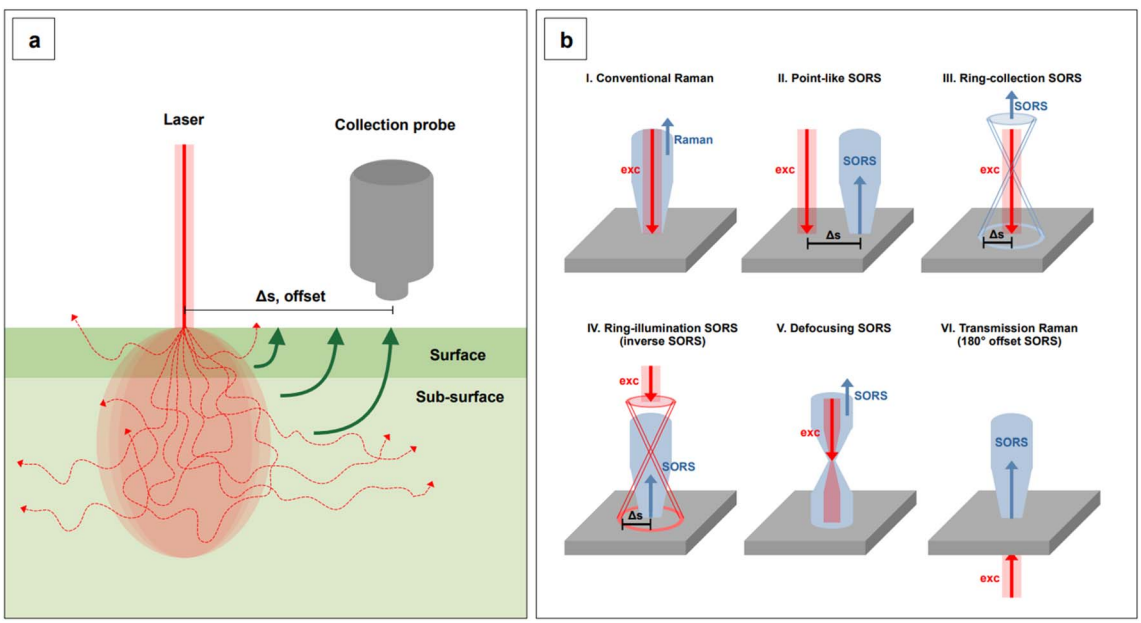

Fig. 15 (a) Schematic representation of the principles of Spatially Offset Raman Spectroscopy (SORS). Raman photons diffuse from the sample to the surface: photons originated from deeper layers tend to first spread sideways, thus allowing a selective detection of them when the collection probe is placed at an offset (Δs) from the illumination point. (b) Five possible source-collection probe configurations that allow for SORS and SESORS measurements, as compared to conventional Raman (I): (II) point-like configuration (backscattering); (III) ring-collection; (IV) ring-illumination; (V) defocusing; (VI) transmission configuration. Figures inspired by Mosca, S., *et al.*, 2021.[240]

© 2023 The Author(s). Published by the Royal Society of Chemistry

Open Access Article. Published on 22 March 2023. Downloaded on 4/4/2023 3:23:28 PM. This article is licensed under a Creative Commons Attribution-NonCommercial 3.0 Unported Licence.

backscattering geometry, the necessary dose of SERS tags to generate a SESORS signal was determined in absolute terms, and it was 2×10^{12} particles total. Because nanoparticles in tissue medium are not static, and they naturally tend to undergo diffusion along with other biophysical processes, the actual number of illuminated nanoparticles is plausibly less than the estimated, indicating that lower nanoparticle doses are likely possible.[244]

Despite nanoparticle dose is an essential element for the translation of SESO(R)RS to real life clinical applications, few focused studies have been carried out on the subject. It must also be noted that, necessarily, these studies are nanoparticle- or nanotag-specific, as well as wavelength-, geometry-, and offset-specific. For example, Nicolson *et al.*[245] have studied the dose of resonant and non-resonant tags for SESORS using a handheld instrument fitted with a 830 nm excitation line at its optimal[246] 8 mm offset and in backscattering geometry (Fig. 15b, II). To accurately control the concentration of the SERS tags and obtain limits of detection that were independent from diffusion into tissue, Nicolson *et al.*[245] performed their measurements in cuvettes, which were shielded by tissue samples of increasing thickness, up to 5 mm. This sampling depth is clinically relevant for through-skin breast cancer applications.[245,247]

In the same paper, Nicolson *et al.*[245] also demonstrated the benefits of utilizing resonant tags to achieve higher signal-to-noise ratio, and with it, the possibility of administering lower nanoparticle doses. The selected 830 nm-resonant chalcogenpyrylium[231] reporter, dye 823, was able to yield SESORRS signals that were eleven times higher than those obtained with the standard, commercially available non-resonant reporter, BPE. The same dye was also utilized to fabricate nanotags for the SESORRS detection of breast cancer 3D models based on multicellular tumor spheroids (MTS) through 15 mm porcine tissue,[248] as well as to perform multiplex imaging on analogous MTS models, in conjunction with other two 830 nm-resonant chalcogenpyrylium reporters.[249] Due to their brightness, resonant SERS tags also allow for larger sampling depths compared to non-resonant tags.[248,249] This is particularly important for measurements performed in backscattering geometry, which is known to access shallower depths compared to transmission measurements.[250,251]

The spatial component inherent to SESO(R)RS can be exploited to retrieve information about the depth of a target inclusion; this is particularly relevant for diagnostic or intra-operative applications, where the localization of a lesion could be required, either *in vivo* or *ex vivo*. Methods for this type of determination have been recently developed for both transmission and backscattering geometries by two independent groups. Mosca *et al.*[250] proposed an approach based on a totally non-invasive acquisition of calibration data, that is, without any need to obtain information from internal components of the sample. Consequently, this method can be utilized in transmission configuration. The reported root-mean-square error of prediction is 6.7%. Berry *et al.*,[251] on the other hand, developed a ratiometric approach to be utilized in backscattering geometry, based on the use of non-resonant nanotags and Principal Component Analysis (PCA). PCA was primarily utilized to determine the bands of the nanotags and tissue that contributed to the largest variance in the system. These were then utilized to calculate the natural logarithm of the nanotag to tissue intensity ratios at different known depths and build a linear model for each nanotag system. Two different non-resonant nanotags were studied to investigate the importance of the identity of the reporter, showing the slope of the intensity ratio as a function of inclusion depth exclusively depends on the optical properties of the tissue. In prediction studies, this method showed a root-mean-square error between 5.015 and 4.727%, depending on the utilized nanotag reporter.

Although SERS and SERRS nanotags populate the SESO(R)RS literature, less common, *direct* SESORS can also be implemented. Moody *et al.*[252] developed a direct SESORS method to detect neurotransmitters through bone (0.5–1.25 mm), both in mock brain samples and in a euthanized rat subject, under 785 nm irradiation. Mock samples were obtained by the superimposition of a rat skull onto agarose gel slabs that were previously incubated with standard solutions of neurotransmitters serotonin, melatonin, epinephrine, norepinephrine, and dopamine at physiologically relevant concentrations (low hundreds of nM (ref. 253)), both individually and in mixtures. To compensate for post-mortem decomposition processes, the brain of the euthanized rat subject was enriched with an injection of 200 μL of 100 μM serotonin, which was allowed to diffuse prior to analysis. Citrate-reduced gold nanospheres were chosen as the enhancing substrates, brought to pH 2 to invert the surface charge from negative to positive for neurotransmitter-substrate affinity reasons, and let incubate and diffuse into the gel slabs. The nanoparticle delivery into the skull of the euthanized rat subject was performed *via* through-skull injection instead. The measurements on mock samples demonstrated that it is possible to obtain direct SESORS spectra of neurotransmitters at concentrations that are relevant for human applications, with LODs that do not differ much from those calculated for the same species in standard solutions and synthetic biological fluids in regular SERS experiments.[252,253] While the thickness of the euthanized rat's skull allowed for through-bone SERS detection of serotonin even in the absence of an offset, maximum signal was obtained with a 1 mm offset in backscattering geometry, thus showing a potential of the SESORS technique to allow for the study neurotransmitters *in vivo*, in a minimally invasive way.[252]

For the detection of targets that are more complex than small molecules, and especially in those cases where imaging has to be performed, elaborate nanotags must be utilized. A paradigmatic example of this case is the first *in vivo* SESORRS study performed by Kircher's group.[214] Nanotags based on cyclic-RGDyK peptide-functionalized silica-encapsulated resonant-dye labeled gold nanostars were fabricated to target integrin, a protein that is overexpressed in glioblastoma multiforme (GBM) tumors. SESORRS imaging of GBM masses was performed *in vivo*, on glioblastoma-bearing mice under general anesthesia, after prior (18–24 hours) injection of a 100 μL 8 nM dose of nanotags *via* the tail vein (Fig. 16a). Measurements were collected both with and without offset, demonstrating the

 © 2023 The Author(s). Published by the Royal Society of Chemistry

Open Access Article. Published on 22 March 2023. Downloaded on 4/4/2023 3:23:28 PM.
This article is licensed under a Creative Commons Attribution-NonCommercial 3.0 Unported Licence.

higher accuracy of SESORRS over conventional, non-offset imaging collection set-ups (Fig. 16b), as well as comparable results to MRI (Fig. 16c).

It might be now apparent to the reader that because SESO(R)RS is a new technique, it is still being explored in its more fundamental aspects by relatively few groups. This notwithstanding, the two recent studies by Kircher's and Sharma's groups demonstrate a clear potential for clinical translation. To fully enable this process, in-depth studies on toxicity and biocompatibility of the enhancing substrates, as well as on nanoparticle administration, distribution, bioaccumulation, and kinetics of elimination must be undertaken. The interested reader can refer to recent reviews on these topics and learn about the state of the art in nanotoxicology.[254–257]

3 Perspective and conclusions

Throughout this review we have illustrated how the community has been addressing the challenges that arise when targeting or manipulating biological samples in sensing applications using NIR excitation sources. However, many more still remain open. Before concluding, we want therefore to give an overview of what we believe are the important problems to tackle moving forward. This list is based on our perspective, hence it is not exhaustive, but we hope it will provide the reader with some useful reflection points.

SERS measurements at any wavelength can certainly benefit from a homogeneous enhancing substrate, as this is directly responsible of the level of uniformity of the signal enhancement that can be produced. Substrate homogeneity is however *fundamental* in biological applications because of the intrinsic inhomogeneity and variability of the biological targets which, inherently, produce an intrinsically variable SERS response. Therefore, to ensure that the signal variation is due to the target and not to the substrate, one should aim to minimize substrate heterogeneity, especially when the analyte is present at low concentration. This heterogeneity is in general particularly prominent when colloidally synthesized nanoparticles are drop-casted or chemisorbed onto a substrate to form planar arrays. The heterogeneity arises not only from aggregation upon solvent evaporation (*e.g.*, coffee rings), but also from the often-limited morphological uniformity of the nanoparticles themselves, caused by a lack of understanding and control of the synthetic protocols. This is especially true in the case of one-pot syntheses with fast reaction kinetics. One-pot protocols inherently offer less reaction control because they lack separation between synthesis steps such as nucleation, seed formation, and growth—a level of control that can instead be achieved by adopting seed-mediated approaches. The latter, in contrast, lead to improved morphological modulation and hence to a better tuning of the plasmonic properties; a better control of the reaction kinetics in the fabrication of the enhancing substrates ultimately achieves a more homogeneous and reproducible SERS response.

The SERS response would also benefit from the identification of protocols that eliminate the need for surfactants in seed-mediated anisotropic growth. In fact, while being ideal for morphological manipulation, surfactants can be difficult to

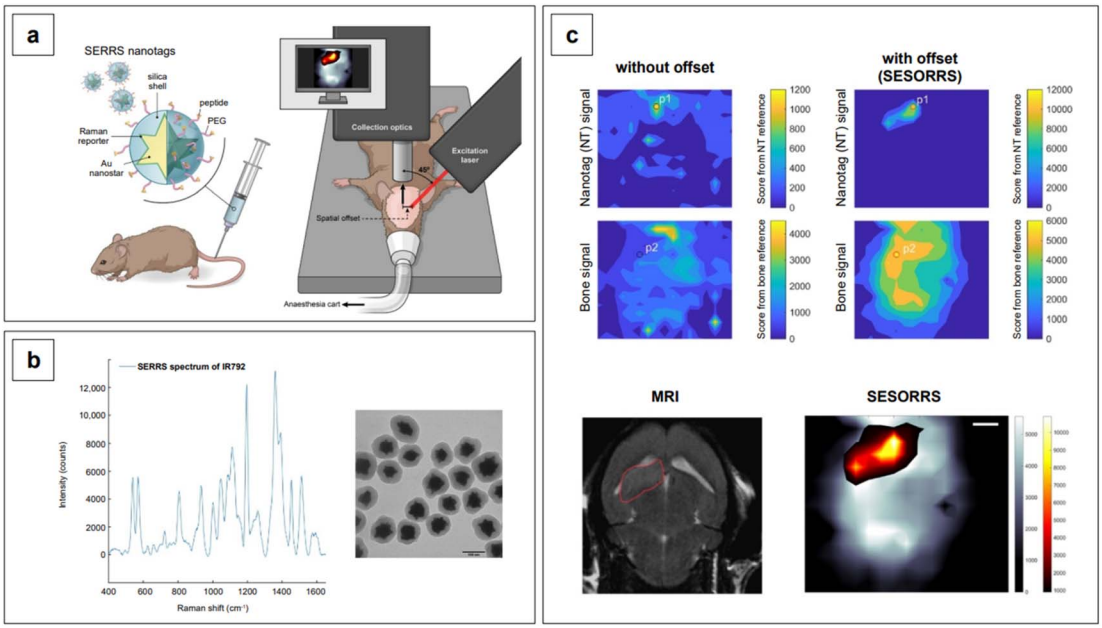

Fig. 16 (a) Schematic representation of the SERRS nanotag architecture and clinical setup for the *in vivo* SESORRS study. (b) Representative SERRS spectrum of the utilized Raman reporter, dye IR792, and TEM micrograph of the SERRS nanotags. (c) (top) Heatmaps of the nanotag and bone signals acquired without any offset (left) and with an offset of 2.5 mm (right). (bottom, left) 2D axial T2-weighted MRI with an horizontally inverted orientation shows the presence of a left frontal tumor, circled in red. (bottom, right) Comparatively analogous tumor margins are shown by the SESORRS heatmap, obtained by the merging of the individual bone and nanotag heatmaps. Adapted from Nicolson *et al.*, *Theranostics*, 2019, **9**, 5899–5913; figures licensed under CC BY 4.0, https://creativecommons.org/licenses/by/4.0/.

Open Access Article. Published on 22 March 2023. Downloaded on 4/4/2023 3:23:28 PM. This article is licensed under a Creative Commons Attribution-NonCommercial 3.0 Unported Licence.

remove and can thus hinder performance by increasing the separation between the nanoparticle surface and the target. Lastly, the properties of the nanoparticles would benefit from a more in-depth exploration of the role of stoichiometry, as recent literature highlighted its potentially pivoting role in morphological control. For example, in a surfactant-free, one pot synthesis of nanostars, different ratios of ascorbic acid to gold and silver were utilized to yield a series of nanostars with increased branch length (modulated *via* silver).[83] In the reaction coordinates that have been explored, one particular combination did not yield branched structures, but nanospheroids. This result has been later associated to the stoichiometry of the reaction:[53] when L-ascorbic acid is in excess, branched nanoparticles can be obtained, while, when it is the limiting agent, nanospheroids are synthesized instead. This could be due to the manipulation of nucleation *vs.* growth and deposition *vs.* diffusion rates *via* stoichiometry, and/or to the onset of surface-promoted disproportionation reactions upon excess of metal precursors, with a concomitant drift towards low-energy structures. Stoichiometry in the synthesis of nanoparticles is a factor that is seldom investigated or mentioned at all,[53,131,258] while it could be a tool in uncovering the rules that predict the shape of a nanoparticle, in the same way we can predict reaction products in organic syntheses.

The importance of morphological control cannot be discounted even when employing nanoparticles to build SERS tags. In this instance, ensuring (hypothetically) that the nanoparticles synthesized are always identical would lead to obtaining tags with identical SERS response, guaranteeing that, similar to what mentioned before, the measured SERS variability can only be associated to concentration changes in the target. Importantly however, considering that SERS tags are suspended in water or buffer and not anchored on a surface such as in the case of SERS arrays, nanoparticle reshaping can often occur, primarily due to defective or inadequate surface functionalization. One, for instance, should think about the fate of SERS tags in DNA extraction mixtures. In these solutions the presence of dithiotreitol (DTT) leads to the cleavage of the Au–S bond and the deprotection of the Au atoms on the nanoparticle's surface, which increases their mobility, finally leading to reshaping, consequent loss of SERS activity, and even colloidal destabilization and precipitation. Au ad-atom mobility, especially important at high energy locations on the nanoparticles, can be reduced by the presence of atomic Ag, which has been shown by Atta *et al.*[123] to deposit as a surface monolayer or bilayer on 6-branched gold nanostars. The presence of atomic Ag on the surface of the nanoparticle drastically reduces spike reshaping by limiting atomic mobility in surface Au, similar to what a well-bound surface ligand would do. Thus, both surface chemistry and surface functionalization of nanoparticles employed in SERS sensing, and especially as SERS tags, should be well understood and rationalized if we want to introduce them in the practical world.[53,123,259] This is particularly important in critical environments and bodily fluids, where, for instance, the presence of enzymes or the formation of a protein corona can drastically alter the properties of the nanoparticles as they had been designed or synthesized. Taken all together, these factors are key in determining the quality and repeatability of the SERS measurement, which are imperative to a successful translation of the technique to the clinical practice.

Thinking about clinical application leads us to consider the importance of collaborating with (bio)statisticians to bring power analysis, the inverse problem approach, and, in general, a rigorous (*vs.* black box) statistical treatment of data to the SERS community. While mandatory when dealing with clinical specimens, improving the way we handle SERS data, especially with the advent of instrumentation with ultrafast collection capability, would allow us to reap further benefits, such as an improved interpretation of full SERS spectra, as compared to the approach that only uses individual peak positions. This approach is fundamental in biological applications of *direct* SERS, where the spectra are complex and often not well characterized (*i.e.*, the signal is not generated by a known reporter but by the actual target, whose Raman fingerprint may not have been fully assigned yet). This improved analysis can provide richer information on the biological analyte and increase discrimination capability. All this, along with the richer information that we can extract by developing *ad hoc* statistical and deep learning tools, could improve the robustness and reliability of SERS and render it an important analytical and diagnostic tool in the biological and medical fields.

On the other side of the collaborative spectrum, one should remember the importance of establishing and sustaining collaborations with industry to push for the development of instruments with fast (and stable) acquisition rates. It must be recalled that adsorption is a dynamic process, and the association events between the components of a SERS sample (analyte, plasmonic metal, capping agents, synthetic by-products, *etc.*) are not static in nature, but represent instead instantaneous pictures of a dynamic equilibrium, *i.e.*, what might be happening on the surface of the nanomaterial during a given time interval. Molecules on a surface adsorb, desorb, diffuse,[260] and this dynamicity has a significant impact on the measurement of analytes, especially at ultratrace concentrations (<1 nM, *single molecule*), where it is often said that SERS spectra are observed as "blinking" events.[261] This intermittence in the observation of SERS spectra in the ultratrace regime is caused not only by the stochastic probability of a molecule adsorbing on a hotspot, the stochastic nature of nanoparticle-extrinsic (*i.e.*, aggregation-induced) hotspot formation, but also by the dynamic nature of the equilibria established during adsorption and the kinetics of the adsorption. The latter can be particularly problematic in that adsorption of certain analytes can occur at time scales that are faster than the sampling speed of the Raman instrument utilized for SERS measurements, effectively impeding single molecule detection.[262,263] This is especially true in the case of flow-through detection set-ups (*e.g.*, microfluidics, lab-on-a-chip, nanopore sequencing[264]), which are particularly relevant to clinical diagnostics applications. They are also important when analyzing large and complex bioanalytes, such as proteins, which, during interaction with the SERS substrate may be deformed by the highly curved surface and thus provide a fingerprint pattern that is not representative of the molecule in its functional state. Finally, it will be important to leverage

© 2023 The Author(s). Published by the Royal Society of Chemistry

Open Access Article. Published on 22 March 2023. Downloaded on 4/4/2023 3:23:28 PM. This article is licensed under a Creative Commons Attribution-NonCommercial 3.0 Unported Licence.

the collaboration with industry to develop equipment of low cost and high portability, which will be key to enable the use of the technique in laboratories where dangerous (or poorly portable) targets are studied, such as viruses.

Collaboration with industry brings up the necessity to make SERS substrates fabrication a more commercially appealing endeavor, which translates into achieving high yield, scaled-up synthetic processes. Unfortunately, nanomaterial fabrication is extremely sensitive to mass transfer parameters, and scale-up approaches *via* simple proportional increase of reagents and batch vessels volumes (*i.e.*, *scale-out* approach) are unfeasible, because they do not preserve these parameters.[265] Micromixer-based flow reactor processes, on the other hand, allow for the preservation of the mass transfer characteristics of an original batch process by increasing the number of *parallel* reactors as opposed to their individual volume (*i.e.*, *numbering-up* approach).[265] However, the lack of fundamental knowledge of the complex relationships between all mass transfer parameters, especially for anisotropic growth syntheses, still constitutes an obstacle in the straightforward application of these scale-up approaches, and thus, in the large-scale fabrication of SERS substrates. As mentioned for other aspects of SERS research, computational simulations of the hydrodynamic flows,[266] as well as the application of industrial processes-specific machine learning algorithms[265,267–269] can aid in the advancement of this field, minimizing the bottleneck that currently halts the commercial potential of these materials, and thus, the establishment of SERS as a routine analytical platform.

In consideration of our focus on applications in the infrared, it will be fundamental to exploit the increasing accessibility and cost-effectiveness of SWIR detectors (*e.g.*, extended InGaAs detectors),[34] that can overcome the instrumental issues that have so far drastically limited SERS analysis beyond 1000 nm. In turn, technological progress in this area could also benefit the telecommunications industry when coupled with the development of highly anisotropic plasmonic materials with resonances in the SWIR.[270,271] Along with the design of SWIR-resonant plasmonic materials, we must not forget the development of new resonant and non-resonant SERS reporters for NIR and SWIR applications, which has seen a stall in the recent years. However, developments in the design of NIR fluorophores, which are typically also Raman active, can be leveraged to extract useful tips for future revival of this branch of research. Research on fluorophores is more active, although the synthesis of red-shifted dyes remains challenging. Theoretical information for rational design of these molecules can be compiled and leveraged as it concerns the reduction of the fluorescence quantum yield (QY), as it would reduce the fluorescence background that is known to affect the SERS response. In a recent review on NIR-II fluorescent dyes by Li *et al.*,[60] the following points were listed as key guidelines in the design of these types of reporters: (1) increasing the conjugation chain length, and varying the heteroatom from oxygen to other chalcogens, results in redshifted spectra (as seen in the works of Harmsen,[231] Bedics,[233] and Kearns[238]); (2) a rigid aromatic structure bearing halogen atoms like Cl/Br/I is unfavorable to the fluorescence process and can decrease the QY *via* increased intersystem crossing caused by the heavy atom effect; (3) functional groups like carboxyl, cyano, and carbonyl can lower the HOMO and increase the energy gap between HOMO and LUMO, hence leading to a certain loss of QY. Taking into account all these guidelines would enable the synthesis of NIR-II fluorophores that can be applied also as Raman reporters, similar to what is commonly done with rhodamine 6G, crystal violet, and others.

Finally, and most importantly from the materials design standpoint, going forward it will be necessary to leverage the use of doped metal oxide nanoparticles (such as ZnO) as infrared SERS substrates. Fundamental studies on these materials, focusing on composition, morphology, electronic energy levels, and their electromagnetic and chemical enhancement mechanisms will be needed to fill the gaps that are still significant in their application for the detection of bioanalytes, such as disease biomarkers. While some of the research that has already been carried out to study the SERS properties of plasmonic materials active in the visible will have to be repeated for infrared-active materials, much of the knowledge we have put together over the past 25 years will result tremendously useful: it will guide us in this understanding and discovery process that is now in its infancy, but promises to bring significant scientific and technological breakthroughs in the years to come.

Conflicts of interest

There are no conflicts to declare.

Acknowledgements

This project has received funding from the European Research Council (ERC) under the European Union's Horizon 2020 Research and Innovation Programme (grant agreement No. 865819).

References

1 C. J. Murphy, T. K. Sau, A. M. Gole, C. J. Orendorff, J. Gao, L. Gou, S. E. Hunyadi and T. Li, *J. Phys. Chem. B*, 2005, **109**, 13857–13870.
2 N. R. Jana, L. Gearheart and C. J. Murphy, *Langmuir*, 2001, **17**, 6782–6786.
3 S. J. Hurst, E. K. Payne, L. Qin and C. A. Mirkin, *Angew. Chem., Int. Ed.*, 2006, **45**, 2672–2692.
4 C. G. Khoury and T. Vo-Dinh, *J. Phys. Chem. C*, 2008, **112**, 18849–18859.
5 S. Barbosa, A. Agrawal, L. Rodríguez-Lorenzo, I. Pastoriza-Santos, R. A. Alvarez-Puebla, A. Kornowski, H. Weller and L. M. Liz-Marzán, *Langmuir*, 2010, **26**, 14943–14950.
6 L. Gunnarsson, E. J. Bjerneld, H. Xu, S. Petronis, B. Kasemo and M. Käll, *Appl. Phys. Lett.*, 2001, **78**, 802–804.
7 N. Félidj, S. L. Truong, J. Aubard, G. Lévi, J. R. Krenn, A. Hohenau, A. Leitner and F. R. Aussenegg, *J. Chem. Phys.*, 2004, **120**, 7141–7146.

Open Access Article. Published on 22 March 2023. Downloaded on 4/4/2023 3:23:28 PM. This article is licensed under a Creative Commons Attribution-NonCommercial 3.0 Unported Licence.

8 L. A. Dick, A. D. McFarland, C. L. Haynes and R. P. van Duyne, *J. Phys. Chem. B*, 2002, **106**, 853–860.
9 L. Wang, L. Xu, H. Kuang, C. Xu and N. A. Kotov, *Acc. Chem. Res.*, 2012, **45**, 1916–1926.
10 J. P. Camden, J. A. Dieringer, J. Zhao and R. P. van Duyne, *Acc. Chem. Res.*, 2008, **41**, 1653–1661.
11 S. A. Maier and H. A. Atwater, *J. Appl. Phys.*, 2005, **98**, 011101.
12 W. A. Murray and W. L. Barnes, *Adv. Mater.*, 2007, **19**, 3771–3782.
13 M. M. Miller and A. A. Lazarides, *J. Phys. Chem. B*, 2005, **109**, 21556–21565.
14 C. L. Haynes, A. J. Haes, A. D. McFarland and R. P. Van Duyne, in *Topics in fluorescence spectroscopy*, ed. C. D. Gedde and J. R. Lakowicz, Springer Science + Business Media Inc, New York, 2005, pp. 47–99.
15 K.-S. Lee and M. A. El-Sayed, *J. Phys. Chem. B*, 2006, **110**, 19220–19225.
16 J. E. Millstone, S. J. Hurst, G. S. Métraux, J. I. Cutler and C. A. Mirkin, *Small*, 2009, **5**, 646–664.
17 International Human Genome Sequencing Consortium, *Nature*, 2004, **431**, 931–945.
18 J. Grisham, *Nat. Biotechnol.*, 2000, **18**, 365.
19 T. Shin, D. Kraemer, J. Pryor, L. Liu, J. Rugila, L. Howe, S. Buck, K. Murphy, L. Lyons and M. Westhusin, *Nature*, 2002, **415**, 859.
20 C. Galli, I. Lagutina, G. Crotti, S. Colleoni, P. Turini, N. Ponderato, R. Duchi and G. Lazzari, *Nature*, 2003, **424**, 635.
21 Q. Zhou, J.-P. Renard, G. le Friec, V. Brochard, N. Beaujean, Y. Cherifi, A. Fraichard and J. Cozzi, *Science*, 2003, **302**, 1179.
22 L. Mancinelli, M. Cronin and W. Sadée, *AAPS PharmSci*, 2000, **2**, 29–41.
23 J. de Leon, *Expert Rev. Mol. Diagn.*, 2006, **6**, 277–286.
24 K. Jain, *Expert Rev. Mol. Diagn.*, 2002, **2**, 299–301.
25 R. Sachidanandam, D. Weissman, S. C. Schmidt, J. M. Kakol, L. D. Stein, G. Marth, S. Sherry, J. C. Mullikin, B. J. Mortimore, D. L. Willey, S. E. Hunt, C. G. Cole, P. C. Coggill, C. M. Rice, Z. Ning, J. Rogers, D. R. Bentley, P.-Y. Kwok, E. R. Mardis, R. T. Yeh, B. Schultz, L. Cook, R. Davenport, M. Dante, L. Fulton, L. Hillier, R. H. Waterston, J. D. McPherson, B. Gilman, S. Schaffner, W. J. van Etten, D. Reich, J. Higgins, M. J. Daly, B. Blumenstiel, J. Baldwin, N. Stange-Thomann, M. C. Zody, L. Linton, E. S. Lander and D. Altshuler, *Nature*, 2001, **409**, 928–933.
26 F. S. Collins and V. A. McKusick, *JAMA*, 2001, **285**, 540.
27 K. K. Jain, *Technol. Cancer Res. Treat.*, 2005, **4**, 645–650.
28 R. Weissleder, *Nat. Biotechnol.*, 2001, **19**, 316–317.
29 T. Hirschfeld and B. Chase, *Appl. Spectrosc.*, 1986, **40**, 133–137.
30 H. J. Butler, L. Ashton, B. Bird, G. Cinque, K. Curtis, J. Dorney, K. Esmonde-White, N. J. Fullwood, B. Gardner, P. L. Martin-Hirsch, M. J. Walsh, M. R. McAinsh, N. Stone and F. L. Martin, *Nat. Protoc.*, 2016, **11**, 664–687.
31 E. C. LeRu and P. Etchegoin, *Principles of Surface-Enhanced Raman Spectroscopy*, Elsevier, Amsterdam, 2009.
32 E. C. le Ru, P. G. Etchegoin, J. Grand, N. Félidj, J. Aubard and G. Lévi, *J. Phys. Chem. C*, 2007, **111**, 16076–16079.
33 F. Shan, X. Y. Zhang, X. C. Fu, L. J. Zhang, D. Su, S. J. Wang, J. Y. Wu and T. Zhang, *Sci. Rep.*, 2017, **7**, 6813.
34 X. Chen, Y. Gu and Y. Zhang, in *Epitaxy*, ed. M. Zhong, InTech Open, London, 2018, pp. 203–234.
35 Q. L. Kleipool, R. T. Jongma, A. M. S. Gloudemans, H. Schrijver, G. F. Lichtenberg, R. M. van Hees, A. N. Maurellis and R. W. M. Hoogeveen, *Infrared Phys. Technol.*, 2007, **50**, 30–37.
36 B. Smiri, M. ben Arbia, D. Ilkay, F. Saidi, Z. Othmen, B. Dkhil, A. Ismail, E. Sezai, F. Hassen and H. Maaref, *Mater. Sci. Eng., B*, 2020, **262**, 114769.
37 X. Ji, B. Liu, H. Tang, X. Yang, X. Li, H. Gong, B. Shen, P. Han and F. Yan, *AIP Adv.*, 2014, **4**, 087135.
38 G. Hong, A. L. Antaris and H. Dai, *Nat. Biomed. Eng.*, 2017, **1**, 0010.
39 A. M. Smith, M. C. Mancini and S. Nie, *Nat. Nanotechnol.*, 2009, **4**, 710–711.
40 Horiba, *Synapse InGaAs/Symphony II InGaAs Deep Cooled NIR Scientific Cameras*, **https://www.horiba.com/int/products/detail/action/show/Product/synapse-ingaassymphony-ii-ingaas-1483/**, accessed 10 June 2022.
41 K. M. Kosuda, J. M. Bingham, K. L. Wustholz and R. P. van Duyne, in *Comprehensive Nanoscience and Technology*, ed. D. L. Andrews, G. D. Scholes and G. P. Wiederrecht, Elsevier, Amsterdam, 2001, pp. 263–301.
42 L. Litti and M. Meneghetti, *Phys. Chem. Chem. Phys.*, 2019, **21**, 15515–15522.
43 C. Deriu, I. Conticello, A. M. Mebel and B. McCord, *Anal. Chem.*, 2019, **91**, 4780–4789.
44 E. Akanny, A. Bonhommé, C. Commun, A. Doleans-Jordheim, F. Bessueille, S. Bourgeois and C. Bordes, *Anal. Bioanal. Chem.*, 2019, **411**, 5563–5576.
45 H. T. Phan, T. S. Heiderscheit and A. J. Haes, *J. Phys. Chem. C*, 2020, **124**, 14287–14296.
46 D. Yılmaz and M. Culha, *Langmuir*, 2022, **38**, 6281–6294.
47 R. Pilot and M. Massari, *Chem. Phys.*, 2021, **2**, 100014.
48 P. C. Lee and D. Meisel, *J. Phys. Chem.*, 1982, **86**, 3391–3395.
49 J. Turkevich, P. C. Stevenson and J. Hillier, *Discuss. Faraday Soc.*, 1951, **11**, 55.
50 G. Frens, *Nature*, 1973, **241**, 20–22.
51 C. J. Murphy and J. M. Buriak, *Chem. Mater.*, 2015, **27**, 4911–4913.
52 R. A. Alvarez-Puebla and L. M. Liz-Marzán, *Chem. Soc. Rev.*, 2012, **41**, 43–51.
53 C. Deriu, A. Bracho and B. McCord, *J. Phys. Chem. C*, 2022, **126**, 2023–2040.
54 S. S. Masango, R. A. Hackler, N. Large, A.-I. Henry, M. O. McAnally, G. C. Schatz, P. C. Stair and R. P. van Duyne, *Nano Lett.*, 2016, **16**, 4251–4259.
55 M. Moskovits, *J. Raman Spectrosc.*, 2005, **36**, 485–496.
56 M. Moskovits, *Phys. Chem. Chem. Phys.*, 2013, **15**, 5301–5311.

© 2023 The Author(s). Published by the Royal Society of Chemistry

Open Access Article. Published on 22 March 2023. Downloaded on 4/4/2023 3:23:28 PM. This article is licensed under a Creative Commons Attribution-NonCommercial 3.0 Unported Licence.

57 M. Sánchez-Purrà, B. Roig-Solvas, A. Versiani, C. Rodriguez-Quijada, H. de Puig, I. Bosch, L. Gehrke and K. Hamad-Schifferli, *Mol. Syst. Des. Eng.*, 2017, **2**, 401–409.
58 D. Zhang, L. Huang, B. Liu, E. Su, H. Y. Chen, Z. Gu and X. Zhao, *Sens. Actuators, B*, 2018, **277**, 502–509.
59 R. Chen, B. Liu, H. Ni, N. Chang, C. Luan, Q. Ge, J. Dong and X. Zhao, *Analyst*, 2019, **144**, 4051–4059.
60 L. Li, X. Dong, J. Li and J. Wei, *Dyes Pigm.*, 2020, **183**, 108756.
61 M. Balu, T. Baldacchini, J. Carter, T. B. Krasieva, R. Zadoyan and B. J. Tromberg, *J. Biomed. Opt.*, 2009, **14**, 010508.
62 G. Hong, S. Diao, A. L. Antaris and H. Dai, *Chem. Rev.*, 2015, **115**, 10816–10906.
63 N. Stone, M. Kerssens, G. R. Lloyd, K. Faulds, D. Graham and P. Matousek, *Chem. Sci.*, 2011, **2**, 776–780.
64 J. Langer, D. J. de Aberasturi, J. Aizpurua, R. A. Alvarez-Puebla, B. Auguié, J. J. Baumberg, G. C. Bazan, S. E. J. Bell, A. Boisen, A. G. Brolo, J. Choo, D. Cialla-May, V. Deckert, L. Fabris, K. Faulds, F. Javier García de Abajo, R. Goodacre, D. Graham, A. J. Haes, C. L. Haynes, C. Huck, T. Itoh, M. Käll, J. Kneipp, N. A. Kotov, H. Kuang, E. C. le Ru, H. K. Lee, J. F. Li, X. Y. Ling, S. A. Maier, T. Mayerhöfer, M. Moskovits, K. Murakoshi, J. M. Nam, S. Nie, Y. Ozaki, I. Pastoriza-Santos, J. Perez-Juste, J. Popp, A. Pucci, S. Reich, B. Ren, G. C. Schatz, T. Shegai, S. Schlücker, L. L. Tay, K. George Thomas, Z. Q. Tian, R. P. van Duyne, T. Vo-Dinh, Y. Wang, K. A. Willets, C. Xu, H. Xu, Y. Xu, Y. S. Yamamoto, B. Zhao and L. M. Liz-Marzán, *ACS Nano*, 2020, **14**, 28–117.
65 D. Li, D. Yao, C. Li, Y. Luo, A. Liang, G. Wen and Z. Jiang, *TrAC, Trends Anal. Chem.*, 2020, **127**, 115885.
66 G. Barbillon, *Nanomaterials*, 2020, **10**, 1–17.
67 M. P. Oyarzún, A. Tapia-Arellano, P. Cabrera, P. Jara-Guajardo and M. J. Kogan, *Sensors*, 2021, **21**, 1–30.
68 M. Blanco-Formoso, N. Pazos-Perez and R. A. Alvarez-Puebla, *J. Raman Spectrosc.*, 2021, **52**, 554–562.
69 B. Andreiuk, F. Nicolson, L. M. Clark, S. R. Panikkanvalappil, Kenry, M. Rashidian, S. Harmsen and M. F. Kircher, *Nanotheranostics*, 2022, **6**, 10–30.
70 I. B. Becerril-Castro, I. Calderon, N. Pazos-Perez, L. Guerrini, F. Schulz, N. Feliu, I. Chakraborty, V. Giannini, W. J. Parak and R. A. Alvarez-Puebla, *Analysis Sensing*, 2022, **2**, e20220000.
71 T. D. Payne, A. S. Moody, A. L. Wood, P. A. Pimiento, J. C. Elliott and B. Sharma, *Analyst*, 2020, **145**, 3461–3480.
72 G. Q. Wallace and J. F. Masson, *Analyst*, 2020, **145**, 7162–7185.
73 S. S. Panikar, D. Cialla-May, E. de la Rosa, P. Salas and J. Popp, *TrAC, Trends Anal. Chem.*, 2021, **134**, 116122.
74 V. Moisoiu, S. D. Iancu, A. Stefancu, T. Moisoiu, B. Pardini, M. P. Dragomir, N. Crisan, L. Avram, D. Crisan, I. Andras, D. Fodor, L. F. Leopold, C. Socaciu, Z. Bálint, C. Tomuleasa, F. Elec and N. Leopold, *Colloids Surf., B*, 2021, **208**, 112064.
75 V. Cupil-Garcia, P. Strobbia, B. M. Crawford, H. N. Wang, H. Ngo, Y. Liu and T. Vo-Dinh, *J. Raman Spectrosc.*, 2021, **52**, 541–553.
76 M. E. Berry, H. Kearns, D. Graham and K. Faulds, *Analyst*, 2021, **146**, 6084–6101.
77 W. A. Hassanain, C. L. Johnson, K. Faulds, D. Graham and N. Keegan, *Analyst*, 2022, **147**, 4674–4700.
78 H. Chen, Z. Cheng, X. Zhou, R. Wang and F. Yu, *Anal. Chem.*, 2022, **94**, 143–164.
79 A. Guerrero-Martínez, S. Barbosa, I. Pastoriza-Santos and L. M. Liz-Marzán, *Curr. Opin. Colloid Interface Sci.*, 2011, **16**, 118–127.
80 P. F. Liao and A. Wokaun, *J. Chem. Phys.*, 1982, **76**, 751–752.
81 L. Rodríguez-Lorenzo, R. A. Álvarez-Puebla, I. Pastoriza-Santos, S. Mazzucco, O. Stéphan, M. Kociak, L. M. Liz-Marzán and F. J. García de Abajo, *J. Am. Chem. Soc.*, 2009, **131**, 4616–4618.
82 T. Chung, S.-Y. Lee, E. Y. Song, H. Chun and B. Lee, *Sensors*, 2011, **11**, 10907–10929.
83 S. He, M. W. C. Kang, F. J. Khan, E. K. M. Tan, M. A. Reyes and J. C. Y. Kah, *J. Opt.*, 2015, **17**, 114013–114026.
84 A. Garcia-Leis, A. Torreggiani, J. V. Garcia-Ramos and S. Sanchez-Cortes, *Nanoscale*, 2015, **7**, 13629–13637.
85 C. D. L. de Albuquerque, R. G. Sobral-Filho, R. J. Poppi and A. G. Brolo, *Anal. Chem.*, 2018, **90**, 1248–1254.
86 J. A. Huang, M. Z. Mousavi, Y. Zhao, A. Hubarevich, F. Omeis, G. Giovannini, M. Schütte, D. Garoli and F. de Angelis, *Nat. Commun.*, 2019, **10**, 5321.
87 B. Li, T. Wang, Q. Su, X. Wu and P. Dong, *Sensors*, 2019, **19**, 3742.
88 B. Li, T. Wang, W. Bai, Q. Su, X. Wu and P. Dong, *IEEE Sens. J.*, 2021, **21**, 18425–18434.
89 L. Minati, D. Maniglio, F. Benetti, A. Chiappini and G. Speranza, *Materials*, 2021, **14**, 7272.
90 T. R. Nayak, C. Andreou, A. Oseledchyk, W. D. Marcus, H. C. Wong, J. Massagué and M. F. Kircher, *Nanoscale*, 2017, **9**, 1110–1119.
91 K. Dardir, H. Wang, B. E. Martin, M. Atzampou, C. B. Brooke and L. Fabris, *J. Phys. Chem. C*, 2020, **124**, 3211–3217.
92 S. He, Y. M. E. Kyaw, E. K. M. Tan, L. Bekale, M. W. C. Kang, S. S. Y. Kim, I. Tan, K. P. Lam and J. C. Y. Kah, *Anal. Chem.*, 2018, **90**, 6071–6080.
93 J. Dong, X. Zhao, W. Gao, Q. Han, J. Qi, Y. Wang, S. Guo and M. Sun, *Nanoscale Res. Lett.*, 2019, **14**, 118.
94 Y. Sun, S. Ge, J. Xue, X. Zhou, W. Lu, G. Li and X. Cao, *Biomed. Opt. Express*, 2020, **11**, 7062.
95 N. Albarghouthi, P. MacMillan and C. L. Brosseau, *Analyst*, 2021, **146**, 2037–2047.
96 B. Nikoobakht and M. A. El-Sayed, *Chem. Mater.*, 2003, **15**, 1957–1962.
97 P. L. Gai and M. A. Harmer, *Nano Lett.*, 2002, **2**, 771–774.
98 S. K. Meena and M. Sulpizi, *Angew. Chem., Int. Ed.*, 2016, **55**, 11960–11964.
99 J. A. da Silva and M. R. Meneghetti, *Langmuir*, 2018, **34**, 366–375.
100 J. A. da Silva, P. A. Netz and M. R. Meneghetti, *Langmuir*, 2020, **36**, 257–263.
101 C. J. Johnson, E. Dujardin, S. A. Davis, C. J. Murphy and S. Mann, *J. Mater. Chem.*, 2002, **12**, 1765–1770.

© 2023 The Author(s). Published by the Royal Society of Chemistry

Open Access Article. Published on 22 March 2023. Downloaded on 4/4/2023 3:23:28 PM. This article is licensed under a Creative Commons Attribution-NonCommercial 3.0 Unported Licence.

102 M. J. Walsh, S. J. Barrow, W. Tong, A. M. Funston and J. Etheridge, *ACS Nano*, 2015, **9**, 715–724.
103 M. J. Walsh, W. Tong, H. Katz-Boon, P. Mulvaney, J. Etheridge and A. M. Funston, *Acc. Chem. Res.*, 2017, **50**, 2925–2935.
104 W. Tong, M. J. Walsh, P. Mulvaney, J. Etheridge and A. M. Funston, *J. Phys. Chem. C*, 2017, **121**, 3549–3559.
105 W. Tong, H. Katz-Boon, M. J. Walsh, M. Weyland, J. Etheridge and A. M. Funston, *Chem. Commun.*, 2018, **54**, 3022–3025.
106 J. A. Edgar, A. M. McDonagh and M. B. Cortie, *ACS Nano*, 2012, **6**, 1116–1125.
107 G. González-Rubio, V. Kumar, P. Llombart, P. Díaz-Núñez, E. Bladt, T. Altantzis, S. Bals, O. Peña-Rodríguez, E. G. Noya, L. G. Macdowell, A. Guerrero-Martínez and L. M. Liz-Marzán, *ACS Nano*, 2019, **13**, 4424–4435.
108 Y. Xia, Y. Xiong, B. Lim and S. E. Skrabalak, *Angew. Chem., Int. Ed.*, 2009, **48**, 60–103.
109 Y. Xia, X. Xia and H.-C. Peng, *J. Am. Chem. Soc.*, 2015, **137**, 7947–7966.
110 G. González-Rubio, L. Scarabelli, A. Guerrero-Martínez and L. M. Liz-Marzán, *ChemNanoMat*, 2020, **6**, 698–707.
111 Z. Chen, J. W. Chang, C. Balasanthiran, S. T. Milner and R. M. Rioux, *J. Am. Chem. Soc.*, 2019, **141**, 4328–4337.
112 A. Sánchez-Iglesias, K. Jenkinson, S. Bals and L. M. Liz-Marzán, *J. Phys. Chem. C*, 2021, **125**, 23937–23944.
113 A. Waragai, T. Nakagawa, W. L. Hinze and Y. Takagai, *Langmuir*, 2021, **37**, 10702–10707.
114 X. Lin, C. Li, C. He, Y. Zhou, Z. Wang, N. Duan and S. Wu, *ACS Appl. Nano Mater.*, 2021, **4**, 8231–8240.
115 A. S. Tatar, C. Farcău, A. Vulpoi, S. Boca and S. Astilean, *Spectrochim. Acta, Part A*, 2022, **273**, 121069.
116 F. Liebig, R. Henning, R. M. Sarhan, C. Prietzel, M. Bargheer and J. Koetz, *Nanotechnology*, 2018, **29**, 185603.
117 A. Jakhmola, R. Vecchione, F. Gentile, M. Profeta, A. C. Manikas, E. Battista, M. Celentano, V. Onesto and P. A. Netti, *Mater. Today Chem.*, 2019, **14**, 100203.
118 L. A. Osminkina, O. Žukovskaja, S. N. Agafilushkina, E. Kaniukov, O. Stranik, K. A. Gonchar, D. Yakimchuk, V. Bundyukova, D. A. Chermoshentsev, S. A. Dyakov, N. A. Gippius, K. Weber, J. Popp, D. Cialla-May and V. Sivakov, *Appl. Surf. Sci.*, 2020, **507**, 144989.
119 T. K. Sau, A. L. Rogach, M. Döblinger and J. Feldmann, *Small*, 2011, **7**, 2188–2194.
120 H. I. Khan, M. U. Khalid, A. Abdullah, A. Ali, A. S. Bhatti, S. U. Khan and W. Ahmed, *J. Vac. Sci. Technol., B: Nanotechnol. Microelectron.: Mater., Process., Meas., Phenom.*, 2018, **36**, 03E101.
121 P. Pallavicini, A. Donà, A. Casu, G. Chirico, M. Collini, G. Dacarro, A. Falqui, C. Milanese, L. Sironi and A. Taglietti, *Chem. Commun.*, 2013, **49**, 6265–6267.
122 A. J. Blanch, M. Döblinger and J. Rodríguez-Fernández, *Small*, 2015, **11**, 4550–4559.
123 S. Atta, M. Beetz and L. Fabris, *Nanoscale*, 2019, **11**, 2946–2958.
124 F. Liebig, R. Henning, R. M. Sarhan, C. Prietzel, C. N. Z. Schmitt, M. Bargheer and J. Koetz, *RSC Adv.*, 2019, **9**, 23633–23641.
125 P. Senthil Kumar, I. Pastoriza-Santos, B. Rodríguez-González, F. Javier García De Abajo and L. M. Liz-Marzán, *Nanotechnology*, 2008, **19**, 015606.
126 Y. Pu, Y. Zhao, P. Zheng and M. Li, *Inorg. Chem.*, 2018, **57**, 8599–8607.
127 T. T. V. Phan, V. T. Nguyen, S.-H. Ahn and J. Oh, *Eur. Polym. J.*, 2019, **118**, 492–501.
128 P. T. Huynh, G. D. Nguyen, K. T. le Tran, T. M. Ho, B. T. Duong, V. Q. Lam and T. V. K. Ngo, *J. Nanomater.*, 2021, **2021**, 1–10.
129 W. Xi and A. J. Haes, *J. Am. Chem. Soc.*, 2019, **141**, 4034–4042.
130 O. M. Bakr, B. H. Wunsch and F. Stellacci, *Chem. Mater.*, 2006, **18**, 3297–3301.
131 H. Yuan, C. G. Khoury, H. Hwang, C. M. Wilson, G. A. Grant and T. Vo-Dinh, *Nanotechnology*, 2012, **23**, 075102.
132 L. Minati, F. Benetti, A. Chiappini and G. Speranza, *Colloids Surf., A*, 2014, **441**, 623–628.
133 K. Chandra, K. S. B. Culver, S. E. Werner, R. C. Lee and T. W. Odom, *Chem. Mater.*, 2016, **28**, 6763–6769.
134 C. A. Foss, G. L. Hornyak, J. A. Stockert and C. R. Martin, *J. Phys. Chem.*, 1994, **98**, 2963–2971.
135 N. Kameta and H. Shiroishi, *Chem. Commun.*, 2018, **54**, 4665–4668.
136 H. Yuan, M. Wanhong, C. Chen, J. Zhao, J. Liu, H. Zhu and X. Gao, *Chem. Mater.*, 2007, **19**, 1592–1600.
137 J. Xie, J. Y. Lee and D. I. C. Wang, *Chem. Mater.*, 2007, **19**, 2823–2830.
138 A. M. Fales, H. Yuan and T. Vo-Dinh, *J. Phys. Chem. C*, 2014, **118**, 3708–3715.
139 A. S. de Silva Indrasekara, S. F. Johnson, R. A. Odion and T. Vo-Dinh, *ACS Omega*, 2018, **3**, 2202–2210.
140 H. T. Phan and A. J. Haes, *J. Phys. Chem. C*, 2019, **123**, 16495–16507.
141 E. Tosatti and F. Ercolessi, *Mod. Phys. Lett. B*, 1991, **5**, 413–425.
142 H. Vanrompay, E. Bladt, W. Albrecht, A. Béché, M. Zakhozheva, A. Sánchez-Iglesias, L. M. Liz-Marzán and S. Bals, *Nanoscale*, 2018, **10**, 22792–22801.
143 C. Deriu, A. N. Morozov and A. M. Mebel, *J. Phys. Chem. A*, 2022, **126**, 5236–5251.
144 A. Borowik, K. Butowska, K. Konkel, R. Banasiuk, N. Derewonko, D. Wyrzykowski, M. Davydenko, V. Cherepanov, V. Styopkin, Y. Prylutskyy, P. Pohl, A. Krolicka and J. Piosik, *Nanomaterials*, 2019, **9**, 973.
145 X. Shi, H. L. Perry and J. D. E. T. Wilton-Ely, *Nanotheranostics*, 2021, **5**, 155–165.
146 H.-M. Song, Q. Wei, Q. K. Ong and A. Wei, *ACS Nano*, 2010, **4**, 5163–5173.
147 C. Kuttner, V. Piotto and L. M. Liz-Marzán, *Chem. Mater.*, 2021, **33**, 8904–8914.
148 M. Becucci, M. Bracciali, G. Ghini, C. Lofrumento, G. Pietraperzia, M. Ricci, L. Tognaccini, S. Trigari, C. Gellini and A. Feis, *Nanoscale*, 2018, **10**, 9329–9337.

© 2023 The Author(s). Published by the Royal Society of Chemistry

Open Access Article. Published on 22 March 2023. Downloaded on 4/4/2023 3:23:28 PM. This article is licensed under a Creative Commons Attribution-NonCommercial 3.0 Unported Licence.

149 X. Luo, L. Qiao, Z. Xia, J. Yu, X. Wang, J. Huang, C. Shu, C. Wu and Y. He, *Langmuir*, 2022, **38**, 6454–6463.
150 D. C, P. Sahu and D. V. R. Kumar, *J. Chem. Sci.*, 2022, **134**, 64.
151 P. Drude, *Ann. Phys.*, 1900, **306**, 566–613.
152 E. C. le Ru and P. G. Etchegoin, *Principles of Surface-enhanced Raman Spectroscopy and related plasmonic effects*, Elsevier, Amsterdam, 2009.
153 X. Liu, *Front. Mater.*, 2018, **5**, 59.
154 B. Yang, S. Jin, S. Guo, Y. Park, L. Chen, B. Zhao and Y. M. Jung, *ACS Omega*, 2019, **4**, 20101–20108.
155 X. Wang, E. Zhang, H. Shi, Y. Tao and X. Ren, *Analyst*, 2022, **147**, 1257–1272.
156 G. Song, S. Cong and Z. Zhao, *Chem. Sci.*, 2022, **13**, 1210–1224.
157 X. Wang and L. Guo, *Angew. Chem., Int. Ed.*, 2020, **132**, 4259–4267.
158 S. Cong, Y. Yuan, Z. Chen, J. Hou, M. Yang, Y. Su, Y. Zhang, L. Li, Q. Li, F. Geng and Z. Zhao, *Nat. Commun.*, 2015, **6**, 7800.
159 J. R. Lombardi, R. L. Birke, T. Lu and J. Xu, *J. Chem. Phys.*, 1986, **84**, 4174–4180.
160 Samriti, V. Rajput, R. K. Gupta and J. Prakash, *J. Mater. Chem. C*, 2022, **10**, 73–95.
161 M. Li, X. Fan, Y. Gao and T. Qiu, *J. Phys. Chem. Lett.*, 2019, **10**, 4038–4044.
162 X. Jiang, L. Xu, W. Ji, W. Wang, J. Du, L. Yang, W. Song, X. Han and B. Zhao, *Appl. Surf. Sci.*, 2022, **584**, 152609.
163 S. Xie, K. Lai, C. Gu, T. Jiang, L. Zhou, X. Zheng, X. Shen, J. Han and J. Zhou, *Mater. Today Nano*, 2022, **18**, 100179.
164 A. D. Terna, E. E. Elemike, J. I. Mbonu, O. E. Osafile and R. O. Ezeani, *Mater. Sci. Eng., B*, 2021, **272**, 115363.
165 E. W. Seelig, B. Tang, A. Yamilov, H. Cao and R. P. H. Chang, *Mater. Chem. Phys.*, 2003, **80**, 257–263.
166 R. Spectroscopy, X. Wang, W. Shi, Z. Jin, W. Huang, J. Lin, G. Ma, S. Li, L. Guo, X. Wang, Z. Jin, J. Lin, G. Ma, L. Guo, D. Shi, S. Li and D. Huang, *Angew. Chem., Int. Ed.*, 2017, **56**, 9851–9855.
167 T. Taib, M. R. Johan and W. J. Basirun, *Phys. B*, 2021, **606**, 412638.
168 B. Bonelli, O. Tammaro, F. Martinovic, R. Nasi, G. Dell'Agli, P. Rivolo, F. Giorgis, N. Ditaranto, F. A. Deorsola and S. Esposito, *ACS Omega*, 2021, **6**, 24562–24574.
169 X. Chen, N. Deng, X. Zhang, Y. Yang, J. Li, B. Hong, J. Fang, J. Xu, D. Jin, X. Peng, X. Wang and H. Jin, *Chem. Phys. Lett.*, 2019, **722**, 96–103.
170 L. Ma, Q. Zhang, J. Li, X. Lu, C. Gao, P. Song and L. Xia, *Materials*, 2021, **14**, 922.
171 S. Thakur and S. Neogi, *Appl. Nanosci.*, 2021, **11**, 159–171.
172 Y. Wang, M. Zhang, H. Ma, H. Su, A. Li, W. Ruan and B. Zhao, *ACS Appl. Mater. Interfaces*, 2021, **13**, 35038–35045.
173 M. Zhang, Y. Wang, X. Wang, B. Zhao and W. Ruan, *J. Phys. Chem. C*, 2021, **125**, 17125–17132.
174 L. Zhou, J. Zhou, W. Lai, X. Yang, J. Meng, L. Su, C. Gu, T. Jiang, E. Y. B. Pun, L. Shao, L. Petti, X. W. Sun, Z. Jia, Q. Li, J. Han and P. Mormile, *Nat. Commun.*, 2020, **11**, 1785.
175 R. Haldavnekar, K. Venkatakrishnan and B. Tan, *Nat. Commun.*, 2018, **9**, 3065.
176 D.-J. Lee and D. Y. Kim, *Sensors*, 2019, **19**, 5471.
177 J. Liu, Y. Liu, Y. Cao, S. Sang, L. Guan, Y. Wang and J. Wang, *Micromachines*, 2022, **13**, 128.
178 X. Ling, L. G. Moura, M. A. Pimenta and J. Zhang, *J. Phys. Chem. C*, 2012, **116**, 25112–25118.
179 W. Xu, N. Mao and J. Zhang, *Small*, 2013, **9**, 1206–1224.
180 X. Ling, S. Huang, S. Deng, N. Mao, J. Kong, M. S. Dresselhaus and J. Zhang, *Acc. Chem. Res.*, 2015, **48**, 1862–1870.
181 Z. Wang, S. Wu, L. Colombi Ciacchi and G. Wei, *Analyst*, 2018, **143**, 5074–5089.
182 G. Darabdhara, M. R. Das, S. P. Singh, A. K. Rengan, S. Szunerits and R. Boukherroub, *Adv. Colloid Interface Sci.*, 2019, **271**, 101991.
183 H. Lai, F. Xu, Y. Zhang and L. Wang, *J. Mater. Chem. B*, 2018, **6**, 4008–4028.
184 X. Ling, S. Huang, S. Deng, N. Mao, J. Kong, M. S. Dresselhaus and J. Zhang, *Acc. Chem. Res.*, 2015, **48**, 1862–1870.
185 L. Yang, J.-H. Lee, C. Rathnam, Y. Hou, J.-W. Choi and K.-B. Lee, *Nano Lett.*, 2019, **19**, 8138–8148.
186 Y. Yang, Y. Cong, J. Shang, Y. Liu, G. Fang, J. Zhang and B. Dong, *Sens. Actuators, B*, 2021, **330**, 129199.
187 S. Atta, S. Rangan and L. Fabris, *ChemNanoMat*, 2020, **6**, 53–57.
188 H. Bao, Y. Guo, T. Zhang, H. Fu, S. Zhu, L. Zhou, H. Zhang, Y. Li, W. Cai, H. Bao, Y. Guo, T. Zhang, H. Fu, S. Zhu, L. Zhou, H. Zhang, Y. Li and W. Cai, *Adv. Mater. Interfaces*, 2022, **9**, 2102107.
189 O. M. Yaghi, M. J. Kalmutzki and C. S. Diercks, *Introduction to Reticular Chemistry: Metal-Organic Frameworks and Covalent Organic Frameworks*, Wiley-VCH, Weinheim, 2019.
190 N. Martín and F. G. Cirujano, *Org. Biomol. Chem.*, 2020, **18**, 8058–8073.
191 S. Denning, A. A. A. Majid, J. M. Lucero, J. M. Crawford, M. A. Carreon and C. A. Koh, *ACS Appl. Mater. Interfaces*, 2020, **12**, 53510–53518.
192 J. Cao, X. Li and H. Tian, *Curr. Med. Chem.*, 2019, **27**, 5949–5969.
193 E. A. Dolgopolova, A. M. Rice, C. R. Martin and N. B. Shustova, *Chem. Soc. Rev.*, 2018, **47**, 4710–4728.
194 Y. Zhang, Y. Hu, G. Li and R. Zhang, *Microchim. Acta*, 2019, **186**, 1–10.
195 X. Zhao, T. Yang, D. Wang, N. Zhang, H. Yang, X. Jing, R. Niu, Z. Yang, Y. Xie and L. Meng, *Anal. Chem.*, 2022, **94**, 4484–4494.
196 S. Bock, Y. S. Choi, M. Kim, Y. Yun, X. H. Pham, J. Kim, B. Seong, W. Kim, A. Jo, K. M. Ham, S. G. Lee, S. H. Lee, H. Kang, H. S. Choi, D. H. Jeong, H. Chang, D. E. Kim and B. H. Jun, *J. Nanobiotechnol.*, 2022, **20**, 130.
197 Y. Gutiérrez, A. S. Brown, F. Moreno and M. Losurdo, *J. Appl. Phys.*, 2020, **128**, 080901.
198 J. Asselin, C. Boukouvala, E. R. Hopper, Q. M. Ramasse, J. S. Biggins and E. Ringe, *ACS Nano*, 2020, **14**, 5968–5980.

Open Access Article. Published on 22 March 2023. Downloaded on 4/4/2023 3:23:28 PM. This article is licensed under a Creative Commons Attribution-NonCommercial 3.0 Unported Licence.

199 E. R. Hopper, T. M. R. Wayman, J. Asselin, B. Pinho, C. Boukouvala, L. Torrente-Murciano and E. Ringe, *J. Phys. Chem. C*, 2022, **2022**, 39.
200 S. Juneja and M. S. Shishodia, *Opt. Commun.*, 2019, **433**, 89–96.
201 W. Li, R. Zamani, P. Rivera Gil, B. Pelaz, M. Ibáñez, D. Cadavid, A. Shavel, R. A. Alvarez-Puebla, W. J. Parak, J. Arbiol and A. Cabot, *J. Am. Chem. Soc.*, 2013, **135**, 7098–7101.
202 J. E. Sanchez, S. A. Jaramillo, E. Settles, J. J. Velazquez Salazar, A. Lehr, J. Gonzalez, C. Rodríguez Aranda, H. R. Navarro-Contreras, M. O. Raniere, M. Harvey, D. M. Wagner, A. Koppisch, R. Kellar, P. Keim and M. Jose Yacaman, *RSC Adv.*, 2021, **11**, 25788–25794.
203 U. Guler, G. v. Naik, A. Boltasseva, V. M. Shalaev and A. v. Kildishev, *Appl. Phys. B*, 2012, **107**, 285–291.
204 U. Guler, A. v. Kildishev, A. Boltasseva and V. M. Shalaev, *Faraday Discuss.*, 2015, **178**, 71–86.
205 J. Asselin, C. Boukouvala, E. R. Hopper, Q. M. Ramasse, J. S. Biggins and E. Ringe, *ACS Nano*, 2020, **14**, 5968–5980.
206 J. Asselin, C. Boukouvala, Y. Wu, E. R. Hopper, S. M. Collins, J. S. Biggins and E. Ringe, *J. Chem. Phys.*, 2019, **151**, 244708.
207 E. A. Jenrette, M. J. Farrell, J. A. Flowers and A. K. Pradhan, *Nanomanufacturing*, 2021, **1**, 3–13.
208 T. Daeneke, B. J. Carey, A. F. Chrimes, J. Z. Ou, D. W. M. Lau, B. C. Gibson, M. Bhaskaran and K. Kalantar-zadeh, *J. Mater. Chem. C*, 2015, **3**, 4771–4778.
209 L. Fabris, *J. Opt.*, 2015, **17**, 114002.
210 H. Wang, K. Dardir, K.-B. Lee and L. Fabris, *Bioconjugate Chem.*, 2019, **30**, 2555–2562.
211 C. Andreou, S. A. Kishore and M. F. Kircher, *J. Nucl. Med.*, 2015, **56**, 1295–1299.
212 C. Andreou, V. Neuschmelting, D.-F. Tschaharganeh, C.-H. Huang, A. Oseledchyk, P. Iacono, H. Karabeber, R. R. Colen, L. Mannelli, S. W. Lowe and M. F. Kircher, *ACS Nano*, 2016, **10**, 5015–5026.
213 S. Pal, S. Harmsen, A. Oseledchyk, H.-T. Hsu and M. F. Kircher, *Adv. Funct. Mater.*, 2017, **27**, 1606632.
214 F. Nicolson, B. Andreiuk, C. Andreou, H. T. Hsu, S. Rudder and M. F. Kircher, *Theranostics*, 2019, **9**, 5899–5913.
215 V. Dugandžić, D. Drikermann, O. Ryabchykov, A. Undisz, I. Vilotijević, S. Lorkowski, T. W. Bocklitz, C. Matthäus, K. Weber, D. Cialla-May and J. Popp, *J. Biophotonics*, 2018, **11**, e201800013.
216 C. Song, F. Li, X. Guo, W. Chen, C. Dong, J. Zhang, J. Zhang and L. Wang, *J. Mater. Chem. B*, 2019, **7**, 2001–2008.
217 M. Bhamidipati, H. Y. Cho, K. B. Lee and L. Fabris, *Bioconjugate Chem.*, 2018, **29**, 2970–2981.
218 Thermo Scientific, *Bioconjugation and crosslinking technical handbook*, **https://assets.thermofisher.com/TFS-Assets/BID/Handbooks/bioconjugation-technical-handbook.pdf**, accessed 24 October 2022.
219 G. T. Hermanson, in *Bioconjugate Techniques*, Elsevier, Amsterdam, 2013, pp. 229–258.
220 G. T. Hermanson, in *Bioconjugate Techniques*, Elsevier, Amsterdam, 2013, pp. 259–273.
221 W. H. Brown, C. S. Foote, B. L. Iverson and E. V. Ansly, *Organic Chemistry*, Brooks/Cole, Belmont, 6th edn, 2010.
222 G. T. Hermanson, in *Bioconjugate Techniques*, Elsevier, Amsterdam, 2013, pp. 299–339.
223 J. A. Burns, J. C. Butler, J. Moran and G. M. Whitesides, *J. Org. Chem.*, 1991, **56**, 2648–2650.
224 B. Liu and J. Liu, *J. Am. Chem. Soc.*, 2017, **139**, 9471–9474.
225 D. S. Seferos, D. A. Giljohann, H. D. Hill, A. E. Prigodich and C. A. Mirkin, *J. Am. Chem. Soc.*, 2007, **129**, 15477–15479.
226 P.-C. Guan, H. Zhang, Z.-Y. Li, S.-S. Xu, M. Sun, X.-M. Tian, Z. Ma, J.-S. Lin, M.-M. Gu, H. Wen, F.-L. Zhang, Y.-J. Zhang, G.-J. Yu, C. Yang, Z.-X. Wang, Y. Song and J.-F. Li, *Anal. Chem.*, 2022, **94**, 17795–17802.
227 W. Teng, J. Zhao, Q. Li, P. Shi, J. Zhang, M. Yan and S. Zhang, *Sens. Diagn.*, 2023, **2**, 132–139.
228 S. T. Sivapalan, B. M. DeVetter, T. K. Yang, T. van Dijk, M. V. Schulmerich, P. S. Carney, R. Bhargava and C. J. Murphy, *ACS Nano*, 2013, **7**, 2099–2105.
229 D. Li, L. Jiang, J. A. Piper, I. S. Maksymov, A. D. Greentree, E. Wang and Y. Wang, *ACS Sens.*, 2019, **4**, 2507–2514.
230 D. Zhang, L. Huang, B. Liu, E. Su, H. Y. Chen, Z. Gu and X. Zhao, *Sens. Actuators, B*, 2018, **277**, 502–509.
231 S. Harmsen, M. A. Bedics, M. A. Wall, R. Huang, M. R. Detty and M. F. Kircher, *Nat. Commun.*, 2015, **6**, 6570.
232 S. Rajappa, in *Comprehensive Heterocyclic Chemistry*, Elsevier, Amsterdam, 1984, pp. 741–861.
233 M. A. Bedics, H. Kearns, J. M. Cox, S. Mabbott, F. Ali, N. C. Shand, K. Faulds, J. B. Benedict, D. Graham and M. R. Detty, *Chem. Sci.*, 2015, **6**, 2302–2306.
234 T. Nakamura, R. Kimura, F. Matsui, H. Kondoh, T. Ohta, H. Sakai, M. Abe and M. Matsumoto, *Langmuir*, 2000, **16**, 4213–4216.
235 F. K. Huang, R. C. Horton, D. C. Myles and R. L. Garrell, *Langmuir*, 1998, **14**, 4802–4808.
236 S. Y. Lee, E. Ito, H. Kang, M. Hara, H. Lee and J. Noh, *J. Phys. Chem. C*, 2014, **118**, 8322–8330.
237 H. Kearns, M. A. Bedics, N. C. Shand, K. Faulds, M. R. Detty and D. Graham, *Analyst*, 2016, **141**, 5062–5065.
238 H. Kearns, F. Ali, M. A. Bedics, N. C. Shand, K. Faulds, M. R. Detty and D. Graham, *R. Soc. Open Sci.*, 2017, **4**, 170422.
239 O. Zeiri, *ACS Sens.*, 2020, **5**, 3806–3820.
240 S. Mosca, C. Conti, N. Stone and P. Matousek, *Nat. Rev. Methods Primers*, 2021, **1**, 21.
241 N. A. Macleod and P. Matousek, *Appl. Spectrosc.*, 2008, **62**, 291A–304A.
242 F. Martelli, S. del Bianco, A. Ismaelli and G. Zaccanti, *Light Propagation Through Biological Tissue and Other Diffusive Media: Theory, Solutions, and Software (SPIE Press Monograph vol. PM193)*, 2010.
243 N. Stone, K. Faulds, D. Graham and P. Matousek, *Anal. Chem.*, 2010, **82**, 3969–3973.
244 B. Sharma, K. Ma, M. R. Glucksberg and R. P. van Duyne, *J. Am. Chem. Soc.*, 2013, **135**, 17290–17293.
245 F. Nicolson, L. E. Jamieson, S. Mabbott, K. Plakas, N. C. Shand, M. R. Detty, D. Graham and K. Faulds, *Analyst*, 2018, **143**, 5358–5363.

© 2023 The Author(s). Published by the Royal Society of Chemistry

Open Access Article. Published on 22 March 2023. Downloaded on 4/4/2023 3:23:28 PM.
This article is licensed under a Creative Commons Attribution-NonCommercial 3.0 Unported Licence.

246 F. Nicolson, L. E. Jamieson, S. Mabbott, N. C. Shand, D. Graham and K. Faulds, *J. Raman Spectrosc.*, 2017, **48**, 1828–1838.
247 P. R. Bakic, C. Zhang and A. D. A. Maidment, *Med. Phys.*, 2011, **38**, 3165–3176.
248 F. Nicolson, L. E. Jamieson, S. Mabbott, K. Plakas, N. C. Shand, M. R. Detty, D. Graham and K. Faulds, *Chem. Sci.*, 2018, **9**, 3788–3792.
249 F. Nicolson, L. E. Jamieson, S. Mabbott, K. Plakas, N. C. Shand, M. R. Detty, D. Graham and K. Faulds, *Chem. Commun.*, 2018, **54**, 8530–8533.
250 S. Mosca, P. Dey, T. A. Tabish, F. Palombo, N. Stone and P. Matousek, *J. Biophotonics*, 2020, **13**, e201960092.
251 M. E. Berry, S. M. Mccabe, N. C. Shand, D. Graham and K. Faulds, *Chem. Commun.*, 2022, **58**, 1756.
252 A. S. Moody, T. D. Payne, B. A. Barth and B. Sharma, *Analyst*, 2020, **145**, 1885–1893.
253 A. S. Moody and B. Sharma, *ACS Chem. Neurosci.*, 2018, **9**, 1380–1387.
254 T. A. Qiu, P. L. Clement and C. L. Haynes, *Chem. Commun.*, 2018, **54**, 12787–12803.
255 W. Najahi-Missaoui, R. D. Arnold and B. S. Cummings, *Int. J. Mol. Sci.*, 2020, **22**, 385.
256 C. Egbuna, V. K. Parmar, J. Jeevanandam, S. M. Ezzat, K. C. Patrick-Iwuanyanwu, C. O. Adetunji, J. Khan, E. N. Onyeike, C. Z. Uche, M. Akram, M. S. Ibrahim, N. M. el Mahdy, C. G. Awuchi, K. Saravanan, H. Tijjani, U. E. Odoh, M. Messaoudi, J. C. Ifemeje, M. C. Olisah, N. J. Ezeofor, C. J. Chikwendu and C. G. Ibeabuchi, *J. Toxicol.*, 2021, **2021**, 1–21.
257 R. Singh, A. Sharma, J. Saji, A. Umapathi, S. Kumar and H. K. Daima, *Nano Convergence*, 2022, **9**, 21.
258 S. Kumar, K. S. Gandhi and R. Kumar, *Ind. Eng. Chem. Res.*, 2007, **46**, 3128–3136.
259 S. R. Jackson, J. R. McBride, S. J. Rosenthal and D. W. Wright, *J. Am. Chem. Soc.*, 2014, **136**, 5261–5263.
260 K. Christmann, Introduction to Surface Physical Chemistry, in *Topics in Physical Chemistry*, Springer-Verlag, Berlin/Heidelberg, 1991, vol. 1.
261 D. P. dos Santos, M. L. A. Temperini and A. G. Brolo, *Acc. Chem. Res.*, 2019, **52**, 456–464.
262 M. Belkin, S.-H. Chao, M. P. Jonsson, C. Dekker and A. Aksimentiev, *ACS Nano*, 2015, **9**, 10598–10611.
263 C. Chen, Y. Li, S. Kerman, P. Neutens, K. Willems, S. Cornelissen, L. Lagae, T. Stakenborg and P. van Dorpe, *Nat. Commun.*, 2018, **9**, 1733.
264 D. Deamer, M. Akeson and D. Branton, *Nat. Biotechnol.*, 2016, **34**, 518–524.
265 N. A. Jose, M. Kovalev, E. Bradford, A. M. Schweidtmann, H. Chun Zeng and A. A. Lapkin, *Chem. Eng. J.*, 2021, **426**, 131345.
266 K.-J. Wu, G. M. de Varine Bohan and L. Torrente-Murciano, *React. Chem. Eng.*, 2017, **2**, 116–128.
267 E. Bradford, A. M. Schweidtmann and A. Lapkin, *J. Glob. Optim.*, 2018, **71**, 407–438.
268 A. M. Schweidtmann, A. D. Clayton, N. Holmes, E. Bradford, R. A. Bourne and A. A. Lapkin, *Chem. Eng. J.*, 2018, **352**, 277–282.
269 A. D. Clayton, A. M. Schweidtmann, G. Clemens, J. A. Manson, C. J. Taylor, C. G. Niño, T. W. Chamberlain, N. Kapur, A. J. Blacker, A. A. Lapkin and R. A. Bourne, *Chem. Eng. J.*, 2020, **384**, 123340.
270 B. Smiri, F. Saidi, A. Mlayah and H. Maaref, *J. Mater. Sci.: Mater. Electron.*, 2020, **31**, 10750–10759.
271 T. Qi, Y. Yu, Y. Hu, K. Li, N. Guo and Y. Jia, *Nanomaterials*, 2022, **12**, 1258.

© 2023 The Author(s). Published by the Royal Society of Chemistry